Simulation of the Transmitted Dose in an EPID Using a Monte Carlo Method

Thuc M Pham

ADELAIDE
UNIVERSITY
AUSTRALIA

Thesis submitted for the degree of
Master of Science
In the School of Chemistry and Physics
University of Adelaide

Supervisors:

Dr. Eva Bezak
Mr Kim Quach

March 2009

Contents

ABSTRACT

The BEAMnrc and DOSXYZnrc codes from EGSnrc Monte Carlo (MC) system are considered to be the gold standards for simulating radiotherapy linear accelerators and resulting dose depositions (Rogers, Faddegon et al. 1995). The aim of this project was to setup the EGSnrc system for the simulation of the linear accelerator (linac) head and a Scanning Liquid Ionisation Chamber (SLIC) Electronic Portal Imaging Device (EPID) for calculations of transmitted dose in the EPID.

The project was divided into two parts. The head of a 6 MV Varian 600C/D photon linac was first simulated by BEAMnrc. The modelling parameters such as the electron beam energy and the Full Width at Half Maximum (FWHM) of the electron spatial distribution were adjusted until the absorbed dose profiles and the Percentage Depth Dose (PDD) curves, in general agreed better than the measured profiles and PDDs by 2%. The X-ray beam obtained from the modelled linac head was used for the simulation of the transmitted dose in the EPID in the second part of the project. The EPID was simulated by DOSXYZnrc based on the information obtained from Spezi and Lewis 2002 (Spezi and Lewis 2002), who also modelled the Varian SLIC EPID (MK2 Portal Vision system, Varian Inc., Palo Alto, CA, USA). The comparisons between the measured and the simulated transmitted doses were carried out for three different phantom setups consisting of an open field, homogeneous water equivalent phantom and a humanoid phantom (RANDO). These phantom setups were designed so that the accuracy of the MC method for simulating absorbed dose in air, homogeneous and inhomogeneous phantoms could be assessed. In addition, the simulated transmitted dose in an EPID was also compared with values obtained from the Pinnacle treatment planning system (v6.2b, Phillips Medical Systems).

In the process of selecting the electron beam energy and FWHM, it was confirmed (Sheikh-Bagheri and Rogers 2002; Keall, Siebers et al. 2003) that the variation of the electron beam FWHM and energy influenced the beam profiles strongly. The PDD was influenced by the electron beam energy less strongly. The increase in the energy led to the increase in the depth of maximum dose. However, the effect could not be observed until the energy change of 0.2 MeV was made. Based on the analysis of the

results, it was found that the combination of FWHM and energy of 1.3 mm and 5.7 MeV provided the best match between the measured and MC simulated beam profiles and PDDs. It can be concluded that an accuracy of 1.5% can be achieved in the simulation of the linac head using Monte Carlo method. In the comparison between the Monte Carlo and the measured transmitted dose maps, agreements of 2% were found for both the open field and homogeneous water equivalent phantom setups. The same agreements were also found for the comparison between Monte Carlo and Pinnacle transmitted dose maps for these setups. In the setup where the humanoid phantom RANDO was introduced in between the radiation field and the EPID, a general agreement of about 5% found for the comparison between Monte Carlo and measured transmitted dose maps. Pinnacle and measured transmitted dose map was also compared for this setup and the same agreement was found.

DECLARATION

This work contains no material which has been accepted for the award of any other degree or diploma at any other university or other tertiary institution and to the best of my knowledge and belief, contains no material previously published or written by another person, except where due reference has been made in the text.

I give consent to this copy of my thesis, when deposited in the university Library, being available for loan and photocopying.

SIGNED: ________________________ DATED: __________________

ACKNOWLEDGEMENT

I would like to express my gratitude to my principle supervisor Dr Eva Bezak for her great and persistent support over the course of my project work. I am sincerely appreciate Dr Eva Bezak for welcomingly accepted me as her MSc student and enthusiastically provided me with valuable advices, ideas and knowledge in data analysis and writing of the thesis. Dr Eva Bezak treated me as a student as well as a friend which made me felt comfortable for communications and interactions throughout this work.

I would also like to thank my co-supervisor Mr Kim Quach for all of his efforts in solving the technical problems that i came across. My project work would have not run smoothly without Mr Kim Quach efforts and great support. He has been a good supervisor, mentor and also a good friend.

Furthermore, i would like to thank Dr Lotte Fog who was also supervising me at the beginning of this project work. She had provided support in setting up EGSnrc Monte Carlo codes and provided guidances in planning and organising the project work.

It had been my pleasure to work with Dr Mohammad Mohammadi and Mr Paul Reich. They had been great collaborators in part of my project. I would like to thanks them for sharing their knowledge and MatLab codes which were used for extracting and analysing RANDO data.

I would like to express my appreciation to all other staffs in the Royal Adelaide Hospital Medical Physics Department for their humorous, friendly and kind company. I also like to thank Mr Alan Baldock for kindly lending his own dial-up modem for establishing a network connection with the SAPAC's supercomputers. In addition, I like thank the SAPAC trainer and coordinator, Mr Patrick Fitzhenry who had provided me with lot of supports in remote login to SAPAC's supercomputers and executing parallel jobs in LINUX platform.

Finally, I would like to thank the University of Adelaide and Australasian College of Physical Scientists and Engineers for providing the fund to attend the EPSM national conferences in Adelaide (2005) and Noosa (2006). I also like to thank the New South Wales department of health for providing me with the funds and Mr Shan Yau for providing me with study leaves to attend two interstate project meetings with my supervisors.

Last, but not least, I would like to thank all members of my beloved family especially my mother for her great care and hospitality and my father for his strong supports and encouragements.

CHAPTER 1

INTRODUCTION AND AIM OF THE CURRENT RESEARCH

The main objective of radiotherapy is to deliver the maximum possible dose to the target tumour and the minimum dose to the healthy surrounding tissues. One way to achieve this objective is to have a good understanding of the dose distribution in the treatment target and most importantly, to be able to verify the dose distribution experimentally.

Currently, the available treatment planning systems such Pinnacle (v6.2b, Phillips Medical Systems), Eclipse (Varian Treatment Planning System, Varian Inc., Palo Alto, CA, USA) and FOCUS (CMS Inc., St Louis, Missouri, USA) are being used to calculate the dose distribution in the treatment region. One of the advantages of these planning systems is that they provide three dimensional visualisation of the dose distribution in the treatment region. However, in order to meet the main objective of radiotherapy, it is essential that the calculated dose be verified experimentally. This area of work is called in-vivo dosimetry.

Thermoluminescent detectors (TLDs) and diodes have been used widely for in-vivo dosimetry. The limitation of these methods is that they can only be used for point dose verification. Film dosimetry is a good method for 2-dimensional dose verification however, it requires a lot of care in processing and thus it is a time consuming procedure. Another tool which can be used as a 2-dimensional dosimeter is an Electronic Portal Imaging Device (EPID). In addition to its use as a position verification device in radiotherapy, it was found that the EPID’s signal can be related to the dose in the EPID’s plane known as the transmitted dose (Kirby and Williams 1993; Boellaard, van Herk et al. 1996; Parsaei, el-Khatib et al. 1998; Greer and Popescu 2003; Mohammadi and Bezak 2006). The advantage of the EPID is that no chemical processing is required. The EPID’s output signals can be transferred electronically to a computer and analysis can be performed at the same time (online verification). Practically, there is no time delay between data acquisition and processing which is particularly important for position verification purposes where patient movement may occur in between data acquisition and processing (Mohammadi 2006). The EPID data can be stored in digital form which can easily be retrieved and transferred over the network to other destinations. In addition, having a digital format, EPID data can save a lot of storage space. A study by Fielding et al 2002 and 2004 also showed that the EPID can also be used for quality assurance purposes, in particular, the leaf positioning accuracy of the Multi-leaf Collimator (MLC) in the linac head (Fielding, Evans et al. 2002; Fielding, Evans et al. 2004). An error of 2 mm in the leaf position can be detected.

Further investigations have been performed in order to derive the patient dose in three dimensions based on the transmitted dose. A method known as convolution algorithm was used by a number of authors (Essers, Hoogervorst et al. 1995; Boellaard, van Herk et al. 1996; Hansen, Evans et al. 1996; McNutt, Mackie et al. 1996). In this convolution algorithm, the pencil beam dose deposition kernel was convolved with the primary fluences in the humanoid phantom to obtain a 3D dose distribution. The primary fluence in the humanoid phantom was derived from the back-projection of the transmitted dose with correction for scattering within the humanoid phantom. The re-construction of the 3D dose distribution is not the subject of this research.

The objective of this project is to calculate the transmitted dose using the Monte Carlo method. The Monte Carlo programs BEAMnrc and DOSXYZnrc (Rogers et al 2007) were used in the current work to model the high energy X-ray linac head and to calculate the transmitted dose in the EPID respectively.

A general description of the structures of the linac head is presented in chapter 2. The emphasis of this section is to describe the components of the linac head that were modelled using the Monte Carlo program BEAMnrc. The information about the geometrical structures and material composition of the modelled EPID was obtained from the paper by (Spezi and Lewis 2002). The structures and the basic principle of operation of the EPID, particularly the Scanning Liquid Ionisation Chamber (SLIC) type, are also described in detail in chapter 2. In addition, the literature review regarding the use of an EPID for invivo dosimetry is also described in this chapter.

The EPID cannot be used for dosimetry purposes until it had been calibrated. Chapter 2 ended with a description of the EPID's calibration procedure.

Monte Carlo calculation method models the particle interaction and radiation beam from first principles therefore, in principle, it has no limitations and is generally considered to be the most accurate method for dose calculation in radiotherapy (Roger et al 1995). Chapter 3 illustrates the principle behind the Monte Carlo method and how it is applied in BEAMnrc and DOSXYZnrc programs for simulating the linac head and calculating the dose distributions in a phantom respectively. In addition to accuracy, for clinical use it is also crucial to have a MC system that can produce useful results within a reasonable time frame. This is a known difficulty for Monte Carlo programs. Chapter 3 describes the techniques used in BEAMnrc and DOSXYZnrc programs to improve the speed of the calculation while maintain its accuracy, in other word, to improve the efficiency of the calculation. Furthermore, the general literature reviews of the modelling of the linac head and the transmitted dose in an EPID are also discussed in chapter 3 and it concluded with a description of the 2D Gamma analysis technique.

The modelling procedure of the linac head for the production of an X-ray beam is described in fine detail in chapter 4. The geometrical and radiation properties of the X-ray beam such as the radiation field sizes and symmetry of the radiation beam were verified against the measured data in this work. The results are presented in this chapter. Chapter 4 also include the investigation of certain time reduction parameters such as the Bremsstrahlung Splitting and parallel processing parameters which were used in BEAMnrc and DOSXYZnrc in this work for the simulation of the linac head and dose calculation respectively.

An accurate model of the linac head and accurate transmitted dose calculation are very useful for studying the changes in dose distribution due to heterogeneity in the radiation field such as air pocket or gold seeds. These studies are not the objective of this work however, the most accurate MC model of the linac head and the transmitted dose calculation are attempted. In order to develop an accurate MC model, careful fine tuning of the modelling parameters such as: the electron energy and the Full Width at Half Maximum (FWHM) of the spatial distribution of the electron beam is necessary. Chapter 5 presents with a tuning technique in order to derive the best combination of the electron energy and the FWHM of the spatial distribution of the electron beam in this work. The analyses of the results are also discussed.

The modelling and calculation of the transmitted dose in an EPID using DOSXYZnrc is described in chapter 6. In order to verify the accuracy of the modelled EPID, the transmitted dose in an EPID through three different phantoms called an open field, homogeneous phantom and humanoid phantom were calculated. The description of these phantom setups is also presented in detail in chapter 6. All the results and analyses are also presented in this chapter.

Chapter 7 presents with the summary of all the results found in this work. It concludes with the description of the possible future works in supplement to this work and along the line of Monte Carlo modelling of the transmitted dose in an EPID.

CHAPTER 2

HARDWARES FOR TRANSMITTED DOSIMETRY

2.1 Structure Of The Linear Accelerator Head

The linear accelerator (linac) is a primary tool in external beam radiotherapy. The operation principle of the linac has been discussed in depth in the literature and many textbooks (Johns and Cunningham 1983; van Dyk 1999; Khan 2003). This chapter focuses on the general design of the linac head that produces therapy high energy X-ray beam. Therapy X-ray energies generally range between 4 and 23 MV (Johns and Cunningham 1983). In addition, a general discussion about the linac head from the modelling point of view is also included in this chapter.

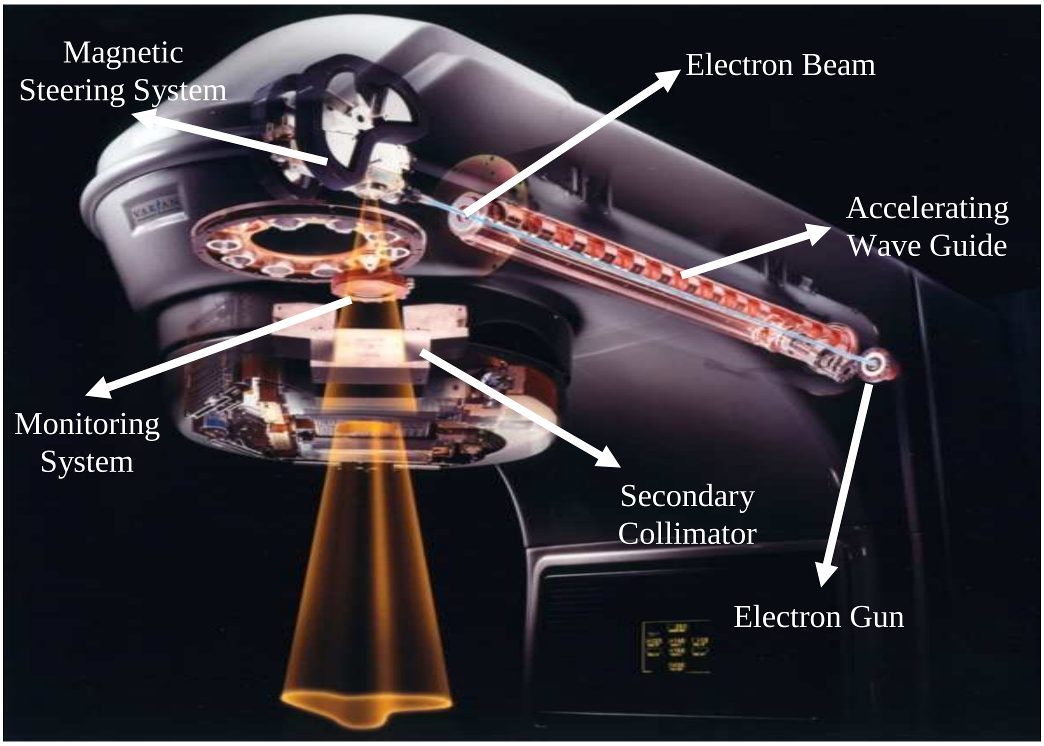

Figure 2.1.1: Internal structure of the Varian dual mode linear accelerator. (Varian Medical Systems)

The production of an X-ray beam begins at the X-ray target. An electron beam from the electron gun is accelerated to a very high speed in the linac waveguide (figure 2.1.1). This electron beam is steered by the 270^{o} magnet to hit the surface of the X-ray target at 90^{o}. As the electron beam penetrates the target material, the Coulomb interactions between the electron beam, atomic electrons in the target and the protons in the nuclei of the target material occur. Coulomb interactions caused by interaction with protons result in a deflection of the electron trajectory causing electron to lose energy. A photon is generated as a result so as to conserve the energy and momentum. A photon produced in this interaction is called a Bremsstrahlung photon. This is the main process through which the X-rays in the linac head are being produced. The X-ray production efficiency or Bremsstrahlung yield can be described by the following equation (Johns and Cunningham 1983):

$$B = \frac{1}{E_0}\int_0^{E_0} \Phi_e(E)\,\frac{S_{rad}(E)}{S_{total}(E)}\,dE \qquad \textbf{Eq 2.1. 1}$$

Where E_0 is the electron energy just before it interacts with the target element, $S_{rad}(E)$ is the radiation stopping power and $S_{total}(E)$ is the total stopping power of the electron with energy E in the target. The integration symbol indicates that the Bremsstrahlung yield is integrated over all electron energies in the electron beam with electron fluence $\Phi_e(E)$. The stopping power is defined as the energy loss per unit thickness of the medium measured in g/cm^2 as the electron traverses a medium. When the electron loses its energy through ionisation with other atomic electrons, the corresponding stopping power is referred to as ionisation stopping power (S_{ion}). When the electron energy is lost through the Bremsstrahlung process, the stopping power is referred to radiation stopping power (S_{rad}). S_{total} is the sum of S_{ion} and S_{rad}. The derivation of the radiation and ionisation stopping power equations require both relativity and quantum mechanics theory. The details of the derivation should be referred to Johns and Cunningham 1983, and references within.

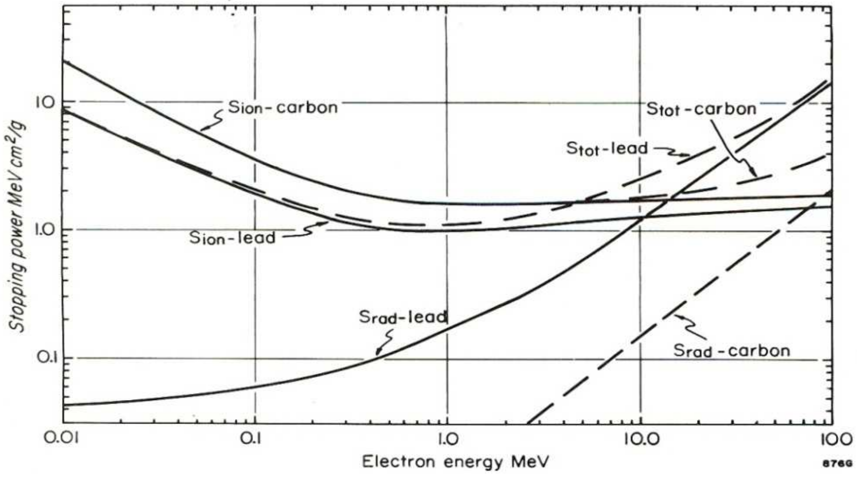

Figure 2.1.2: Ionising and radiative stopping power as a function of initial electron energy and absorber materials (Johns and Cunningham 1983).

It can be observed from figure 2.1.2 that the radiation stopping power not only depends on the energy of the impinging electrons but it also depends on the atomic number Z of the target element. The Bremsstrahlung yield therefore depends on the electron energy and the atomic number of the target element as well. Figure 2.1.2 also shows that below certain energy in the interaction with a medium, the electron loses more energy through ionisation process than through the Bremsstrahlung process for both low and high atomic number elements such as carbon and lead respectively. However, the ratio of the radiation stopping power and the total stopping power is higher for high Z elements compared to low Z elements for an electron energy range between 0.01 and 100 MeV and this ratio also increases with energy. Therefore high atomic number elements such as tungsten and copper or a mixture of them are used as X-ray target materials.

The direction and spatial distribution of the accelerated electron beam has a significant effect on the angular distribution of the generated X-ray beam. All linac designs are such that the trajectory of electron beam is perpendicular to the surface of the X-ray target. The spatial distribution of the electron beam is not accurately known. Measured data (Sheikh-Bagheri, Rogers et al. 2000) suggests that there is a spatial spread of the electron beam which resembles the Gaussian distribution in figure 2.1.3. The X and Y direction are often referred to the cross-plane and in-plane respectively. The cross-plane is perpendicular to the direction of the beam and the patient table and the in-plane is also perpendicular to the beam direction but parallel to the patient table. The Full Width at Half Maximum (FWHM) or the magnitude of the spread of several linear accelerators at the Royal Adelaide Hospital radiotherapy department was found to be between 1-2 mm based on measurement using the pinhole cameral method. When modelling the X-ray beam, it is the FWHM and the energy of the electron beam that are adjusted in order to obtain the best match between the measured and simulated beam profiles and percentage depth dose curves.

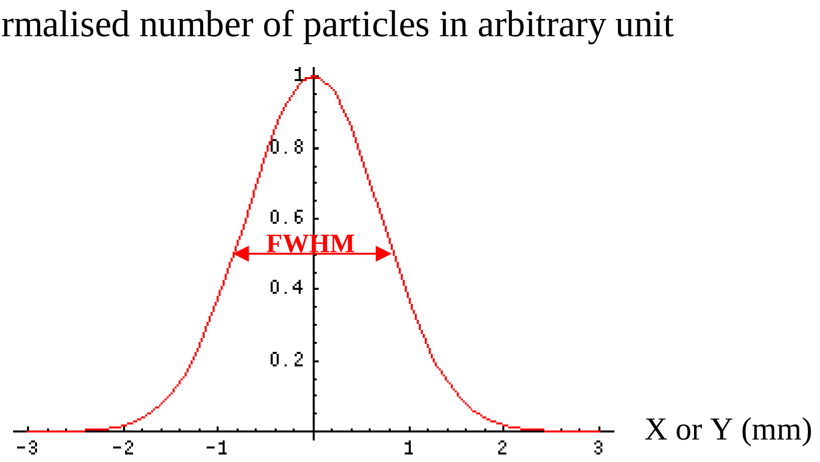

Figure 2.1.3: 1 dimensional Gaussian distribution representing the spatial spread of the electron beam before hitting the X-ray target (http://mathworld.wolfram.com/GaussianFunction.html).

Following the X-ray target is the primary collimator. It is designed to absorb all unwanted sections of the X-ray field. Tungsten is often used for this component because of its high atomic number and thus high attenuation coefficient. The photon beam exiting the primary collimator does not have uniform spatial intensity. It has an angular distribution that is strongly peaked forward in the same direction as the initial electron beam before entering the X-ray target (top section of figure 2.1.4).

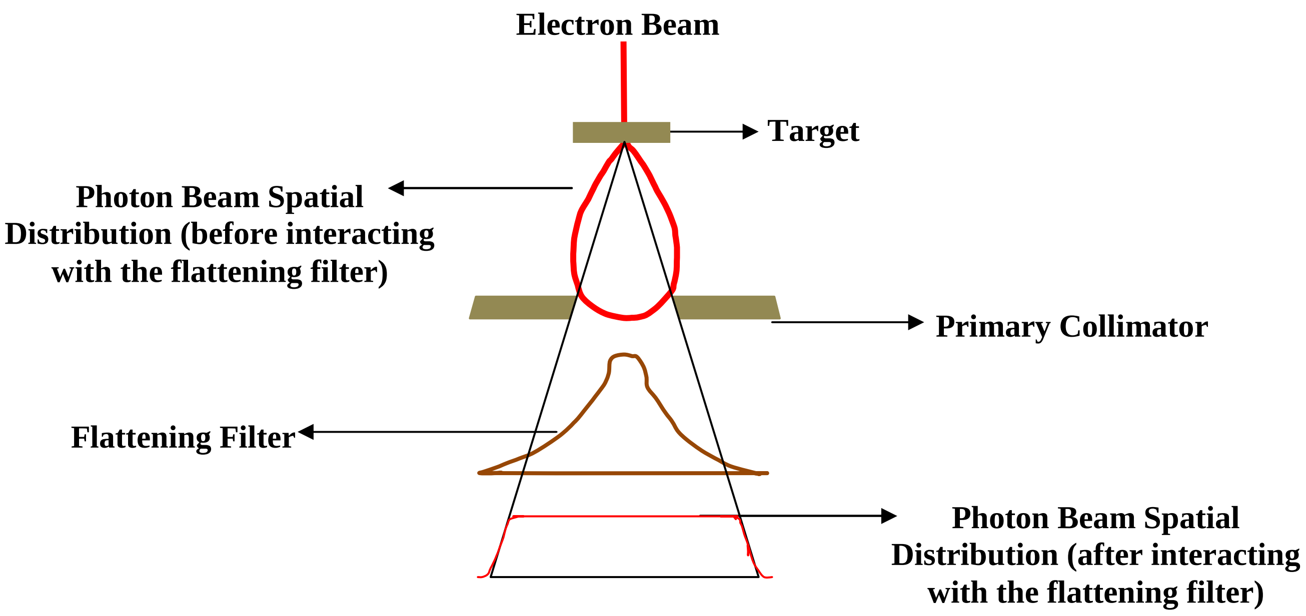

Figure 2.1.4: Angular distribution of the photon beam before and after entering the flattening filter.

A more uniform angular distribution of the photon beam can be achieved by passing it through a flattening filter. The general shape of the flattening filter is shown in figure 2.1.4. The material required for the flattening filter is lead or copper depending on the beam energy or manufacturer. The dose distribution is very sensitive to the position of the flattening filter. A small misalignment of the flattening filter within a few millimetres in the linac head would cause large variations in the dose distribution. The flattening filter also has another effect on the beam called beam hardening. The details of this effect will be discussed in later chapters.

Following the flattening filter are the monitoring system and the mirror. The monitoring system consists of four quadrants of ion chambers which are fixed in the beam direction (refer to figure 2.1.1). The ion chambers measure the radiation beam dose output in terms of Monitor Units (MU) and the radial and transverse symmetry of the radiation beam. The transverse and radial directions are perpendicular to each other and also perpendicular to the direction of the radiation beam. The monitor chamber system also has a mechanism to provide feedback to disable the linac from beaming due to the lack of symmetry and or when the required number of MU is delivered.

The mirror underneath the monitor chamber system is used to project light from the optical source to replicate the shape of the radiation field. The angle and position of the mirror and the light source are carefully aligned so that the light field is coincident with the radiation field. These components are designed so that they have minimal effect on the radiation beam. From the modelling perspective, these components are included in the linac head model for consistency reasons only. The effect is small compared to other components in the linac head. Modelling errors related to these components can be difficult to diagnose.

Below the mirror are two sets of jaws which constitute a secondary collimator (refer to figure 2.1.1). These are movable tungsten blocks with sufficient thicknesses to shield out the unwanted radiation and effectively define the radiation field size. The top jaws move in the in-plane direction and the bottom jaws move in the cross-plane direction. These jaws are designed to move in an arc shape to account for the divergence of the X-ray beam. This is not a concern for modelling because the jaws are static in the simulation.

One of the objective in producing X-rays for clinical purposes in radiotherapy is to have a spatially uniform fluence and a well collimated radiation beam in a reference plane that is perpendicular to the beam axis. Generally, this plane is defined at a depth of 10 cm in a water phantom. The surface of the water phantom is 100 cm away from the X-ray source. When this condition is met, the radiation beam will produce a uniform dose distribution across the reference plane. This objective is met by having the flattening filter, primary and secondary collimators components in the linac head.

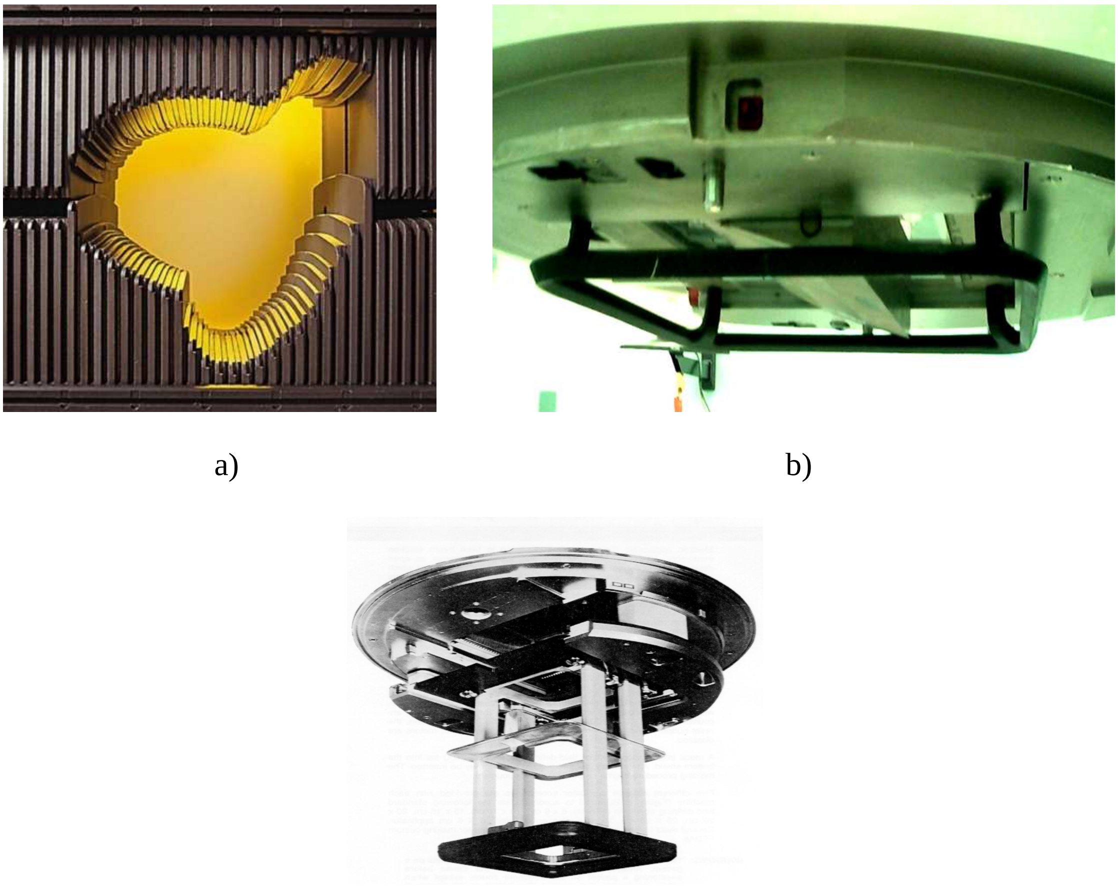

a) b)

c)

Figure 2.1.5: Beam shaping device for complex treatment targets in radiotherapy: a) the Multi-Leaf Collimators MLC (view from below) is a great advancement replacing the use of physical blocks for beam shaping purposes. b) Physical wedge is often used in breast treatment to create a desirable dose gradient corresponding to the angle of the wedge. c) An electron applicator mounted to the collimator to shape the electron beam. The field size of the electron beam is defined by the length and width of the applicator.

The structure of the linac head described above contains only the basic components that are of importance for this project. There are other components such as the Multi-leaf Collimators (MLC) and Wedges which can also be mounted to the head. These components are generally made of Tungsten and steel alloys (figure 2.1.5). They provide means to customise and conform the shape of the radiation beam for complex treatment targets such as in the breast, prostate, head and neck radiotherapy. Modern linacs are also capable of producing both X-ray and electron beams. In the electron mode, the X-ray target and the flattening filter are replaced by a pair of electron scattering foils which are mounted on a carousel (refer to figure 2.1.1). This component causes scattering of the narrow electron beam to create clinically wide uniform dose distribution at the reference plane. In the electron mode, the electron cone is mounted to the collimator (figure 2.1.5 c) to define size and shape the beam closer to the patient plane.

2.2 Electronic Portal Imaging Device

Electronic Portal Imaging Devices (EPIDs) are used in external beam megavoltage radiotherapy for position verification purposes. The EPID consists of a two dimensional array of detectors which is mounted on the arm attached to the gantry and extracts underneath the patient. In contrast to film which requires processing, the EPID produces an on-line digital image of the patient anatomy for direct position verification against the planned treatment position using Digitally Reconstructed Radiographs (DRRs). Three different variations in the design of the EPID evolved since the 1980s. The first design was introduced by Norman Baily in 1980 (Baily, Horn et al. 1980). The design is based on the use of fluoroscopic medium to produce a megavoltage image; this is the principle of the camera-based fluoroscopic system. The second design is known as the Scanning Liquid Ion Chamber (SLIC) system which was developed by van Herk and Meertens in 1988 (van Herk and Meertens 1988). The third design is known as the amorphous silicon (a-Si) solid state detector or simply a-Si EPID. This design was developed at the John Hopkins University in 1982 (Taborsky 1981). The detectors are made from solid state silicon alloys such as amorphous silicon (Antonuk, Boudry et al. 1992) and amorphous selenium (Zhao, Blevis et al. 1997). The detail description of the camera-based and a-Si EPIDs has been discussed widely in literature. The aim of this chapter is to provide an overview of the structure and the physics behind the SLIC EPID. The geometry and material structures of the SLIC EPID that were used for modelling in this project will be described in more detail. Furthermore, the use of EPIDs for in-vivo dosimetry will be discussed and the calibration procedure that was used to derive the transmitted dose in this project will be described.

2.2.1 Basic Components and Structures of the EPID

The Varian Portal Vision MK2 SLIC EPID model was used in this project. In general, it has two major components: the Control Unit and the Megavoltage “Camera” Cassette as illustrated in figure 2.2.1.1.

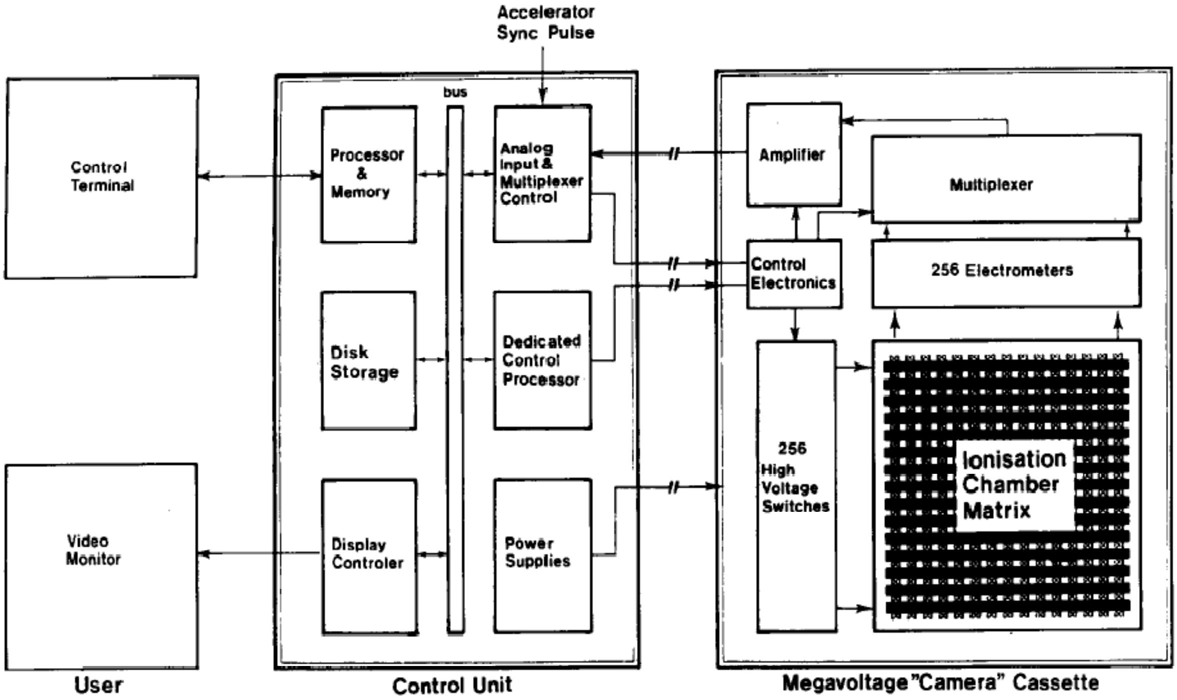

Figure 2.2.1.1: Schematic diagram of the internal structure of the EPID consisting of the Control Unit and the Megavoltage “Camera” Cassette (Boyer, Antonuk et al. 1992).

The Control Unit has a built-in microcomputer with essential data analysis programs and sufficient memory to store and process signals from the electrometers in the Camera Cassette.

The Camera Cassette has the following components: control electronics system, a 256-channel electrometer, a 256-channel high voltage switch and an ionisation chamber matrix. The ionisation chamber matrix is formed by 256 electrode plates and

256 high voltage plates positioned at right angle to each other. The electrode plate and the voltage plate are connected to the electrometer and high voltage switch respectively forming a single ionisation chamber at every cross point. This arrangement creates a total number of 256x256 image pixels over a surface area of 32.5x32.5 cm^2. The maximum resolution is thus 0.127 cm. The ionisation chamber matrix is submerged in 0.08 cm thick Iso-octane liquid film acting as the radiation sensitive layer of the EPID. The sensitive layer is sandwiched between two 0.08 cm thick Printed Circuit Board (PCB) and with an additional 0.1 cm thick radiation build-up layer made of Plasto-ferrite on top of the PCB layer. The structure is further protected by a pair of 0.8 cm thick Rohacell foams and 0.08 cm thick PCB on the outer boundary. An enlarged side view of an ionisation chamber matrix from Varian manufacturer is shown in figure 2.5.1.2 (Spezi and Lewis 2002). This structure was modelled by the Monte Carlo program DOSXYZnrc in the current work.

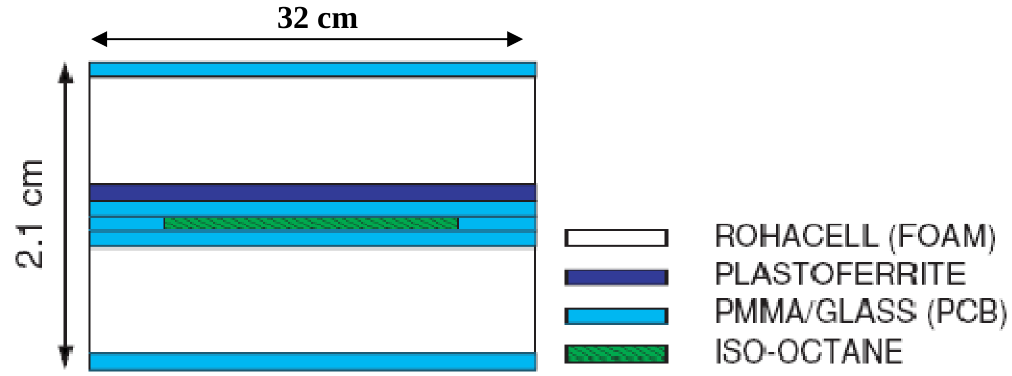

Figure 2.2.1.2: Side view of the EPID that was modelled by DOSXYZnrc program in this project (Spezi and Lewis 2002).

2.2.2 Physics and Operation of the EPID

Image taken by the EPID is the result of a high energy X-ray beam (mega voltage range) passing through and interacting with the EPID sensitive layer containing the ion chamber array. The differences in the attenuation of the photons due to varying densities and thicknesses in the object give rise to different grey scale or EPID pixel values which form an image. The pixel value is proportional to the number of electrons or ions formed in the ion chambers as a result of interactions of the attenuated X-ray beam with the sensitive medium of the EPID. The ion chambers are used to detect ions or electrons. Studies have shown that the ability to detect the signal in a particular period of time known as the Sampling Efficiency is greatly improved when detecting electrons (Boyer, Antonuk et al. 1992)]. An electron being a lighter particle moves a lot faster than an ion and thus has greater mobility (~10^5 times). Therefore in a particular period of time more electrons can be detected giving rise to the Sampling Efficiency of up to 100% compared to 10% of that from ions (Boyer, Antonuk et al. 1992)]. Apart from electron mobility, other important parameters which determine the Sampling Efficiency and thus contribute to the quality of the EPID's image are: radiation pulse frequency and the electron's life time in the liquid called the recombination time.

The mobility determines the time, called drift time, that it takes the electrons to reach the electrode plate of an ion chamber. The drift time determines the period for switching the high voltage from one ion chamber to another. The switching period is set to be greater than the drift time so that all of the free electrons generated would be detected. The system is set to make repeated measurements along every row and the signals are averaged over a number of measurements until desirable image is obtained. The maximum number of measurements is determined by the radiation pulse frequency. For example, a typical linear accelerator pulse frequency is between 200-400 Hertz. The common scanning mode of the EPID takes 20 ms to measure signals from 256 electrodes. Therefore, the signals can be averaged up to a maximum of eight times. Electrons created in the liquid can be lost through recombination with ions. The time taken for electrons to recombine defines the electron lifetime. Therefore to achieve a high sampling efficiency, it is important that there is sufficient voltage across the ion chamber array (~300 V) (Herman, Balter et al. 2001) to ensure that the electron's mobility in the liquid is large so that the drift time is shorter compared to the electron lifetime.

2.2.3 Factors determining the Quality of the EPID

The quality of an Electronic Portal Image (EPI) can be assessed through a number of quantities. The important ones which will be discussed in this section are contrast, Signal to Noise Ratio (SNR), Detective Quantum Efficiency (DQE) and photon scatter. The quality of an EPI from the megavoltage X-ray beam and the kilovoltage X-ray beam will also be compared.

Contrast

The contrast of an image represents how well one object can be distinguished from another or from the background. It is defined as the ratio of the signal difference to the mean signal as shown mathematically in equation 2.2.3.1 (Herman, Balter et al. 2001). S_{p1} is the primary photon fluence (number of particles per unit area or signal) from object 1, S_{p2} is the primary photon fluence from object 2 and the S_{scat} is the scattered photon fluence.

$$C = \frac{signal\,difference}{mean\,signal} = \frac{S_{p2} - S_{p1}}{\frac{1}{2}\left(S_{p2} + S_{p1} + 2S_{scat}\right)} \qquad \textbf{Eq 2.2.3. 1}$$

Equation 2.2.3.1 clearly shows that the greater the difference in the radiation attenuation between the two objects, the better the contrast. In kilo-voltage imaging, much higher contrast image can be acquired because the attenuation is roughly proportional to the third power of the atomic number (Z^3). Megavoltage imaging on the other hand gives lower contrast because the attenuation is nearly independent of Z due to dominant Compton interaction of MV X-rays with the medium.

Signal-to-Noise Ratio (SNR)

The contrast of an image alone does not completely describe the quality of an image. It becomes meaningless when there is a lack of signal. One of the most important factors that determine the quality of an image is the signal-to-noise ratio. It is simply defined as the ratio of signal amplitude to noise. The noise comes from two main sources; the dark current from the electronic components of the EPID and from the statistical nature of the interactions between the photons and the media. The statistical nature can be described by Poisson’s statistical theory, which implies that the mean number of electrons (signals) detected is equal to the variance σ^2, where σ is the standard deviation or the noise. The noise can be calculated as follows (Prince and Links 2006):

$$\sigma = \sqrt{S_{mean}} \qquad \textbf{Eq 2.2.3.2}$$

The scatter photons also have the effect of reducing the SNR because the detecting system is unable to distinguish whether the signal comes from the primary photons or scattered photons. Similar to the contrast, the signal-to-noise ratio is low for megavoltage beam. Because much fewer electrons are produced in the interaction compared to kV beams. Table 2.2.3.1 shows that for the same dose, the SNR for kV beam is about 75 times that of an MV beam. However, it is possible to improve the SNR for the megavoltage beam by increasing the incident photon fluence which will effectively increase the dose to an object as well. A paper by Motz and Danos in 1978 showed that for a 2 MV beam, the minimum dose for which the image is visible is about 1 cGy.

Energy	Diagnostic (50 kV)	Therapeutic (2 MV)	Therapeutic (2 MV)	Therapeutic (2 MV)	Therapeutic (2MV)
Patient dose	0.05 cGy	0.05 cGy	1 cGy	10 cGy	55 cGy
SNR	71	<1	4.8	15	35

Table 2.2.3. 1: Calculated SNR and patient doses at diagnostic and therapeutic photon beam (Herman, Balter et al. 2001).

Quantum Detection Efficiency

Quantum Detection Efficiency (QDE) describes how effectively the image receptor receives information carried by X-rays. QDE takes into account the number of particles detected by the imaging system that has direct contribution to the signal. For the SLIC EPID, it is the design of the radiation sensitive layer (Iso-octane) and the ion chamber matrix that affects the quantum detection efficiency of the system. The QDE can be improved by designing thicker Iso-octane layer or electrode plates with greater surface area. However, the modifications would result in poorer spatial resolution. For this reason there must be a compromise between the QDE and the spatial resolution of the image.

2.2.4 EPID for In-Vivo Dosimetry

While EPID is an excellent tool for patient position verification, its application in in-vivo dosimetry has also been explored extensively. The first report of the use of an EPID for dosimetry application was published in the 1980s (Leong 1986). The author recognised that when the EPID is in integral mode of operation, it behaves like an array of dosimeters. Further investigation had led the author to propose that such a dosimeter system can be used as an exit dose monitoring system. Based on the topology of the patient from the CT scan, the patient total exit dose can be calculated. The comparison between the calculated and measured total exit dose can be used to identify large errors that might have inadvertently occurred during the treatment fraction. For instance, a wedge displaced in the course of treatment fraction due to insecure mounting may have not been detected by a record and verify system.

Ultimately, what is most important is the dose to the treatment target or their internal structures. In the area of study to predict the dose inside the patient anatomy based on the transmitted dose (transit dosimetry), this dose is often referring to a midline dose. The idea of deriving the midline dose from the patient exit dose was proposed by Leunen in 1990 (Leunens, Van Dam et al. 1990) based on the early work of Rizotti in 1985 (Rizzotti, Compri et al. 1985). The idea proposed by Leunen's group was tested using film by Huyskens (Huyskens, Van Dam et al. 1994). The use of film for calculating the patient midline dose was replaced by the EPID in the work carried out by Hansen (Hansen, Evans et al. 1996). In this work, Hansen obtained the total energy fluence of a treatment field using a calibrated EPID. The primary fluence, $\Phi(E,\mathbf{r})$, was extracted by subtracting the scatter fluence from the total fluence and back-projected into the patient mid-plane. E is the total energy of the particle at the interaction point and $\mathbf{r}$ is its vector position in the patient mid-plane. In order to produce an accurate fluence map, image matching was performed. In this process, the portal image which contains the total fluence was aligned with the reference image obtained from the digitally reconstructed radiograph. The primary fluence map in the patient mid-plane was converted into TERMA (total energy released per unit mass in the medium), $T(\mathbf{r})$, via the mass energy absorption coefficient $\mu/\rho(E,\mathbf{r})$ and the total energy E as in equation 2.2.4.1 (Hansen, Evans et al. 1996).

$$T(\mathbf{r}) = \mu/\rho(E,\mathbf{r}) \times E \times \Phi(E,\mathbf{r}) \qquad \textbf{Eq 2.2.4. 1}$$

The absorbed dose, $D(\mathbf{r})$, at the mid-plane was then calculated by convolving the energy deposition kernel, $H(E,\mathbf{r})$, over all source vector positions, $\mathbf{s}$, with the TERMA as shown in equation 2.2.4.2 (Hansen, Evans et al. 1996):

$$D(r) = T(r) \otimes H(E,r-s) \qquad \textbf{Eq 2.2.4. 2}$$

The method presented by Hansen was performed for single field irradiation of a humanoid phantom. Agreements of about 1.5% and 2% were found for comparison between the measured EPID dose and the dose prescribed by the treatment planning system and measured by TLDs respectively. For clinical feasibility assessment of the method, four fields irradiation of a patient in the pelvic region was also performed. However, the quantification of the agreement between this transit dosimetry method and the treatment was not carried out in this study.

The calculation of the mid-plane dose in the patient was also performed by Boellaard in 1998 (Boellaard, van Herk et al. 1996). In Boellaard’s method, only the primary component of the transmitted dose was used to calculate the exit dose. The mid-plane dose was then calculated by applying three correction factors to the exit dose. The first factor corrects for the attenuation between the mid-plane and the exit plane based on the equivalent path length. This correction factor is obtained by taking two EPID images; one with the patient and the other without the patient in the radiation field. The second factor corrects for the divergence based on the inverse square law. The third factor corrects for the difference in the scatter conditions between the mid-plane and the exit plane. The method used by Boellaard relied only on the transmitted dose at the EPID plane but not on the energy deposition kernel and the treatment planning data as in Hansen’s method. In this way, the verification of delivered dose is more independent. Boellaard’s method was verified by performing point dose measurements on the central axis and in the midplane in both homogeneous and inhomogeneous phantoms. Agreement within 2% was found for verification in a homogeneous phantom. In the case where inhomogeneity exists, similar level of agreement was found only if small inhomogeneity is present in a homogeneous phantom and when large radiation field size (>10x10 cm^2) was used. In the present of a large inhomogeneity in a homogeneous phantom, agreement of around 8% was observed when small field size was used. These agreements were found to be better for low energy (4 MV) and large field size than high energy (18 MV) and small field size. Boellaard’s method has some disadvantages. When used for patient dosimetric verification, it is only appropriate for treatment site with small inhomogeneity such as the pelvic region. Also, additional non-patient EPID images are required for every measurement.

The application of transit dosimetry using an EPID was also found in an Intensity Modulated Radiotherapy (IMRT) dose verification procedure (Wendling, Louwe et al. 2006). In this paper, Wendling and others reported an improved method for calculating the mid-plane dose, which was originally developed by Boellaard et al in 1998 (Boellaard, van Herk et al. 1996). The improved method provides more accurate scatter correction in the penumbra and the tail regions of the beam profile. The improved accuracy of this method is essential for dose verification in IMRT quality assurance procedure. The reason for this is because IMRT plan is delivered with multiple segments which generate many low dose regions and steep dose gradients in each treatment field. Comparison was made with film for five-field IMRT for prostate. The authors observed excellent agreement in 2D analysis with dose and distance criteria of 2% and 2 mm respectively.

van Zijtveld and others also reported the application of transit dosimetry in their IMRT Quality Assurance (QA) program for over 270 patients (van Zijtveld, Dirkx et al. 2006). In this work, the fluoroscopic EPID was used to measure the dose map in the EPID’s detector plane. The algorithm for calculating the transmitted dose from the measured electronic portal image signal was derived based on the method published by Pasma (Pasma, Kroonwijk et al. 1998). The measured dose map is then compared with the predicted dose map which was calculated by the Cadplan treatment planning system (TPS) in the EPID’s detector plane. The main purpose of Zijtveld’s work was to develop an automatic system that can verify and approve an IMRT plan prior to treatment. The 2D dose map analysis was performed using the dose and distance to agreement criteria of 3% and 3 mm respectively. Out of 270 patients, a study group of 75 patients were selected. The analysis for this study group showed that the mean gamma value inside the field was 0.43 ± 0.13 and only 6.1 ± 6.8% of pixels had a gamma value larger than one.

Comparison between the measured and the calculated transmitted dose maps or the mid-plane dose map are essential for detecting dose delivery errors due to the deviation in the cGy/Mu, machine beam profiles, errors in beam data transfer and variations in the patient anatomy between the planning and treatment stage. However, an error in the calculated MU cannot be detected by these means because the same number of MU is used in both the planning and treatment stage (Pasma, Kroonwijk et al. 1998). Pasma et al 1999 derived a method to verify the calculated MU based on the measured portal dose map from a calibrated EPID (Pasma, Kroonwijk et al. 1999). The dose at a depth of 5 cm in a patient resulting from the prescribed dose of 2 Gy at the isocentre was verified using the measured dose derived from the transmitted dose in the calibrated EPID. The measured and calculated portal dose map was also compared to determine the cause of the MU difference. This MU verification method has been applied for 115 prostate cancer patients. Out of which, 7 patients were found to have the MU value differences greater than 5%. It was found that the differences in the MU value were caused by the presence of large gas pockets in the rectum during the planning CT scanning.

The advantage of using an EPID as a dosimetry system is that it provides 2D dose distribution as opposed to TLD or diode dosimeters where only a few points can be measured (Broggi, Fiorino et al. 2002). The availability of the 2D dose distribution offers better dose assessment in regions of high dose gradients. This is especially useful for dose verification purpose in Intensity Modulation Radiotherapy. In addition, the EPID dosimetry system is capable of providing real-time data over the course of treatment and therefore it is less time consuming than for example film (van Zijtveld, Dirkx et al. 2006).

It can be seen that EPIDs can produce important delivered dose data that can be used for in-vivo dosimetry. Transmitted dose is a starting point for methods deriving the patient mid-plane dose distributions. In order to obtain a transmitted dose map, it is essential that the EPID is calibrated carefully. A particular dosimetric calibration method for an EPID will be described in the following section.

2.2.5 Calibration Procedure for Portal Dosimetry

The use of EPIDs for dosimetry purposes was introduced in section 2.2.4. It is well known that the EPID’s signal is related to the dose rate of the linear accelerator (Kirby and Williams 1993; Essers, Hoogervorst et al. 1995; Boellaard, van Herk et al. 1996; Parsaei, el-Khatib et al. 1998; Greer and Popescu 2003; Mohammadi and Bezak 2006). For this reason, it is essential that the EPID is calibrated in order to provide an accurate measurement of the transmitted dose map. The calibration procedures have been carried out in a number of studies and a common relationship between the dose rate and the pixel value from the SLIC EPID was derived as follow (van Herk 1991; Kirby and Williams 1993; Essers, Hoogervorst et al. 1995; Boellaard, van Herk et al. 1996; Parsaei, el-Khatib et al. 1998):

$$PV = a\sqrt{\dot{D}} + b\,\dot{D} \qquad \textbf{Eq 2.2.5. 1}$$

$\dot{D}$ is the radiation dose rate delivered at a particular distance from the source, a and b are parameters that depend on the linac repetition rate.

Mohammadi and Bezak, 2006 performed the verification of the relationship shown in equation 2.5.4.1 and found that their measured data indicated a trend that was best described by equation 2.5.4.2

$$PV = a(\dot{D})^{b} \qquad \textbf{Eq 2.2.5.2}$$

The relation described by equation 2.5.4.2 was used to derive the transmitted dose in this project. The calibration procedure performed by Mohammadi and Bezak at the Royal Adelaide Hospital, Medical Physics Department will be the subject of this section.

The experimental work was carried out using the 6 MV beam from a Varian 600C/D accelerator, the Portal Vision MK2 Varian SLIC EPID and an ion chamber. The pixel value on the beam central axis was first measured using a 10x10 cm^2 field at the iso-centre. The dose rate was varied by moving the EPID panel to distances between 110 and 160 cm from the source. These measurements were repeated for a range of linac repetition rates between 100-600 $MUmin^{-1}$. In order to reduce the statistical uncertainty, the pixel values were averaged over an 8x8 pixel square around the central axis. This averaged pixel value was then compared with the dose rate measured under the same conditions by an ion chamber. The ion chamber dose rate was obtained by calculating the ratio of the dose over the EPID acquisition time. The pixel value was plotted against the dose rate and interpolated using the power interpolation method to derive the relationship described in equation 2.2.5.2.

The EPID is designed to acquire images of the patient anatomy. It is therefore calibrated using the manufacturer standard procedure to produce uniform pixel response over the entire detector matrix for an open field irradiation. Profile A of figure 2.2.5.1 shows an example of the EPID response profile for a 15x15 cm^2 open radiation field. For dosimetry purposes, it is essential that the EPID is calibrated to produce a true dose profiles such as profile B of figure 2.2.5.1, also obtained for a 15x15 cm^2 open field irradiation.

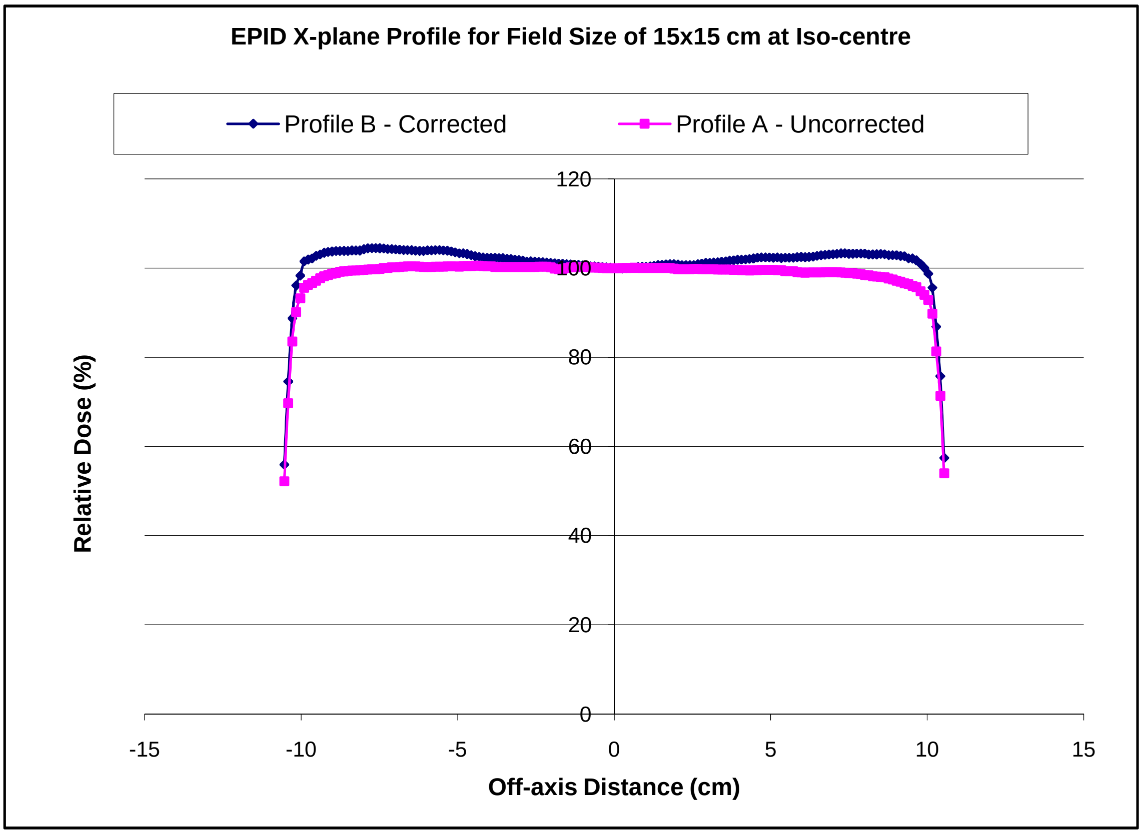

Figure 2.2.5.1: Uncorrected EPID profile (profile A) and corrected EPID profile (profile B) which was performed by the use of EDR2 film.

The features on both sides of profile B in figure 2.2.5.1 are called the horns of the dose profile. These horns can be produced by applying a 2D-Dose correction factor. Mohammadi and Bezak derived this correction factor by the use of the Extended Dose Rate, EDR2 film. The measurements were first carried out with film for field size of 10x10 cm^2 at the iso-centre and a range of SSDs from 110 to 130 cm. The measurements were repeated using the EPID with the same setup. The correction factor for each elemental detector, i and j of the EPID was then calculated as follows:

$$CFM_{i,j} = D_{i,j}\ (\text{EDR2 film}) / D_{i,j}(\text{EPID}) \qquad \textbf{Eq 2.2.5. 3}$$

For two dimensional correction, CFM is the correction factor matrix. The dose in the EPID detector i and j, $D_{i,j}$(EPID), is calculated from equation 2.2.5.2 and $D_{i,j}$ (EDR2 film) is the dose in the i and j pixel of the film which had been resized to the size of the EPID pixel.

Based on the above calibration procedures, Mohammadi and Bezak were able to derived the dose at each detector of the EPID ($D_{i,j}$(corrected)) from the measured EPID dose $D_{i,j}$(measured) as follow:

$$D_{i,j}(\text{corrected}) = D_{i,j}(\text{measured}) \times \text{CFM}_{i,j} \qquad \textbf{Eq 2.2.5. 4}$$

When using the EPID as a dosimetry system, it is important to note the long-term and short-term stabilities of the dose response of the EPID. Essers et al 1995; 1996 and Louwe et al. 2004 found in their studies that the long term and short term stabilities of the SLIC EPID was better than 1% over two years. Furthermore, the bulging effect must be taken into consideration when the SLIC EPID is used for dosimetry at gantry angles other than 0^o. The effect of gravity force on the dielectric liquid can cause significant variation on the EPID signal (van Herk and Meertens 1988; Van Esch, Vanstraelen et al. 2001; Chin, Spezi et al. 2003).

CHAPTER 3

MONTE CARLO MODELLING IN TRANSMITTED DOSIMETRY

3.1 Monte Carlo Simulation Method

EGSnrc software was used to perform all dose calculations in the current project. The software uses Monte Carlo (MC) techniques to calculate dose deposition due to X-ray interactions with matter. As mentioned in the previous chapter, Monte Carlo is the most accurate method for dose calculation. There are two main reasons for this: The first reason is because all possible particle interactions (events) are considered and accounted for in the dose calculations right from the entrance to the exit point in the region of interest. Every possible interaction that has significant contribution to the dose at subsequent calculation points is recorded. This methodology is known as the "First Principle" in model based dose calculations. The second reason is as follows: the principles of quantum mechanics imply that the type of particle interaction is governed by probability. In other words, even if the property of a medium and the energy of a particle are known exactly, the type of interaction as well as the amount of enegy transfer that would occur is still uncertain. The probability that a particular interaction would occur depends on the particle energy and the property of the medium. Because of the probabilistic nature of particle interaction, it is best to use random numbers to determine the initial interaction that would occur to a particle. The likelihood of a particular interaction to occur is determined by the interaction cross-section. The use of random numbers to make decisions for a possible interaction or event is the basis of Monte Carlo method. In this chapter the principle behind Monte Carlo method will be described in detail (Metcalfe and Kron 1997).

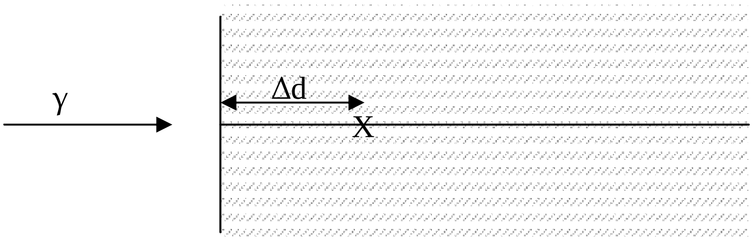

Figure 3.1. 1: A 2 MV photon is incident on a medium. The first interaction point is X at a mean free path of Δd away from the surface.

To illustrate the principle of Monte Carlo, let us imagine a 2 MeV photon beam incident on a medium as shown in figure 3.1.1. In order to calculate the dose at point X, the mean free path, λ of a photon is first calculated. The mean free path is a distance between two points in a medium that a photon travels without interaction. Both of these parameters depend on the total interaction cross-section, σ_{total}, of a photon, which in turn depends on the photon energy and the properties of a medium. The total interaction cross-section is the sum of all cross-sections corresponding to every interaction that may occur at the point of calculation, that is point X in figure 3.1.1. For a 2 MeV photon incident on a medium, three main interactions important in dose calculation may occur: Photoelectric Effect, Compton Scatter and Pair Production with the corresponding cross-sections σ_P, σ_C and σ_{PP} respectively (Johns and Cunningham 1983). In this example, the total cross-section can be calculated by equation 3.1.1:

$$\sigma_{total} = \sigma_P + \sigma_C + \sigma_{PP} \qquad \textbf{Eq 3.1. 1}$$

The quantum mechanics principle implies that there are always uncertainties associated with determining the type of interaction that may occur. Therefore by the definition of the mean free path, its value is also associated with an uncertainty and this must be incorporated in the calculation. This issue is addressed by including a random number, R_1, in the calculation. Taking both the total cross-section and the random number into account, the mean free path can be calculated by equation 3.1.2 (Metcalfe and Kron 1997):

$$\lambda = \frac{-\ln(R_1)}{\sigma_{total}} \qquad \textbf{Eq 3.1. 2}$$

The value of the random number R_1 is randomly distributed between zero and one by the random number generator. Therefore, equation 3.1.2 implies that λ can have any value from zero to infinity with a mean value of $\frac{1}{\sigma_{total}}$**.** The randomness of the generator can be described by the period or cycle of the generator. One cycle represents the number of times a random number is generated without repeating itself.

For dose calculations EGSnrc uses random number generator called RANLUX with a cycle of 10^{165} (Kawrakow and Rogers 2006).

Once the mean free path is determined, a decision on the type of interaction is made. The Monte Carlo method in EGSnrc handles this by taking the ratio of each individual cross-sections, σ_i and the total cross-section, σ_{total} for all three possible events that are Compton Scattering, Pair Production and Photoelectric Effect (Metcalfe, Kron et al. 2007). This ratio represents the probability of each interaction to occur. In this particular example, the photon has the energy of 2 MeV, Compton Scattering interaction therefore has the highest probability, followed by the Pair Production and then the Photoelectric Effect (Johns and Cunningham 1983). For illustration purposes, let say for example the Compton Scattering has 50% chance of occurring ($\frac{\sigma_{CS}}{\sigma_{total}}$ =0.5), Pair Production have 30 % chance of occuring ($\frac{\sigma_{PP}}{\sigma_{total}}$ =0.3) and Photoelectric Effect have 20% chance of occurring ($\frac{\sigma_{P}}{\sigma_{total}}$ =0.2). The Monte Carlo program determines the type of interaction through the following logical loops:

If $0.5 \le R_2 \le 1$ Compton Scattering occurs

$0.5 < R_2 \le 0.2$ Pair Production occurs

$0.2 < R_2 \le 0$ Photoelectric Effect occurs

where R_2 is also a random number with the same property as R_1.

In this particular example, the interactions occur in a 2D plane and thus the calculation is simple. In a three dimensional space, the dose at point X is contributed by both the primary and secondary components of an X-ray beam (figure 3.1.2). The Monte Carlo program has to make a decision for backward, forward and side scatter. Furthermore, in Compton Scattering and Photoelectric Effect processes, an electron will be produced in a medium. Therefore the electron interactions need to be determined by random number as well. The calculation becomes more complicated and the number of interactions multiply quickly as the photon traverses the medium.

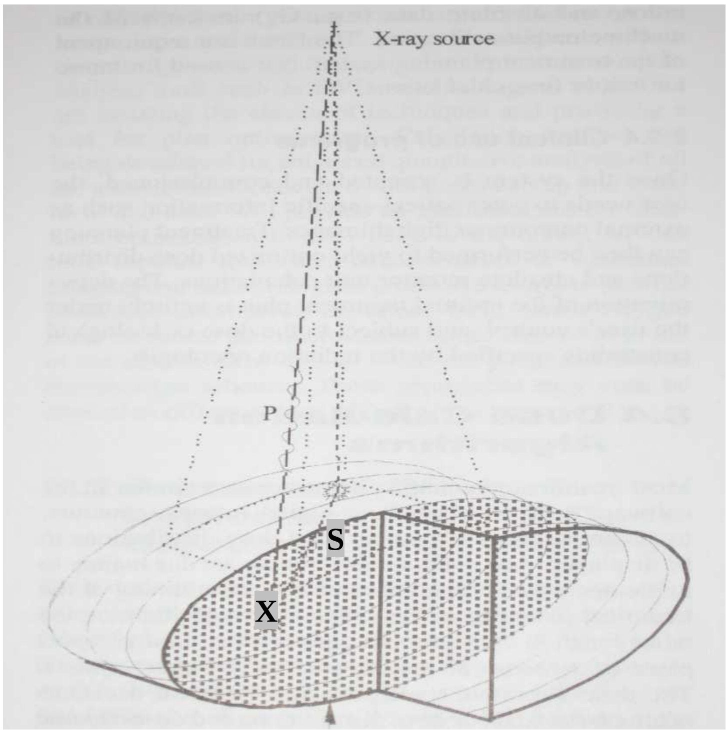

Figure 3.1.2: A photon beam projected onto the 3D volume contains both the primary, P, and secondary, S, components. Both of these components have significant contributions to the dose at point X (van Dyk 1999).

In EGSnrc the dose is calculated in a sub-volume called a voxel instead of a point. The size of the voxel determines the resolution of a particular dose distribution. High resolution dose grid is achieved by decreasing the voxel size and high accuracy in the calculation is achieved by increasing the number of photons in the calculation. Both of these parameters have a dramatic effect on the calculation time in Monte Carlo method. A long calculation time required by Monte Carlo method has been a limitation of this method. EGSnrc provides a few solutions to reduce the calculation time. These topics will be discussed in section 3.2.

3.2 BEAMnrc Program

BEAMnrc is a Monte Carlo (MC) simulation program for modelling radiotherapy sources. The first version was developed in 1987 as part of the OMEGA project to develop a 3-D treatment planning system for radiotherapy purposes (Rogers, Faddegon et al. 1995). The motivation for developing BEAMnrc was that the then commonly used 3D analytical methods based on the monoenergetic point radiation source produced doses with uncertainties of up to 10 % (Mah, Antolak et al. 1989).

The Monte Carlo method on the other hand is capable of simulating the interaction histories of particles (photon, electron and positron) in any media and thus produces the most accurate results if sufficiently large number of particles are used (Rogers, Faddegon et al. 1995). Furthermore, recent rapid developments in computer technology greatly improved the CPU performance, making Monte Carlo programs more suitable for clinical implementation.

BEAMnrc has been continuously improved over the last two decades. It was first created for simulating electron beams and could only be run on a few models of Unix and Linux operating systems. The latest version of BEAMnrc is the multi-platform BEAMnrcMP which can be run on most Unix and Linux and also Microsoft Windows operating systems (Rogers, B. et al. 2007). BEAMnrcMP has far more functions and options allowing for a detailed simulation of almost all radiotherapy sources with greater efficiency. A few common radiation sources which can be modelled by BEAMnrc_MP are: external photon and electron beams, the effects of various components that make up the linac head and internal radioactive sources such as Cobalt 60. Complicated radiation source apparatus such as X-Ray tube and linac head with multi-leaf collimator (MLC) can also be simulated.

In BEAMnrc the simulation begins with a number of particles (positrons or electrons or photons or all three) incident on the surface of the first component module (term used in BEAMnrc to refer to the linac head structure component being simulated) of the linac head at specified angles. All interactions in the medium will be simulated by Monte Carlo method based on random numbers and the physical properties of the particle and the interacting medium. The physical properties such as the charge, mass and energy and their geometrical properties such as angle of incidence on a plane, position of last interaction and current position in the rectilinear coordinate system are stored in a phase space. The user chooses the plane from which the properties of the particle will be recorded and the information will be stored in a phase space file. The simulation of the particle stopped when its energy reached a threshold specified by the variance reduction parameter or when it exits the final component modules.

The structure of BEAMnrc is shown in the flow chart of figure 2.3.1. It indicates the order in which the program follows instructions in deriving the outputs. The first step is to specify the type of component modules in the simulated accelerator. BEAMnrc has 18 built-in component modules. The 2-Dimensional geometrical layout of the component modules SLABS, FLATFILT, CHAMBER, MIRROR and JAWS can be found in Appendix C. The combination of these component modules were used to model the linac head in this project.

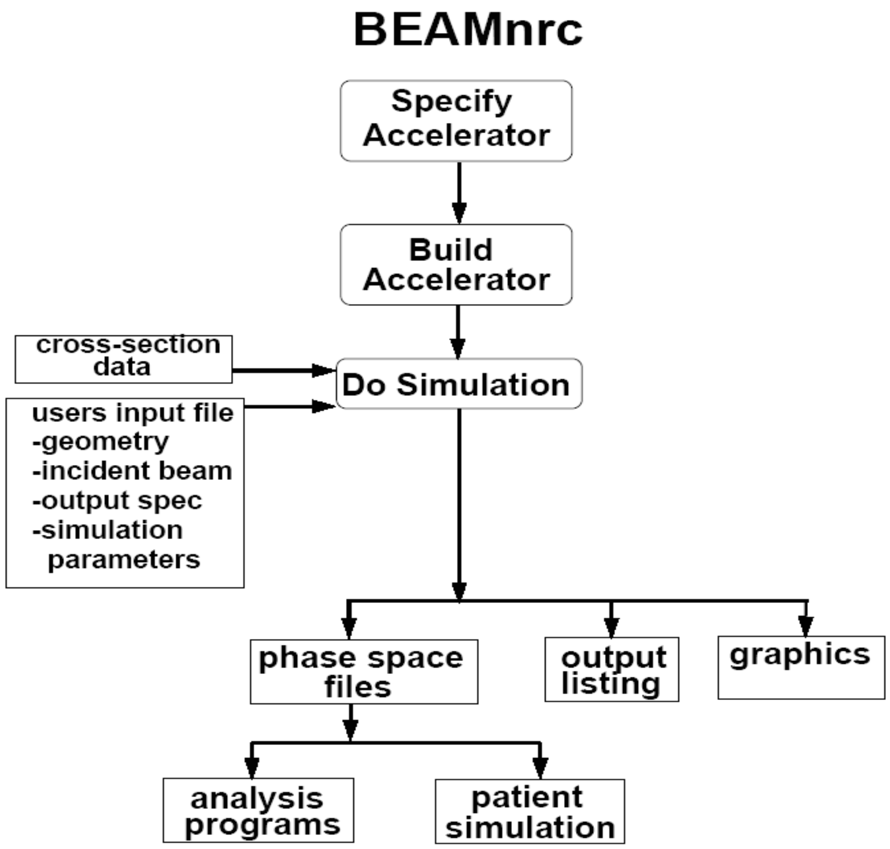

Figure 3.2.1: Illustration of the steps carried out by BEAMnrc in deriving the output (Rogers, B. et al. 2007).

The linac head can be built after the component modules have been selected**.** The building procedure creates a source code and Macros files that are ready to be compiled. The Macros files provides constants and subroutines that will be called by the source code in the compilation process. The product of the compilation process is an executable file which can be run with a given media data file and an input file. The media data files 700icru and 500icru contain the physical properties such as the mass density, electron density and the atomic number of the materials that make up the component modules. Each material has a unique name that must be specified in the input file. The users interact with the program through the input file. The input file has five major sets of parameter files which act as instructions for BEAMnrc to perform the entire simulation. They are Monte Carlo Control, Source Geometrical Configuration, Particle Transport and Component Module Geometrical Configuration and EGS parameters.

Monte Carlo Control parameters include the number of initial particles in the simulation, the random number seed and the maximum simulation time.

The Source Geometrical Configuration parameters specify the properties of the original particles in the simulation. One can choose whether the original particles are photons, electrons or positrons, the energy they carry, their angle of incidence relative to the first component module and their fluence distribution. BEAMnrc has 13 sources with fluence distributions such as the Gaussian, Step and Delta function that can be incident on the plane of the first component module at an angle ranging from 0^o to 360^o. The particle energy can go as high as several hundreds GeV (Kawrakow and Rogers 2006).

The Particle Transport and the EGS parameters describe how a particle behaves in a medium. The Particle Transport parameters also determine when a particle will be eliminated in the phantom. They include ECUTIN, PCUTIN, ESAVE_GLOBAL and IREJCT_GLOBAL. These parameters were implemented into the program to save the simulation time by eliminating those particles that have no significant contribution to the dose in the region of interest. This is called variance reduction method. ECUTIN and PCUTIN are the energies below which an electron and a photon will be discarded in the simulation. ESAVE_GLOBAL is the maximum energy at which an electron will be considered for range rejection as explained below. The process of range rejection is controlled by a parameter called IREJCT_GLOBAL. If the particle energy falls below ESAVE_GLOBAL then IREJCT_GLOBAL will calculate the range of the electron. If the range is not large enough so that the electron can cross the next boundary then it will be discarded and all its energy will be assigned to the absorbed energy in the surrounding region.

Another important variance reduction method used in BEAMnrc is Direct Bremsstrahlung Splitting (DBS) (Kawrakow, Rogers et al. 2004). When this option is selected, the Bremsstrahlung photon will be split NBRSPL times as defined by the user. The algorithm will then determine whether the split photons are aiming inside or outside a circular splitting field at certain distance away from the source. This splitting field is perpendicular to the beam direction and has a radius defined by a parameter called FS in BEAMnrc. The distance between this splitting field and the source is defined by a parameter called SSD. Both FS and SSD are user defined parameters. For those photons that are propagating inside the splitting field, the weighting factor is reduced by a factor of 1/NBRSPL, and the same particle transport algorithms are applied. Photons that are propagating outside the splitting field will be subjected to a selection process called Russian Roulette. Russian Roulette process compares the survival threshold (1/NBRSPL) of each photon outside the splitting field with a random number. A photon will be discarded if the random number is more than its survival threshold. The surviving photons called fat photons will have its weighting factor increased to 1 and will be tracked normally.

The idea of Bremsstrahlung Splitting is to create a uniform particle fluence over a particular area. The average dose in the area is the same because the weighting factor of every split photon is reduced. The simulation takes longer to complete because there are more particles to track. However, the uncertainty of the dose calculation is reduced relatively faster than the increase in the simulation time (Kawrakow, Rogers et al. 2004). The overall efficiency in the simulation is therefore increased. In addition, photons that have no significant contribution to the dose in the region of interest will be eliminated by Russian Roulette. This process further improves the efficiency in the simulation.

The optimal values for the DBS parameters such as the FS, electron splitting plane, Russian Roulette plane and NBRSPL were reported in the paper by Kawrakow et al 2004. It was found that for a 6 MV photon beam, the optimum value for NBRSPL is 1000. The radius of the splitting field should not be much larger than the width of the actual radiation field. For the 10x10 cm^2 field, the splitting field radius of 10 cm is recommended. The Russian Roulette plane should be above the electron splitting plane and they both should be close to the bottom of the flattening filter. With the optimum setting, DBS increases the central axis dose efficiency by a factor 6.4 compared to the previous Selective Bremsstrahlung Splitting (Kawrakow, Rogers et al. 2004) method and even higher compared to non-splitting simulation. The efficiency decreases with the radiation field size and energy.

Direct Bremsstrahlung Splitting technique is not applied just to a Bremsstrahlung photon. It can also be applied to a secondary photon in other interaction processes such as Compton's scattering, pair production, fluorescence excitation and annihilation. The idea is very similar to splitting a Bremsstrahlung photon. The details of the algorithm should be referred to the paper by Kawrakow et al 2004. It should be noted that when DBS is selected, the splitting process will be applied for all processes mentioned above. There is an exception for the splitting of secondary electrons. The user has an option to turn on electron splitting when electron contribution in the region of interest is important.

The EGS parameters determine how the particles move from one position to the other in a phantom. One of the important EGS parameters is the Boundary Crossing Algorithm (BCA). BCA has two options which control whether a particle crosses the nearest boundary between two media in a straight line or at an angle (Kawrakow and Rogers 2006). Other EGS parameters such as Spin Effects, Bound Compton Scattering and Pair Angular Sampling are used to allow effects produced by low energy photons and electrons.

The Geometry parameters describe the positions, shapes, sizes and composition of each of the component module in the simulation. These component modules vary from simple structures such as rectangular slabs or cylinders to complicated structures such as pyramids or tongue and groove structures. The combination of these component modules allows most radiotherapy sources to be simulated by BEAMnrc.

Appendix A.1 documents the BEAMnrc's input file which contains a brief explanation of five different types of parameters mentioned above. Note that the explanations are for a given linac head model. More details of the parameters in the input file can be found in the BEAMnrc_MP user manual (Rogers, B. et al. 2007).

The simulation produces the following outputs: Phasespace, Output Listing, Log and Graphics file. The Phasespace file is a binary file which contains the following information about the particles: the energy, charge, scattered angle and position in a specified plane. The program can also record some history of the particle in the simulation using the LATCH bit setting. With the 29 bits setting it is possible to determine what happened to a particular particle from where it first interacted to where it was eliminated by the IREJCT_GLOBAL parameter. The Phasespace file is useful for programs such as BEAMDP (Ma and Rogers 2007), DOSXYZnrc (Walters, Kawrakow et al. 2007), and DOSRZnrc (Rogers, B. et al. 2007). The BEAMDP program can read and process the data in the Phasespace file to produce the energy spectrum of the previous simulation to produce a new radiation source which effectively requires smaller storage space. The Phasespace file can also be used as a radiation source in DOSXYZnrc and DOSRZnrc. The phasespace file can even be reused by BEAMnrc as the original source of radiation.

Graphics files are also binary files which store necessary data for displaying the geometry and particle tracks in the linac head. A parameter in the Input file called IWATCH controls whether these graphic files will be created. These files can be read in by EGS_Windows (Treurniet and Rogers 1999) to produce a graphical representation of the simulation. Although these graphic files are quite large, they are particularly useful for debugging the Input file and also a convenient way to represent the simulation data.

The Listing file is created to provide a detailed setup of the simulation. This file contains all of the Geometry parameters of each of the specified component module. In addition, the doses, the average energy, the average particle fluence and average angles with respect to the Z-axis are also scored for regions specified by the LATCH’s bits. Furthermore, it provides the simulation time for each batch run and total CPU time for the simulation. The Log file serves the same purpose as the Listing file and in addition reports the uncertainties generated during the execution of the program. The Log file acts rather like a debug file. The Listing and Log files provide a complete record of the simulation which can be used to reproduce the simulation or as a check of the previous simulation.

3.3 DOSXYZnrc Program

DOSXYZnrc is also a Monte Carlo program originally created by Rogers in 1986 for calculating dose in a rectilinear volume element called voxel. Mark Holmes and Blake Walters added Computerised Tomography (CT) reading function in 1996 (Walters, Kawrakow et al. 2007). In 1997, Blake Walters separated this capability so that CT data can be read by another program called CTCREATE (Walters, Kawrakow et al. 2007). In 1999, Blake Walters added an option so that N different jobs can be run on N processors in parallel for a phasespace which has N different components. In 2001, DOSXYZnrc was further modified by Ma et al to include more source routines and a characterised source model. It was then adopted to become part of the OMEGA simulation software package (Walters, Kawrakow et al. 2007).

DOSXYnrc is capable of simulating dose distributions in each voxel in three dimensions. The basis of this program is no different from BEAMnrc. Initially a type of radiation source is chosen to be incident on a region of interest. The type of interaction which occurs will be predicted by the MC method based on random numbers and the physical properties of both the source and the interaction medium. Whereas BEAMnrc is mainly used to determine the physical and geometrical properties of the particle after interacting with a series of component modules, DOSXYZnrc is used to determine the absorbed dose in the interaction region (phantom). Generally BEAMnrc and DOSXYZnrc are used in combination. BEAMnrc is used to calculate the X-ray beam spectrum exiting the linac head and DOSXYZnrc is used to calculate the dose deposited by this beam in a medium.

The execution of DOSXYZnrc is simpler than that of BEAMnrc. After the program has been compiled, two types of input are required to run the simulation. They are Media file and Input file as indicated in the flow chart in figure 2.4.1. The Media file used in DOSXYZnrc is the same as that used in BEAMnrc. The Input file as mentioned previously contains five sets of parameters: Monte Carlo Control, Source Geometrical Configuration, Particle Transport and EGS, and Phantom Geometrical Configuration parameters. These parameters serve the same purpose as in BEAMnrc except that there is no range rejection parameter (IREJCT_GLOBAL).

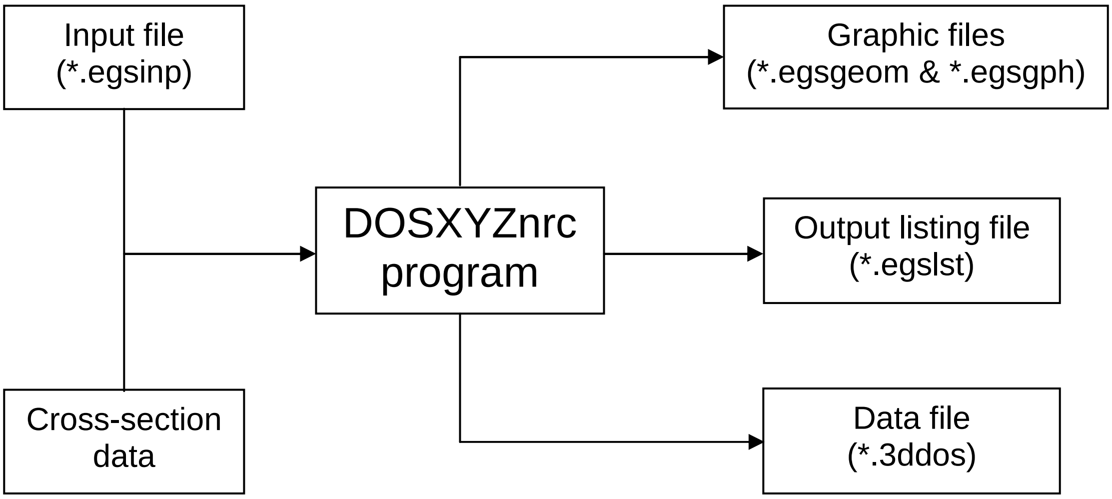

Figure 3.3. 1: Flow chart indicating the required input data for DOSXYZnrc and its output data.

There are four main sets of parameters in the Input file. The first set of parameters specifies the geometries of the phantom. As mentioned previously, the phantom is a 3D region in which interactions take place. It can be specified as one big region or many small voxels bound together. The position and size of the phantom are described by the Cartesian coordinate system with X, Y and Z axis orientated in the lateral, longitudinal and vertical directions respectively as in the treatment room.

The second set of parameters specifies the type of medium of each voxel and the region for which the calculated dose will be displayed in the output listing file.

The type of radiation source is specified by the third set of parameters. DOSXYZnrc has a large number of sources with various spatial distributions and angles of incidence. A few examples are: point, square, circular and divergent sources, with incident angles 0, 90 and 270 degrees.

The last set of parameters is similar to the Source Geometrical Configuration parameters in BEAMnrc, which describes the charge and energy of the source. The phasespace file generated by BEAMnrc can be selected as a source for dose simulation in DOSXYZnrc. In this special case the energy of the initial particles will be taken as whatever energy the particles carried when they escaped the final component module in the BEAMnrc simulation. The flow chart in figure 3.3.1 shows the connection between BEAMnrc and DOSXYZnrc. An additional line of code is required to specify the location of the phasespace file in DOSXYZnrc input file. The information from the phasespace file is extracted through this path.

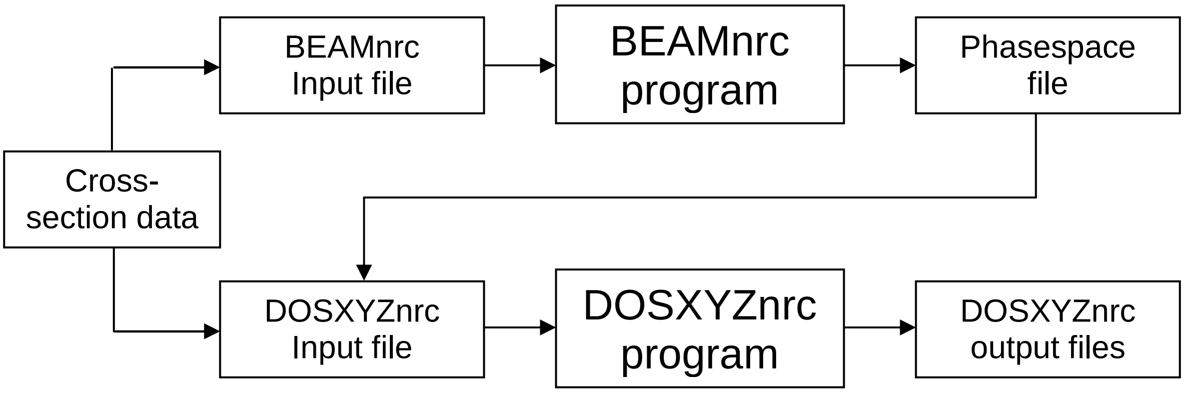

Figure 2.4. 1: Links between BEAMnrc and DOSXYZnrc when phasespace file is used as a radiation source for dose simulation.

The output files of DOSXYZnrc are shown in figure 2.4.1. These files serve the same purpose as the output files produced by BEAMnrc. In general, the Listing and Log files provide a detailed description of the simulation and any uncertainties produced in the simulation. Graphics files are created so that the simulation can be viewed graphically via the EGS_Windows program. The Data file contains the simulated absorbed doses in every voxels in the phantom. The data file is created in a format so that they can be analysed by a program called STATDOSE.

3.4 Monte Carlo Modelling of the Linear Accelerator

Monte Carlo calculation method has been used in radiotherapy for modelling of the X-ray radiation beam and dose distributions for many years. In the early 1980s, when radiotherapy Monte Carlo programs were still in its early stage of development, very simple MC programs that modelled point X-ray sources irradiating a simple homogeneous water phantom were developed to obtain dosimetric data such as the stopping power ratios and X-ray spectra (McCall, McIntyre et al. 1978; Nahum 1978; Andreo and Nahum 1985; Andreo and Brahme 1986; Andreo 1988; Faddegon, Ross et al. 1990; Faddegon, Ross et al. 1991). Manufacturers of the linear accelerators (linacs) also used simple MC programs to assist with the optimisation of their product design (McCall, McIntyre et al. 1978). In 1990, the first model of a simplified linac was used to calculate the dose kernel in water. The dose kernel data were then used in the convolution and superposition algorithms in the commercial treatment planning systems (Mackie, Scrimger et al. 1985; Mohan, Chui et al. 1986).

The rapid increase in computing technology in the mid 1990s triggered a number of published papers describing the complete model of the linac and complex radiation beam shaping devices such as the Multi-Leaf Collimator using Monte Carlo method (Chaney, Cullip et al. 1994; Lovelock, Chui et al. 1995). The first study to clinically implement the Monte Carlo method for dose calculation was performed by Ma et al 1999. The Monte Carlo codes BEAM and EGS4 were used to model the linac head and calculate the dose distributions in his work. Photon beams with energies of 4 MV, 6 MV and 15 MV and electron beam with energies from 6-20 MeV from Varian clinical accelerators 1800, 2100C and 2300CD were modelled. The dose distributions in the homogeneous and heterogeneous phantoms and a patient were calculated and compared with the measured and calculated dose distribution from the commercial treatment planning system FOCUS. The electron beam output factor from the measured data, calculated by the Monte Carlo codes and FOCUS TPS were also compared. The difference between the measured and the Monte Carlo calculated dose distribution were about 2% for various field sizes, source to surface distances and beam modulations. Similar results were observed for electron output factor comparisons. In the comparison between Monte Carlo and FOCUS TPS, a difference of 5% was found. This difference was found for dose calculation in the patient with head and neck, breast and lung tumours. It was concluded that the MC modelling gave better agreement than FOCUS planning system in the heterogeneity region. In addition, Monte Carlo modelling of an electron beam was more accurate and less time consuming compared to the modelling of a photon beam.

Hartmann Siantar et al 2001 also reported the implementation of the Monte Carlo program for radiotherapy dose calculation called PERIGRINE. 6 and 18 MV photon beams from the Varian Clinac 2100C were modelled. The modellings consisted of three separate components; primary, scatter and electron contamination components. The measured and calculated dose distributions in the water phantom were compared for various setups using open field, wedge, block and Multi-Leaf Collimator (MLC). The maximum discrepancy in the comparison was less than 2% in dose and 1.2 mm shift in isodose position for open field and all beam modifiers. The dose calculation for the open field case was compared with EGS4, an older version of EGSnrc. Both of PERIGRINE and EGS4 codes showed similar agreement with the measured data. High discrepancies with the measured data in the build-up region and in the region blocked by the jaws were found for both Monte Carlo codes. It was concluded that both of these codes did not accurately account for the electron contamination component of the photon beam.

The Monte Carlo modelling of the linac head is also useful for investigating the characteristics of the radiation beam. For instance, it is known that the energy and FWHM of the intensity distribution of an electron beam before entering the X-ray target have significant effect on the generated Bremsstrahlung photon beam exiting the X-ray target. This effect was studied in detail by Sheikh-Bagheri and Rogers in 2002. Nine photon linac heads from Varian, Elekta and Siemens with energies between 4-18 MV were simulated using BEAMnrc and DOSXYZnrc Monte Carlo codes. In their investigation, the electron energy and FWHM were tuned by matching the simulated and measured PDDs and in-air off-axis factors. The derivation of the FWHM of the simulated linac heads were said to be completed when the best matches were found for the in-air off-axis factor. The same technique was also used to derive the electron energies except the best match by both the in-air off-axis factor and the PDD was required. The investigation showed that the derived electron beam energies were different between manufacturers for the same nominal energy stated in their specification. The same results were found for the value of the FWHM. The authors also found that the FWHM of the electron beam did not affect the PDD at all. The PDD was only affected by the initial electron beam energy. The off-axis factor on the other hand was strongly affected by the FWHM. The authors also extended their study to investigate how the following parameters affected the off-axis factor and the

PDD: Electron beam divergence, energy distribution, X-ray target lateral dimension, primary collimator upstream opening and the flattening filter material and density. It was found that the beam divergence, X-ray target dimension and energy distribution had insignificant effect on the off-axis factor and PDD. The off-axis factors were very sensitive to the opening of the primary collimator and the flattening filter material and density. Another paper also reported the effect of the electron beam initial energy and FWHM on the PDD and beam profiles (Tzedakis, Damilakis et al. 2004). The same conclusions were made regarding the sensitivity of these two parameters on the PDD and beam profiles.

The MC model of the linac head was used by Ding in 2002 to study the effect of the electron contamination on the surface dose. The results indicated that the maximum contributions from electron contamination at the phantom surface were 21% and 29% for 6 and 18 MV respectively for a 40x40 cm^2 photon beam. Ding also found that the simulated and measured doses were in excellent agreements. However the simulation time was still a limiting factor for the application of MC algorithm in clinical practice.

In this project, the Monte Carlo the linac head was modelled using BEAMnrc code. One of the objectives was to derive two parameters; the initial electron beam energy and its FWHM, which would give the closest agreement between the modelled and the measured dose data. The searching technique used is similar to that reported by Sheikh-Bagheri and Rogers in 2002. The searching technique performed by Sheikh-Bagheri and Roger was time consuming. The problem was addressed in this project by using the time reduction techniques such as the Bremstrahlung Splitting (Kawrakow, Rogers and Walters, 2004), ECUT, PCUT, ESAVE and others (Roger et al, 2005) available in BEAMnrc and DOSXYZnrc code.

3.5 Monte Carlo Modelling of the Transmitted Dose

The Electronic Portal Imaging Device (EPID) have been gaining popularity in dosimetry application in recent years (Essers, Hoogervorst et al. 1995). The applications of the EPID in 2D and 3D in-vivo dosimetry were discussed in section 2.2.4. The calibration process for converting the EPID signal to the absorbed dose in a water phantom was also described in section 2.2.5. In this section, the use of Monte Carlo method in the modelling of the transmitted dose in an EPID will be presented.

It was discussed in section 2.2.4 that the first step in in-vivo dosimetry procedure based on portal imaging device was the acquisition of the transmitted dose map. The transmitted dose map can be obtained by applying the calibration factor to the measured EPID signals. The accuracy of the transmitted dose measurement can be verified by using Monte Carlo modelling of a system consisting of the linac head and an EPID. Monte Carlo method is suitable for verification purpose because it had been set as a gold standard for dose calculation under most circumstances in radiotherapy (Shortt, Ross et al. 1986; Mackie 1990; Rogers and Bielajew 1990). In addition, the dosimetric characteristics of the EPID can also be studied. Keller et al 1998 reported the use of Monte Carlo method to compare the behaviour of the energy deposition kernel in the EPID sensitive layer based on two different types of EPID models. The first type was an EPID which was made from uniform water density material and the second type represented all layers of material in the actual EPID. The differences in the energy deposition kernel for two different types of EPID were used to study their characteristics. The energy deposition kernel was obtained for various energies, lateral positions and depths in the water phantom based EPID. It was shown that the differences in the energy deposition kernel between two types of EPID varied with the energy of the X-ray beam. For the same energy, the variation of the energy deposition kernel depended on the depth and the lateral position relative to the central axis. The maximum variation observed was 2%. It was found that the variation was smallest when the kernel was measured at a depth of 1.2 cm in the water phantom like EPID type. The outcome of this study is useful in the calibration of an EPID for dosimetry purposes. This is because the transmitted dose is the convolution of the photon energy fluence and the energy deposition kernel at the EPID detection layer. The calibration procedure of the EPID response for dosimetry purposes should take into account the variation of the energy deposition kernel with energy, lateral position and depth.

Further work in the MC modelling of an EPID for dosimetry purpose was performed by Spezi and Lewis 2002. The BEAM and DOSXYZ Monte Carlo programs were used to model the complete linear accelerator including the Multi-Leaf Collimator

(MLC) and the EPID. The linear relationship between the measured signal squared and the MC simulated dose was found. This relationship was shown to have a reproducibility of 1%. The dose calibration matrix for the EPID was obtained from the linear fit parameter. The 2D dose in the measured and simulated EPID was compared and agreement of 2% and 2 mm was demonstrated. Using the measured 2D dose distribution, the authors were able to verify the dose distribution calculated from the MC model of the MLC. This investigation is important in the verification of complex multi-field and multi-segments treatment technique for example in Intensity Modulation Radiotherapy where the MLC is the only beam modifying device.

Chin et al 2003 extended the capability of the MC model of the linac and EPID system to allow the transmitted dose map be calculated for phantoms that are obliquely angled to the EPID. The MC codes used in his work were BEAMnrc and DOSXYnrc. In additional, a MATLAB code called TWIZ&GLU was developed to model the phantom and an EPID separately and combine them into one integrated phantom upon import into DOSXYZnrc for dose calculation. The method for creating the phantom and an EPID in this way is not supported by DOSXYZnrc. The calculated EPID signal of an inhomogeneous phantom at an oblique angle was compared with the measured data. An agreement of 2% was found. It was concluded that the method developed in his work could be used for the calculation of the transmitted dose where the phantom is at an oblique angle to the EPID.

An interesting idea proposed by Jarry and Verhaegen 2005 was that an electron beam could generate enough Bremsstrahlung photons to produce good quality EPID images. The MC codes BEAMnrc and DOSXYZnrc from the EGSnrc system were used to model the linac and an EPID to study the EPID image quality during electron beam treatment. The productions of the Bremsstrahlung photon fluences in various components of the linac head and their dependence on the energy, electron applicator and cut-out size were investigated. The EPID image quality of the measured and simulated electron beam was compared and agreement of 5% was found for the image contrast. Both of the simulation and the measurement were performed on the anthropomorphic RANDO phantom. The measured electron image quality was found to be comparable to that of a 6 MV photon beam. Two conclusions were made from this study. A good EPID image from an electron beam might be obtained in the clinical conditions using as little as 10.7 monitor units. Monte Carlo simulated EPID image can be used for comparison with the actual image during electron beam treatment to ensure accuracy in positioning.

In this project, a system consisting of a linac and an EPID, was modelled in a similar way as in the work of Spezi and Lewis, however the MLC was excluded. The transmitted doses were calculated for three different types of phantom setups. The first setup allowed the transmitted dose of a 6 MV X-ray beam from a Varian 600CD linac to be calculated in an open field. This was followed by transmitted dose calculations for 15 cm of solid water phantom and the humanoid RANDO phantom. These setups were designed to allow the investigation of the transmitted dose calculation for simple and more complex scenarios.

3.6 Transmitted Dose Evaluation – The Gamma Algorithm

Modern radiotherapy techniques such as 3D Conformal Radiotherapy and IMRT often produce complex dose distributions such as multiple low and high dose gradient regions. A simple comparison method where two dose maps are superimposed is good for qualitative analysis. The dose difference comparison method for two dose maps is more quantitative. However, in the region of high dose gradient, a small difference in the spatial position of the two dose maps can result in a large difference in the dose value. In order to resolve this problem, Low et al 1998a proposed a method called the Gamma Map algorithm. This method takes into account both the dose difference and the spatial displacement between the corresponding points on two dose maps. The Gamma value or Gamma index is used to assess the agreement between the measured and calculated points. In the comparison between the measured and calculated dose map, the Gamma index, $\gamma(r_m)$ is defined as the minimum of the Gamma function, $\Gamma(r_m, r_c)$ for a measurement point at position r_m and a calculated point at position r_c. Mathematically, they can be described as follow:

$$\gamma(r_m) = \min\{\Gamma(r_m, r_c)\} \forall \{r_c\} \qquad \textbf{Eq 3.6. 1}$$

$$\Gamma(r_m, r_c) = \sqrt{\frac{r^2(r_m, r_c)}{\Delta d^2{}_M} + \frac{\delta^2(r_m, r_c)}{\Delta D^2{}_M}} \qquad \textbf{Eq 3.6. 2}$$

$r(r_m, r_c)$ is the distance between the measured and calculated points at position r_m and r_c respectively and $\delta(r_m, r_c)$ is the dose difference between them. The calculation of the Gamma index requires two user define criteria called the dose difference (ΔD_M) and the distance-to-agreement (Δd_M) acceptance criteria. The value of ΔD_M is the accepted tolerance in the process of acquiring the measured and calculated dose data. The value of Δd_M on the other hand is the accepted tolerance for the misalignment of the corresponding dose maps due to positioning uncertainty in the measurement. The clinically accepted values of ΔD_M and Δd_M are generally 3% and 3 mm respectively.

Based on Low et al algorithm, the investigated dose is said to have failed when the Gamma index is greater than one and passed when the Gamma index is less than or equal to one. Mathematically they can be expressed as follow:

$$\begin{aligned} \gamma(m) \;\; &\leq 1 \qquad \textit{passed} \\ &> 1 \qquad \textit{failed} \end{aligned} \qquad \textbf{Eq 3.6. 3}$$

From equations 3.6.2 and 3.6.3, it can be seen that the smaller the values of ΔD_M and Δd_M, the harder it is to pass the Gamma comparison. Large values of ΔD_M and Δd_M would make it easy to pass the Gamma comparison, but the Gamma analysis may not provide useful results for assessing the agreement between the measured and calculated dose map. In clinical practice, a compromise between time and accuracy should be considered in selecting the values for ΔD_M and Δd_M because longer times may required in order to achieve precise and accurate measured and MC calculated dose maps.

In 2D comparison between the measured and calculated dose distribution, the acceptance criteria for the Gamma analysis can be pictured as the ellipsoid in figure 3.6.1. The size of this ellipsoid is defined by ΔD_M and Δd_M.

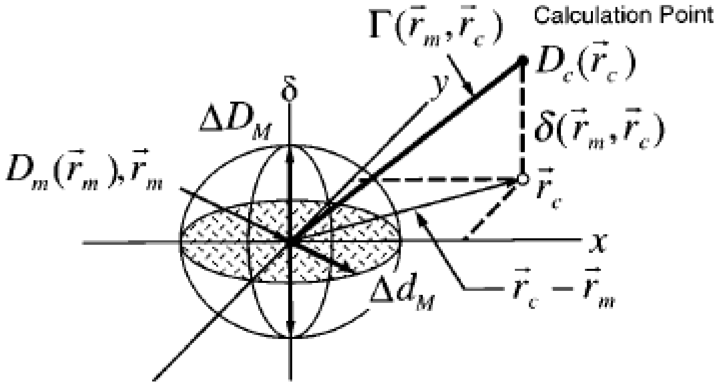

Figure 3.6.1: The Gamma criteria can be represented graphically by an ellipsoid. In this example, the position of a measured point is taken as the origin and the position of a calculated point is represented by vector $\vec{r}(x, y)$ in the x and y plane. The length of the vector $\vec{r}(x, y)$ and δ are the differences in the position and dose respectively between the measured and calculated point (Low, Harms et al. 1998).

The coordinate system in figure 3.6.1 is made up of x, y and δ axes. The combination of x and y axes are represented by the position vector $\vec{r}(x, y)$ which describes the direction and the distance between the calculated point relative to the measured point, which is the origin in this coordinate system. This distance is defined as follows:

$$r(x, y) = \sqrt{x^2 + y^2} \qquad \textbf{Eq 3.6. 4}$$

The δ axis describes the measured and calculated dose difference. The passed and failed values correspond to the calculated points that are inside and outside the ellipsoid respectively. In the comparison where only 1D dose distributions such as the PDD and beam profiles are required, the Gamma acceptance criteria are simply represented by an oval which is illustrated in figure 3.6.2. The spatial position between the measured and calculated points can be described simply by the x axis. The δ axis is defined in the same way as in 2D comparison. The passed and failed values correspond to the calculated points that are inside and outside the oval respectively.

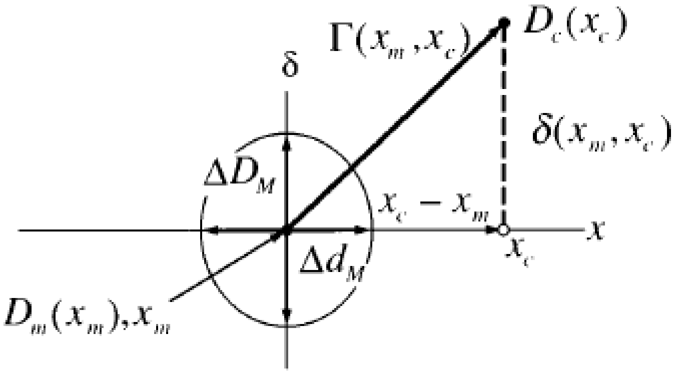

Figure 3.6.2: An oval shape represents the Gamma criteria for 1D dose analysis. This is useful for comparing PDD curves and beam profiles where steep dose gradients are present (Low, Harms et al. 1998)

The OmniPro I'mRT analysis software (Scanditronix Wellhofer, OmniPro I'mRT v1.4b, 2005) was used for the comparison of the measured and calculated 2D dose distribution in this project. The Gamma algorithm implemented in OmniPro I'mRT software was based on the algorithm of Low et al 1998a described above.

Further developments of the Gamma algorithm have been reported in the literature. In 2002 Depuydt et al et al introduced a refined Gamma algorithm that provided a faster solution for comparing complex dose distributions (Depuydt, Van Esch et al. 2002). The key difference in Depuydt et al's algorithm is that the Gamma indices are either 0 or 1 for failed or passed respectively in the comparison. The quality of the comparison is determined by how small are a user defined ΔD and Δd acceptance criteria. The advantage of this algorithm is that it provides a simple result which is useful for making a quick decision on whether the two data sets (measured and calculated dose map) agree within an acceptable tolerance. However, Depuydt et al algorithm provides no indication about how good the agreements between the measured and calculated points in the comparison are. Bakai et al 2003 also reported another development of the Gamma algorithm (Bakai, Alber et al. 2003). The concept of the Gamma algorithm used by Bakai et al is an extension to that of Low et al 1998a. It allows the Gamma analysis to be performed for 3D dose distribution. The algorithm also allows the distance to agreement criterion to be set for three spatial directions to account for positioning errors that are not uniform in the anterior/posterior, lateral and superior/inferior directions. The flexibility of setting the distance to agreement criterion for all three spatial directions in this method was claimed to improve the Gamma calculation time in comparison to the method of Low et al. Bakai et al method was tested on a particular IMRT head and neck patient. Dose calculation was performed by the HYPERION treatment planning system which utilised the Fast Monte Carlo code XVMC (Alber 2000; Fippel, Haryanto et al. 2003) and film was used for acquiring the measured dose.

CHAPTER 4

MONTE CARLO MODELLING AND VERIFICATION OF THE VARIAN 600C/D LINEAR ACCELERATOR HEAD

In Monte Carlo modelling of the linear accelerator head, it is essential that the characteristics of the linear accelerator head are known precisely. The parameters that characterise the linac head can be classified into two categories: physical and geometrical. The geometrical parameters include the dimension, shape, and position of the components of the linac head relative to the radiation source as well as the Full Width at Half Maximum (FWHM) of the spatial distribution of an electron beam prior to its interaction with the X-ray target. The physical parameters include the mass, density, atomic number and composition of the components as well as the energy of an electron beam prior to its interaction with the X-ray target. These parameters are available from the manufacturers only in the form of a generic machine specification (Varian Oncology Systems, Monte Carlo Project 1996). Varian linac head generic specification was used as a guide for the modelling of the linac head in this work. This chapter describes the Monte Carlo modelling of each component in the linac head using BEAMnrc program. The Monte Carlo dose calculation program called DOSXYZnrc was used to calculate the beam profiles. The analysis of the beam profiles was performed to verify the accuracy of the modelled linac head components. The verification process will also be described in this chapter.

4.1 Modelling of the Linear Accelerator Head using BEAMnrc

The production of an X-ray beam from the 6 MV Varian 600C/D photon linear accelerator head was simulated by transporting a monoenergetic electron beam through a sequence of component modules. Table 5.1.1 describes the use of the component modules in the simulated linac head.

Component Modules in the simulated linac head	Composition and Physical Density	The use of the component module in the simulation
1) SLABS	Tungsten – 19.3 g/cm^3 Copper – 17.5 g/cm^3	A model of the X-ray target.
2) FLATFILT	Lead – 11.34 g/cm^3	A model of 2 components: The primary collimator and the flattening filter. The flattening filter is surrounded by the primary collimator.
3) CHAMBER	Outer and inner plates made of Steel (8.06 g/cm^3) and Copper (17.5 g/cm^3) respectively Upper and lower cavity made of Mica (2.9 g/cm^3)	A model of the monitor ion chamber .
4) MIRROR	Mylar – 1.38 g/cm^3	A model of the light field mirror.
5) JAWS	Tungsten – 19.3 g/cm^3	A model of the secondary collimators that define the beam field size.
6) SLABS	Air – 1.2048 x 10^{-3} g/cm^3	A model of an additional air region extends 55.5 cm in the beam direction so that the phase space is 100 cm from the source.

Table 4.1.1: Description of the Component Modules which were used in modelling of the linac head in BEAMnrc code.

The 3D and 2D display of the component modules are shown in figure 4.1.1. a) and b) respectively The values of the parameters describing the geometry and composition of the component modules were obtained from Varian's machine specification data (Varian Oncology Systems, Monte Carlo Project 1996). The complete description of the ion chamber and X-ray target was not given in the specification data. Assumptions for the number of layers in the ion chamber and the individual thickness of the two layers that made up the X-ray target were made based on observation of the actual components. In addition, the cone shape of the flattening filter was approximated by 13 cylinders stacking on top of each other in the order of increasing radius.

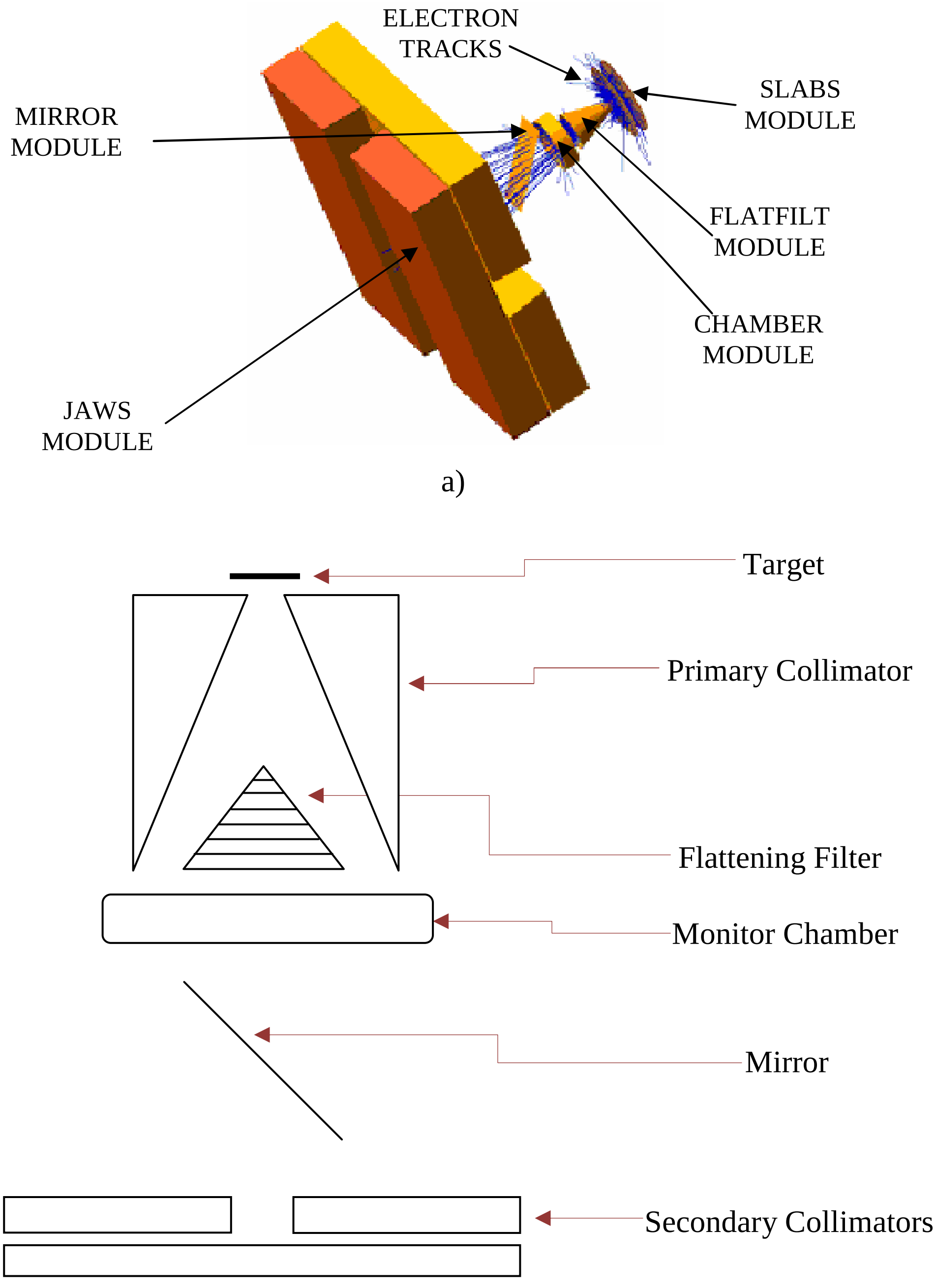

a)

b)

Figure 4.1.1: a) 3D display of the Varian 600C/D 6 MV linear accelerator head simulated by BEAMnrc code. b) unscaled 2D representation of the modelled linac head

The electron beam was modelled using source number 19 from BEAMnrc program (Rogers, B. et al. 2007). Source 19 describes an electron beam entering the centre of the X-ray target at 90 degrees. The spatial distribution of the electron beam is defined by the Gaussian distribution similar to the one in Figure 4.1.2.

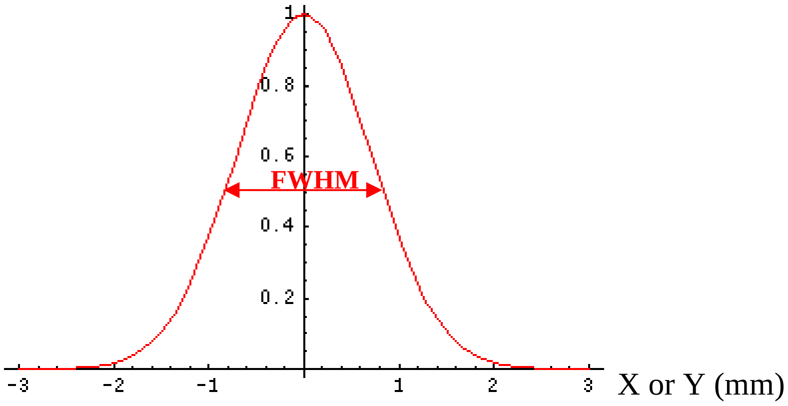

Figure 4.1. 2: The Gaussian distribution which describe the spatial spread of the electron beam before hitting the X-ray target (Weisstein 2008).

The machine specification data does not provide information about the FWHM of the electron beam. In addition, the energy of the electron beam was specified with an associated uncertainty (Varian Oncology Systems, Monte Carlo Project 1996). Therefore it is important that the combination of the FWHM and the energy of the electron beam is selected appropriately and all of the characteristics of the modelled beam are verified. The following section describes the calculation of the percentage depth doses and the beam profiles and how they were used to verify the characteristics of the linac head.

4.2 Calculation of Dose Distributions using DOSXYZnrc

The accuracy of the modelled beam was assessed using the measured Percentage Depth Doses and the beam profiles for various field sizes and depths in a homogeneous water phantom. These data were calculated by the DOSXYZnrc program. The parameters required for the calculation were entered in the input file (Appendix A.2) which was invoked by the program during the execution process. For the assessment of the accuracy of the beam model, the simulation setup in figure 5.2.1 had been designed.

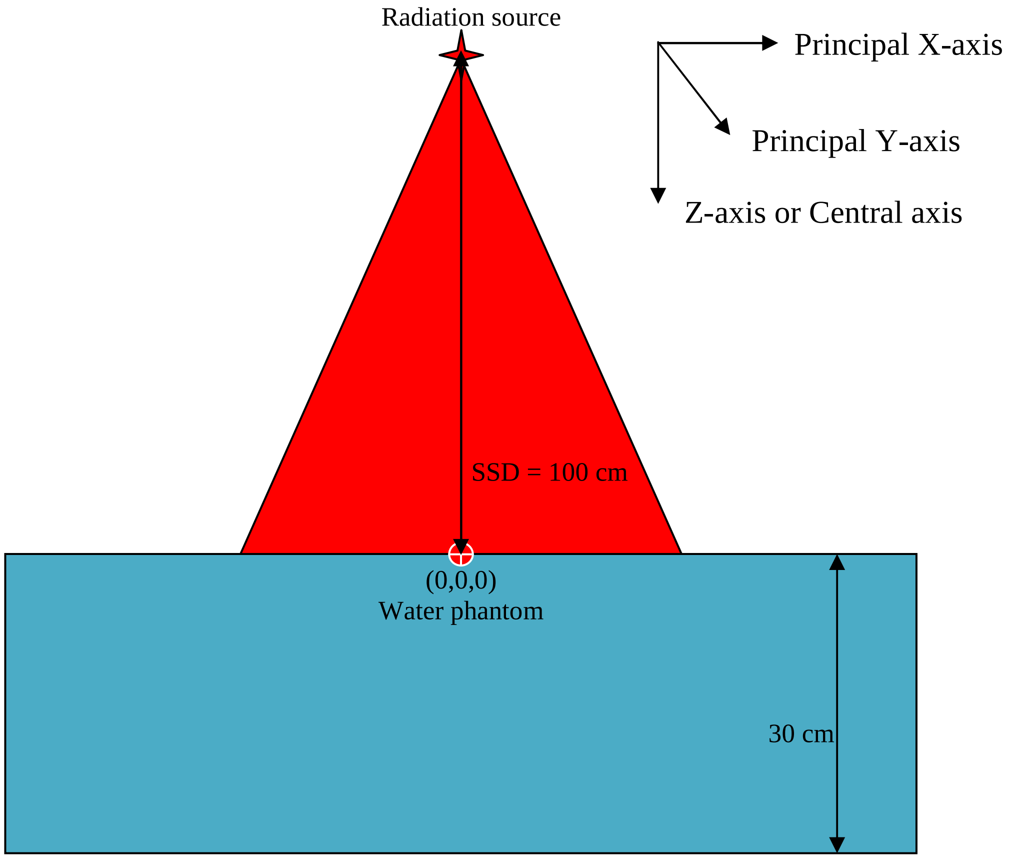

Figure 4.2. 1: 10x10 cm^2 X-ray beam incident on a water phantom at a distance of 100 cm from the X-ray target.

The coordinate system in DOSXYZnrc is such that the X-axis is in the lateral direction of the couch in the treatment room, Y-axis is in the direction along the couch and the Z-axis is in the direction of the beam usually called the central axis. The origin is on the surface and at the centre of the phantom. The phase space file generated from the simulation of the linac head was used as an X-ray beam in the dose simulation. The position of the phase space file was set so that the distance from the electron beam to the surface of the phantom (SSD) is 100 cm and the photon beam is incident on the phantom from above. The 10x10 cm^2 and 40x40 cm^2 field sizes were chosen for the analysis of the PDDs and the beam profiles respectively. Backscattered X-rays from beyond the region of interest can contribute to the dose. In order to include the contribution of backscatter, the phantoms were made 10 cm larger than the region of interest in the Z direction. The phantom and voxel sizes are shown in table 4.2.1. The voxel dimensions were chosen such that minimal simulation time was required for each simulation without compromising the resolution of the data.

Field Size (cm^2)	**40x40**	**10x10**
Phantom Size (cm^3)	100x100x30	50x50x30
Voxel Size (cm^3)	1x1x0.4	0.5x0.5x0.4

Table 4.2.1: The voxel dimensions correspond to the radiation field sizes and phantom dimensions. They determine the resolution of the dose data.

4.3 Selection of Variance Reduction Parameters

The variance reduction parameters used in the simulation are Direct Bremsstrahlung Splitting (DBS), ECUTIN, PCUTIN, ESAVE_GLOBAL and IREJCT_GLOBAL (see section 3.2). Direct Bremsstrahlung Splitting is very useful when there is a need for a large number of particles N (N~10^8) in the phase space. The efficiency for the simulation of the transmitted dose in an EPID increases up to a factor of 120 compared to no DBS as shown in table 4.3.1. This table also shows the efficiency in term of calculation time T and uncertainty σ for the simulation of dose distribution in a water phantom. An increase by a factor of about 7 was observed. Bremsstrahlung Spliting number (NBRSPL) in **BEAMnrc** of 1000 was used in all simulations. This number was reported in the literature to give the highest efficiency (Kawrakow, Rogers et al. 2004). The paper also shows that the efficiency varies slowly for NBRSPL greater than 1000. The result from table 4.3.1 shows that the efficiency decreases by a factor of 1.01 when NBRSPL of 5000 was used. N_SPLIT is the Bremsstrahlung Splitting number in **DOSXYZnrc** program. The efficiencies for three values of N_SPLIT were calculated in this work and are shown in figure 4.3.1. N_SPLIT equal 30 is used for all of the dose simulations in this project because it gives the highest efficiency. This is consistent with the recommended N_SPLIT value of 32 in DOSXYZnrc users manual (Walters, Kawrakow et al. 2007).

Simulation of the dose distribution in a water phantom (40x40 cm^2 field)								
BEAMnrc Simulation				**DOSXYZnrc** Simulation			Total Time T (hrs)	Efficiency 1/TS^2
NCASEB	NBRSPL	Time (hrs)	N	NCASED	Errors σ (%)	Time (hrs)		
10^9	0	48.0	5.7x10^6	10^9	1.2	28	76.0	1.0x10^{-2}
4x10^6	1000	5.0	1.1x10^6	10^8	1.2	8	13.0	7.5x10^{-2}
10^6	5000	6.9	1.4x10^8	10^8	1.2	8	14.9	7.1x10^{-2}
Simulation of the transmitted dose in an EPID (10x10 cm^2 field)								
10^9	0	46.5	4.1x10^5	3.6x10^6	32	3	49.5	1.97x10^{-5}
10^8	1000	123.5	1.1x10^8	3.6x10^8	1.1	226	345.5	2.4x10^{-3}

Table 4.3.1: Efficiency of the Direct Bremsstrahlung Splitting method in dose and beam simulation relative to simulation without using Direct Bremsstrahlung Splitting.

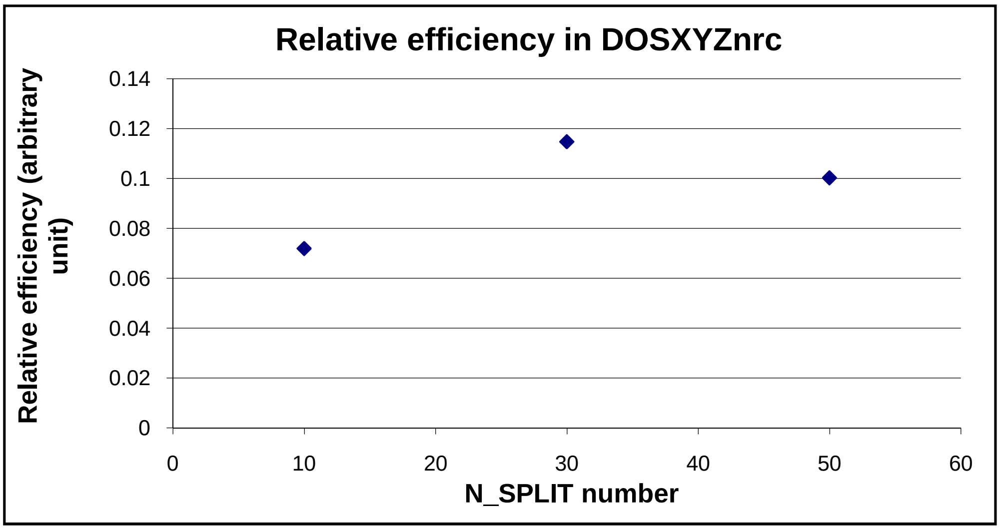

Figure 4.3.1: Comparison of the relative efficiency of DOSXYZnrc for three N_SPLIT number.

The value of N is linearly proportional to the original number of particles in the simulation (NCASEB). A large value of N is required so that the particles in the phase space do not get re-used in the dose simulation. The uncertainty in the simulation is related to the original number of particles in the dose simulation (NCASED) as follows:

$$\sigma = \frac{1}{\sqrt{NCASED}} = \frac{1}{\sqrt{T}} \qquad \textbf{Eq 4.3. 1}$$

The relationship between the calculation time and the uncertainty in the simulation is shown in figure 4.3.2. The blue curve is the power series interpolation of the data points (red diamond). The interpolation function is also presented in figure 4.3.2 with R^2 value nearly equal to 1. The shape of the relationship between the simulation time and uncertainty is a result of random statistical processes that the Monte Carlo program simulates. As mentioned in section 3.1 the random number generator used in DOSXYZnrc is Ranlux which has a probability function that follows the Poisson distribution function (Metcalfe and Kron 1997). The uncertainty is calculated as the standard deviation of the outcome over a group of samples. However, to improve the uncertainty in the dose simulation, not only the value of NCASED needs to be increased but N must also be increased accordingly otherwise the phase space particles will get re-used or recycled. It was found that the uncertainty in the photon dose calculation unchanged for recycling the particles three times. The uncertainty improved by 40% when recycled the particles by 27 times and a certain fixed value was reached regardless of how many times the particles were recycled (Walters, Kawrakow et al. 2002). The efficiency of other variance reduction parameters has been discussed in the literature (Rogers, Faddegon et al. 1995).

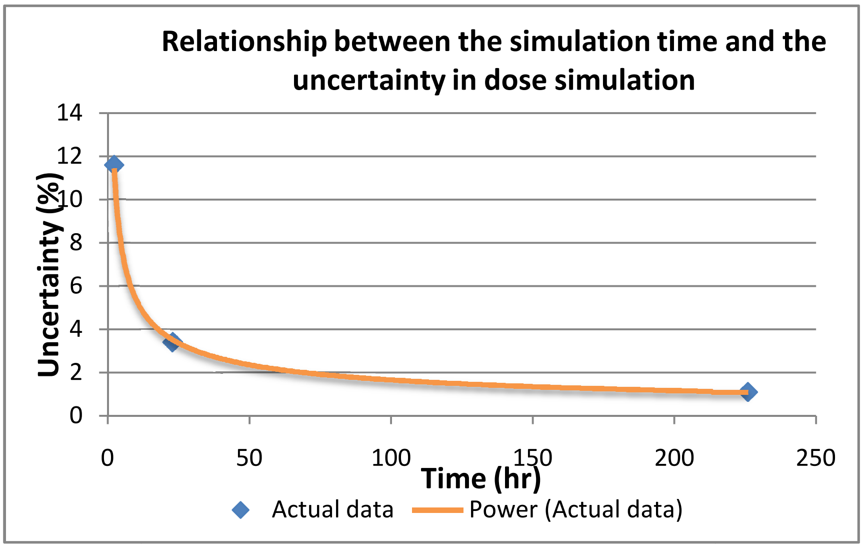

Figure 4.3. 2: Simulation Time versus Uncertainty for dose simulation in the EPID. The blue curve shows the power interpolation of the actual data.

Parallel processing is another feature in EGSnrc which can be used to reduce the simulation time. In the current work, the South Australian Partnership for Advanced Computing (SAPAC) computing system was used for the MC simulation. SAPAC is a government owned organisation. One the objective of SAPAC is to provide services and supports to students and researchers whose project work requires unpractically long computing time on a personal computer. SAPAC has four mainframe systems: Aquila, Hydra, Orion and Perseus. Hydra is the fastest system which has 128 parallel processors. The maximum of 10 parallel processors was allocated for the current project work. Each processor in Hydra has a CPU speed of 2.4 GHz and that runs under REDHAT Linux 7. An investigation was conducted to check the computing time for parallel and sequential computing mode. Table 5.3.2 shows that a single processor takes about 225 hours to complete a particular simulation. The same simulation takes about 22.6 hours to complete on 10 parallel processors. The number of particles in the dose simulation (NCASED) was split evenly and the uncertainty was calculated for the corresponding parallel simulation. Parallel processing method in BEAMnrc and DOSXYZnrc is nearly 100% efficient that is if 10 processes are running at the same time then the total simulation time reduces by a factor of 10 while maintaining the same accuracy as sequential simulation.

Type of Job	NCASED	S (%)	T (hr)
Sequential	$3.6\text{x}10^8$	1.1	~225
Parallel 1	$3.6\text{x}10^7$	3.6	22.5
Parallel 2	$3.6\text{x}10^7$	3.5	22.5
Parallel 3	$3.6\text{x}10^7$	3.5	22.5
Parallel 4	$3.6\text{x}10^7$	3.6	22.7
Parallel 5	$3.6\text{x}10^7$	3.5	22.7
Parallel 6	$3.6\text{x}10^7$	3.5	22.6
Parallel 7	$3.6\text{x}10^7$	3.6	22.8
Parallel 8	$3.6\text{x}10^7$	3.6	22.6
Parallel 9	$3.6\text{x}10^7$	3.6	22.6
Parallel 10	$3.6\text{x}10^7$	3.5	22.7
Total for parallel jobs	$3.6\text{x}10^8$	1.1	226.2~22.6/processor

Table 4.3. 2: Time required for parallel and sequential simulation for the transmitted dose in the EPID. S represents the uncertainty in a single voxel calculated by DOSXYZnrc.

4.4 Verification of the Linear Accelerator Head Model

The geometrical characteristics of the simulated linear accelerator head were verified by comparing the simulated and measured percentage depth dose curves and the beam profiles. The beam field sizes were defined based on the position of the secondary collimators. They can be verified by measuring the distance between two points where the dose in the profile drops to 50% relative to the central axis dose. The MC calculated beam profiles at the depth of D_{max} for two different field sizes of 40x40 cm^2 and 10x10 cm^2 are shown in figure 4.4.1. The black solid line in figure 4.4.1 a) shows a distance of 10 cm across the 50% level. This confirms that the jaw positions were accurately modelled for the 10x10 cm^2 radiation field size. The black solid line in figure 4.4.1 b) measures slightly larger than the expected value of 40 cm. The reason for this is because the beam profiles were simulated at depth of 1.4 cm and so the projection of the simulated radiation field is at 101.4 cm instead of at the surface. Geometrical calculation shows that the same result should be observed for the 10x10 profile as well however, the difference between the set field size and the observed field size is much less than that of the 40x40 profile (less than 1 mm) on each side of the profile and thus cannot be resolved on the graph.

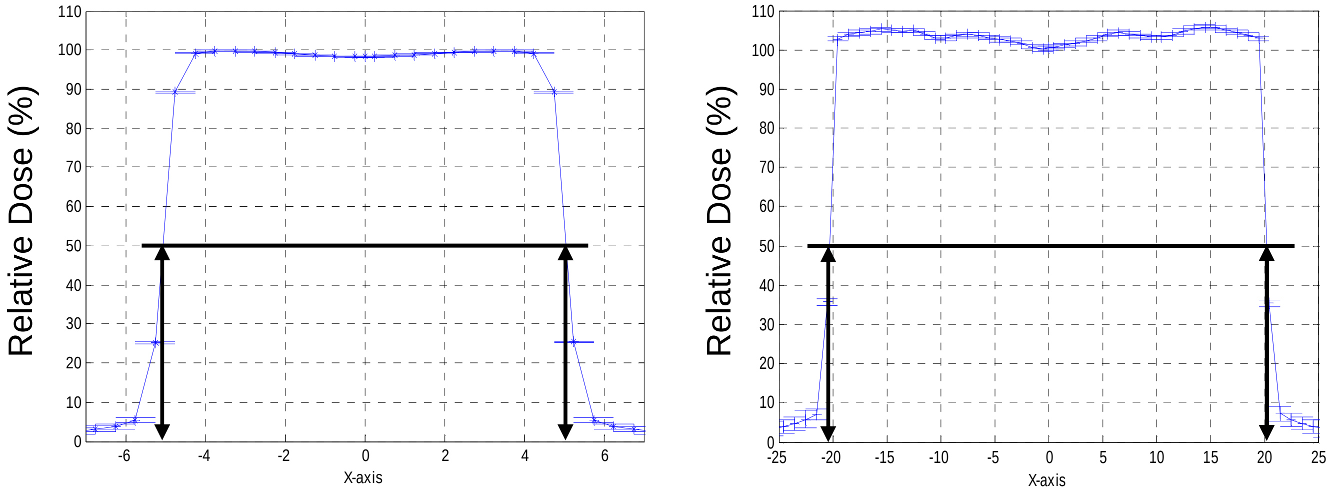

a) b)

Figure 4.4. 1: Verification of the beam field size using the calculated beam profiles a) 10x10 cm ^{2} b) 40x40 cm^{2}.

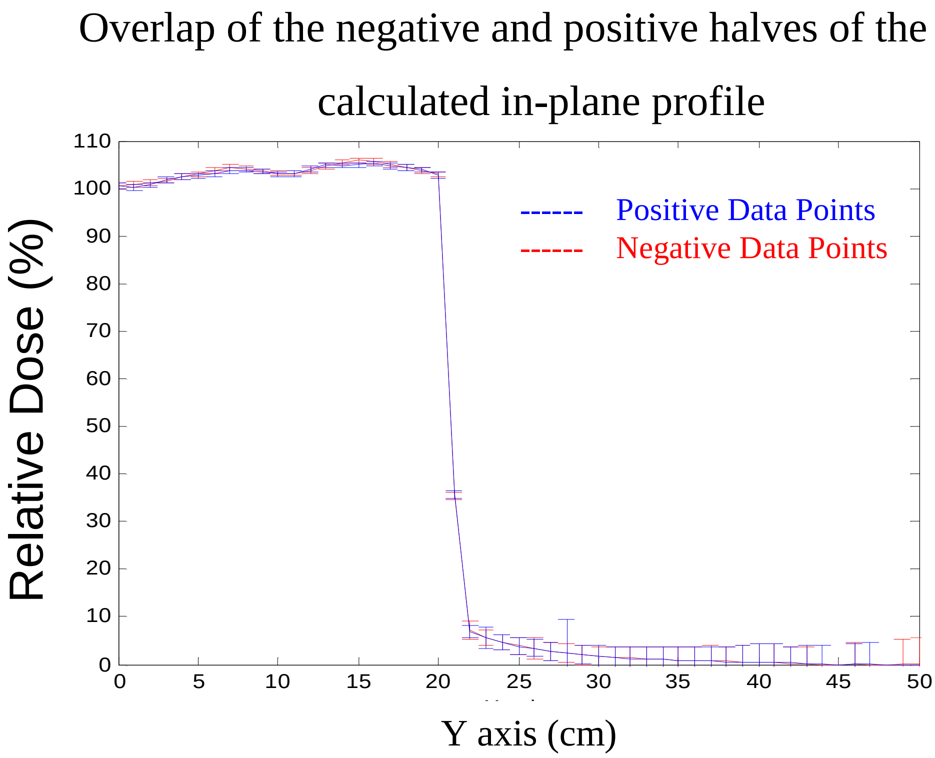

Figure 4.4.2: The negative and positive data points of the 40x40 cm^{2} simulated in-plane beam profile were overlapped to verify the axial symmetry of the simulated linac head.

The structure of the linac head was designed so that the distribution of the radiation was radially symmetric about the central axis. This symmetry was verified to ensure that the modelling parameters were accurately entered in the input. The beam profile in the in-plane direction was bisected at the centre and the negative and positive data points were overlapped as shown in figure 4.4.2. The maximum difference between the negative and positive data points is 1% which is smaller than the uncertainty of the simulation. This result confirms that the simulated linac head is symmetrical about the central axis in a single plane.

The radial symmetry property of the radiation beam also implies that the doses in the in-plane and cross-plane are the same within the uncertainty of the simulation (figure 4.4.3). In reality, this symmetry property is slightly distorted by the design of the secondary collimators. The top jaws of the secondary collimator are opening in the Y direction (in-plane). The bottom jaws are positioned 0.9 cm from below the top jaws and open in the X direction (cross-plane). The doses contributed by radiation scattered from the jaws will be smaller in the in-plane because the scattered radiation from the top jaws will be partially absorbed by the bottom jaws. However, the distortion of the symmetry cannot easily be detected because scatterings from the jaws are random events, which mean the differences between the in-plane and cross-plane profiles are no different than the random uncertainty of the simulation. Unless the uncertainty of the simulation is smaller than the difference in the in-plane and cross-plane, the distortion of symmetry cause by the design of the secondary collimator cannot be seen.

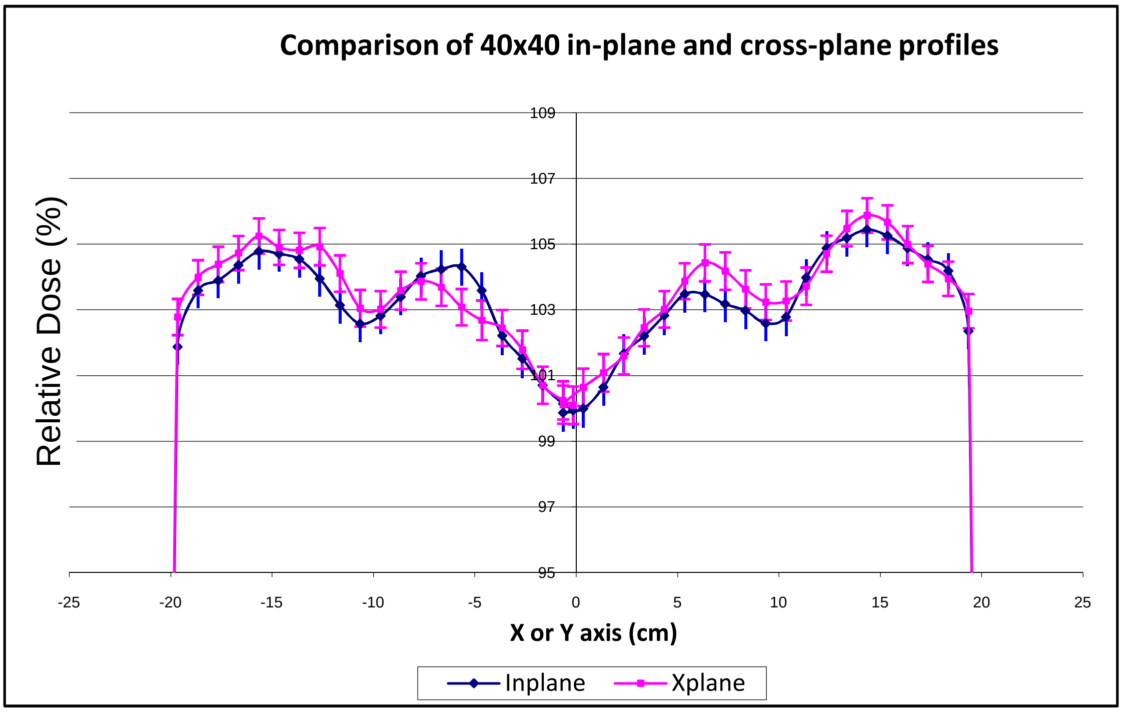

Figure 4.4.3: Overlap of the beam profiles in the in-plane and cross-plane for a 40x40 cm^2 field size at the depth of 1.4 cm from the surface of the phantom.

The measured beam profiles in figure 4.4.4 illustrate the horns on both sides and a dip at the centre. The appearance of these features is the result of the Bremsstrahlung radiation spectrum generated in by the X-ray target. The photons in the centre of the spectrum (centre of the radiation beam) have higher energies than those away from the central axis. Higher energy photon will generate higher energy electrons which deposit dose at larger depths compared to lower energy electrons. Therefore the centre of the phantom receives less dose at a shallow depth below the surface than points off the central axis as the low energy electrons have come to a stop. This is a known fact that the beam harder, more penetrative close to the central axis. Additional beam hardening is caused by the fact that the flattening filter is much thicker at the centre of the radiation beam than at the edges. When the X-ray beam interacts with the flattening filter the lower energy X-rays are attenuated more at the centre than at the edges. The result of this is that more high energy X-rays in the beam spectrum are at the central axis and the total number of X-ray photon is reduced, to produce uniform fluence across the beam area.

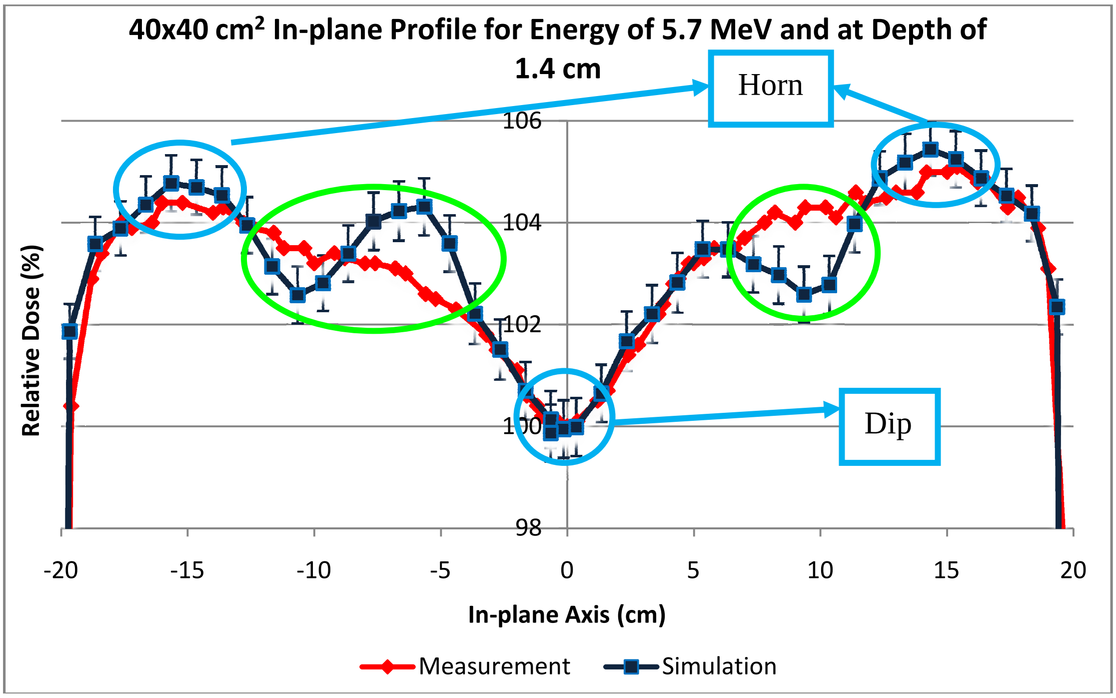

Figure 4.4. 4: **Simulated 40x40 cm^2 beam profile in the in-plane showing the horns at the edges and a dip at the centre.**

The general shape and size of the modelled flattening filter were verified through comparison of the dip and horns of the simulated and measured beam profiles. The shape of the simulated beam profile of figure 4.4.4 conforms very well with the measured profile. Agreement of ≤1.5% can be seen in figure 4.4.4. The differences shown in the blue circles are most likely due to a random error of the simulation. In contrast, the discrepancies highlighted by the green circles were observed in other simulated beam profiles for different electron beam width (FWHM) and electron energy and they occur on both sides of the beam profiles therefore they represent a systematic error of the simulation. The model of the flattening filter and other components in the linac head were carefully checked. The source of error remains unknown. Similar results from other models of the linac head were observed in the literature (Sheikh-Bagheri and Rogers 2002) and the explanation was not found.

CHAPTER 5

MODELLING OF AN X-RAY BEAM FOR A 600C/D LINEAR ACCELERATOR

The Monte Carlo modelling of the linac head component was described in chapter 4. It was mentioned that the actual linac head characteristics were obtained from the generic machine specification (Varian Oncology Systems, Monte Carlo Project 1996). In order to accurately model the X-ray beam coming from the linac head, it is essential that the electron beam energy and beam width (FWHM) value prior to its interaction with the X-ray target are known. These values are not included in the generic machine specification. Monte Carlo simulation programs BEAMnrc and DOSXYZnrc were used to determine the electron beam energy and beam width value in this work. This chapter describes the process of selecting the electron beam energy and electron beam width (FWHM). The objective of this part of the project was to select an electron beam energy and beam width (FWHM) combination such that the simulated and measured dose distributions in a water phantom are within 2% and 3 mm for dose and distance to agreement respectively.

5.1 Selection Process for the Electron Beam Energy and Beam Width at FWHM

The strategy for selecting the best combination of electron beam energy and electron beam width (FWHM) was as follows. The field size of 10x10 cm^2 was used in the analysis of the X-ray PDD. On the other hand the maximum X-ray beam field size of 40x40 cm^2 was chosen in the analysis of the X-ray beam profiles at depth of maximum dose. The reason was because the horns and the dips in the beam profiles would be more pronounced for a large field compared to field size of 10x10 cm^2. The analysis of the PDD was first carried out to check the energy of the electron beam. A series of simulations of the linac head were performed using a range of electron energy values shown in table 5.1 while all other parameters of the model were fixed. The electron energy (E_{best}) that gives the best match between the measured and simulated 10x10 cm^2 X-ray PDD was selected. This linac model was called LINAC$_E$. The analysis of the 40x40 cm^2 X-ray beam profiles in the in-plane and cross-plane was then performed to select the electron beam width. In this analysis, all other parameters in the simulation were fixed except for the FWHM. A range of FWHM values in table 5.1 was used. Similar to the analysis of the electron beam energy, the electron beam width at FWHM (W_{best}) that gives the best match between the measured and X-ray beam profiles was selected. This linac model was called $LINAC_W$. The process so far only provided the best electron energy based on the agreement of the X-ray PDD from linac model $LINAC_E$ and the best FWHM value based on the agreement of X-ray beam profiles from linac model $LINAC_W$ separately. It cannot be assumed that the combination of E_{best} and W_{best} values, applied to another MC linac model, called $LINAC_{EW}$, would still give the best agreement between the simulated and measured X-ray PDD and beam profiles. The assumption can only be made if the electron beam width does not affect the X-ray PDD. A number of papers in the literature have shown that the effect of the electron beam width on the X-ray PDD was insignificant (Sheikh-Bagheri and Rogers 2002). However, this was not taken for granted in this work. For verification purposes, the X-ray 10x10 cm^2 PDD produced from the linac model $LINAC_W$ was also analysed. The electron beam energy and beam width FWHM values E_{best} and W_{best} respectively would be selected for the linac head model if there was no significant change in the PDD; otherwise the selection process for the best electron beam energy would continue for a range of electron beam energies and a fixed electron beam width W_{best}. Finally, the chosen values for the electron beam energy and beam width (FWHM) in the above analysis were used to verify the simulated beam profiles for 40x40 cm^2 radiation field sizes at depths of 10 cm and for 10x10 cm^2 radiation field sizes at depths of 10 cm and 20 cm in a water phantom.

Field Sizes (cm^2)	Energy (MeV)	FWHM (mm)
10 and 40	5.5	1.2
10 and 40	5.6	1.2
10 and 40	5.7	1.2
10 and 40	5.8	1.2
40	5.9	1.2
10 and 40	6.0	1.2
40	5.7	0.9
40	5.7	1.0
40	5.7	1.1
10 and 40	5.7	1.2
40	5.7	1.3
40	5.7	1.4
40	5.7	1.5
40	5.7	1.6
40	5.7	1.7
40	5.5	1.3
40	5.6	1.3
40	5.8	1.3
40	5.9	1.3
40	5.9	1.5
40	6.0	1.3
40	6.1	1.3
40	6.2	1.3

Table 5.1.1: Values of electron beam energy and beam width (FWHM) used in the selection process in order to determine the best values for the MC model of the Varian 600C/D linac had.

5.2 Results and Discussions

The 10x10 cm^2 field size X-ray PDD from the linac head with the electron beam energy of 6 MeV and beam width (FWHM) of 1.2 mm was simulated firsts and resultant X-ray beam data were compared with the measured data. Figure 5.2.1 shows the overlap of the simulated (green) and measured (red) data for this combination of electron beam energy and beam width (FWHM). The simulated data were smoothed from the point just beyond the depth of maximum dose (D_{max}) using the running mean method. The smoothing was performed over 3 data points. Normalisation was then applied to the smoothed simulated data at D_{max} to be consistent with the measured data.

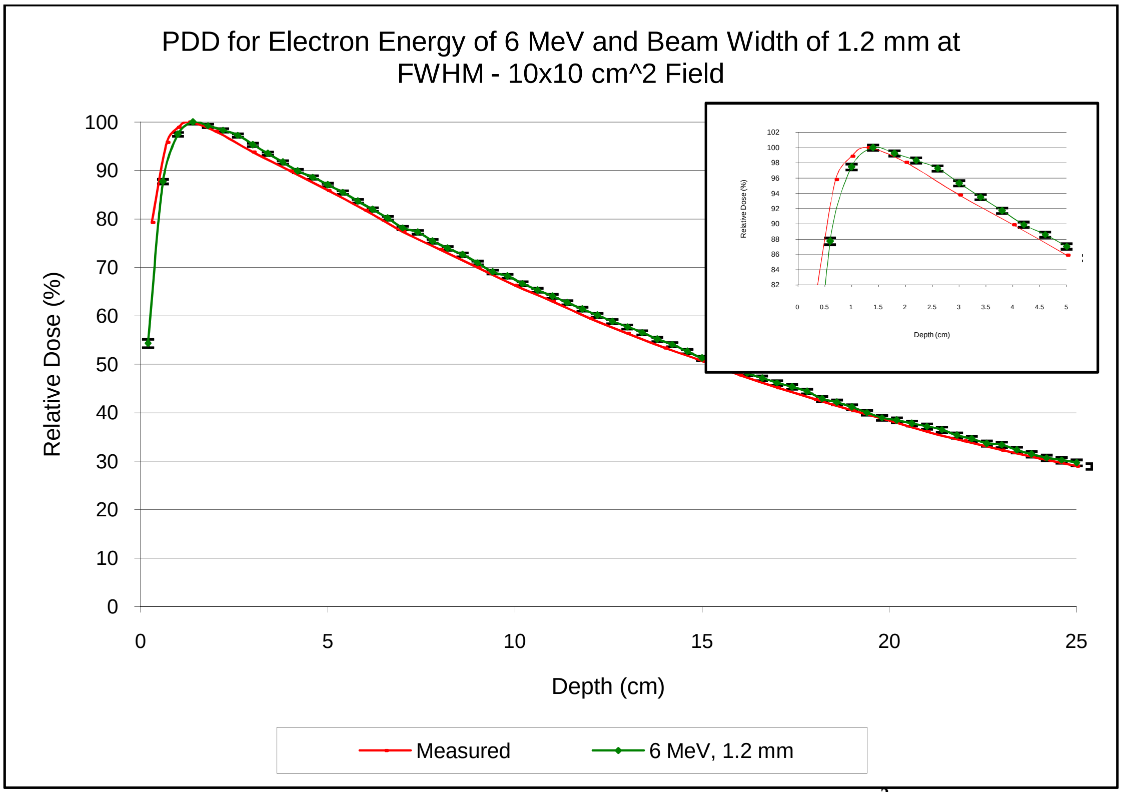

Figure 5.2.1: The measured and simulated PDD produced for a 10x10 cm^2 field by the X-ray beam with an electron beam energy and beam width (FWHM) of 6MeV and 1.2 mm respectively.

The similarity in the shape of the simulated and measured PDD implies that the energy of 6 MeV is close to the actual energy of the modelled linac. Comparison shows agreements of less than or equal to 2% between the measured and simulated data for depths beyond D_{max}. The uncertainties shown in the dose calculation are ±0.7%. The magnitude of these uncertainties depends on the number of particles being simulated in each simulation. The measured data has dose errors of ±0.5% due to the combination of measurement setup uncertainties and the statistical error in the reading.

The insert of figure 5.2.1 shows a difference in the relative dose of upto 6% in the build-up region. There are a number of reasons for this difference. First of all, the dose gradient in the build-up region is very steep. An error in the Z axis of 0.1 cm can cause a change of 3% in dose. The error in the Z axis called distance error is the uncertainty associated with the size of the voxel in the Z direction. They are not shown in the figure but can easily be estimated as follows: The dose at each point is the average dose over the volume of each voxel. In the simulation, the voxel has a dimension of 0.4 cm in the Z direction therefore the distance error is ±0.2 cm. The cylindrical ion chamber IC-15 was used in the measurement of the PDD. The effective point of measurement had been accounted for at the time of measurement therefore there is no distance error associated with the measured data.

The above analysis shows that the simulated PDD is larger than the measured PDD for most data points on the PDD curve. This implies that the selected electron beam energy (6 MeV) should be reduced. This finding had led to simulating of three linacs models that differed from one to another only by the electron beam energy. The three new linac models had electron beam energies of 5.6, 5.7 and 5.8 MeV. Figure 5.2.2 shows the simulated 5.6, 5.7 and 5.8 MeV and the measured PDD curves. There is no change in the general shape of the simulated PDD curves for this range of energy compared to a 6 MeV electron beam. However, the agreement in the build-up region is better for these energies. The insert b) of figure 5.2.2 shows a maximum discrepancy of 3% compared to 6% from figure 5.2.1.

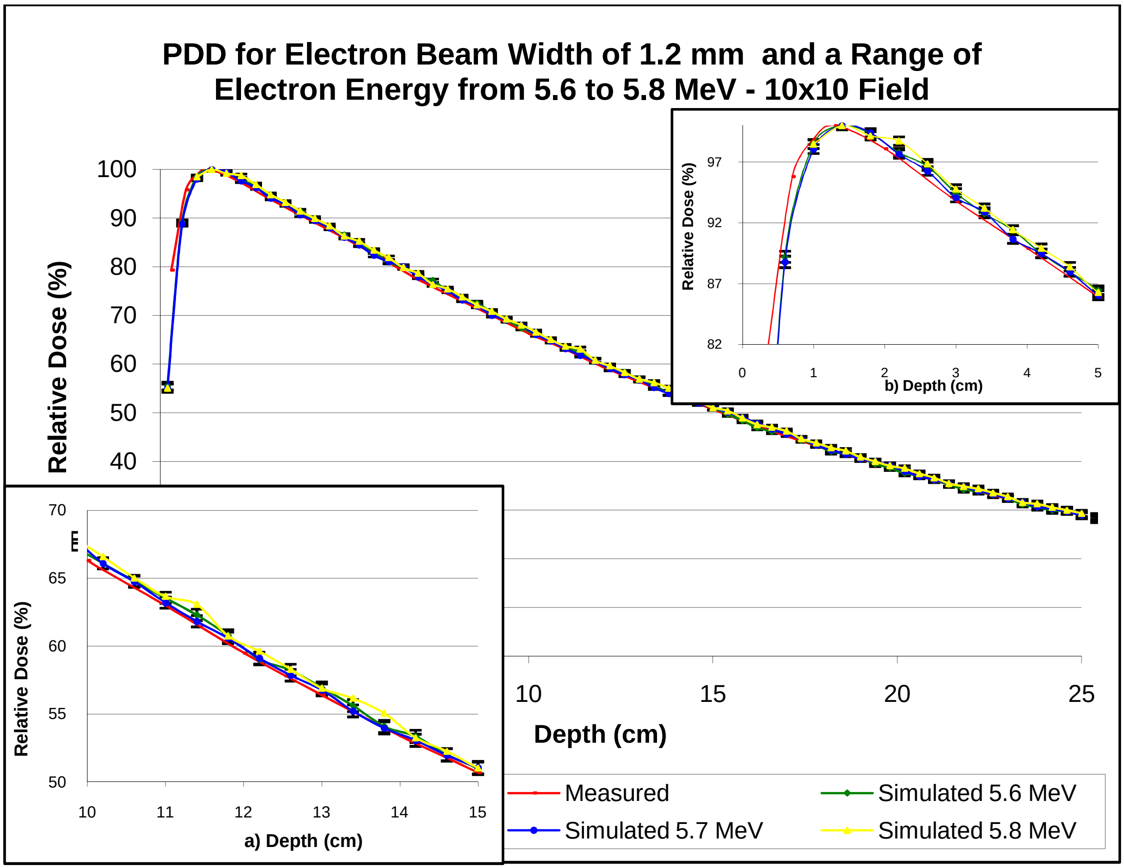

Figure 5.2. 2: Comparison of the PDD for energy from 5.6-5.8 MeV and FWHM of 1.2 mm. The insert shows the build-up region in smaller scale which reveals a maximum discrepancy of 3%.

The region beyond D_{max} in the PDD curve shows very good agreement for all of these energies. Although the insert a) of figure 5.2.2 shows discrepancies of less than 1% between the measured and all of the simulated data, it is not clear from figure 5.2.2 which of the simulated PDD agrees best with the measured PDD. For this reason, the graph of the percentage difference between the measured and simulated PDD was made. Figure 5.2.3 shows the percentage dose difference (ΔD) graph for a range of energies from 5.6 to 6 MeV. The build-up region was not included in this graph because the uncertainty of the data points in this region was high. The perfect energy is the one that overlaps with the horizontal axis of the graph. Practically this is not possible, so the best energy is the one that is where ΔD is the smallest. The yellow curve from figure 5.2.3 crosses the horizontal axis at several points. But apart from these points, the curve is moving away from the horizontal axis. Similar situation occurs for the light blue curve in the opposite direction. This implies that the energies of 6 MeV and 5.6 MeV are the upper and lower suitable energy limits and the right electron energy is within this range. The green and red curves which correspond to energies of 5.7 and 5.8 MeV confirm the above observation. They are positioned in between the yellow and blue curves and their data points fluctuate around (rather than moving away) the horizontal axis. A line of best fit can be generated from the green and red curves to determine which of them have ΔD closest to 0%. Observation from the first 4 cm along the Z axis is sufficient to show that the green curve has ΔD closest to 0%. As a result, it is concluded that the best electron energy for the X-ray linac head model is 5.7 MeV.

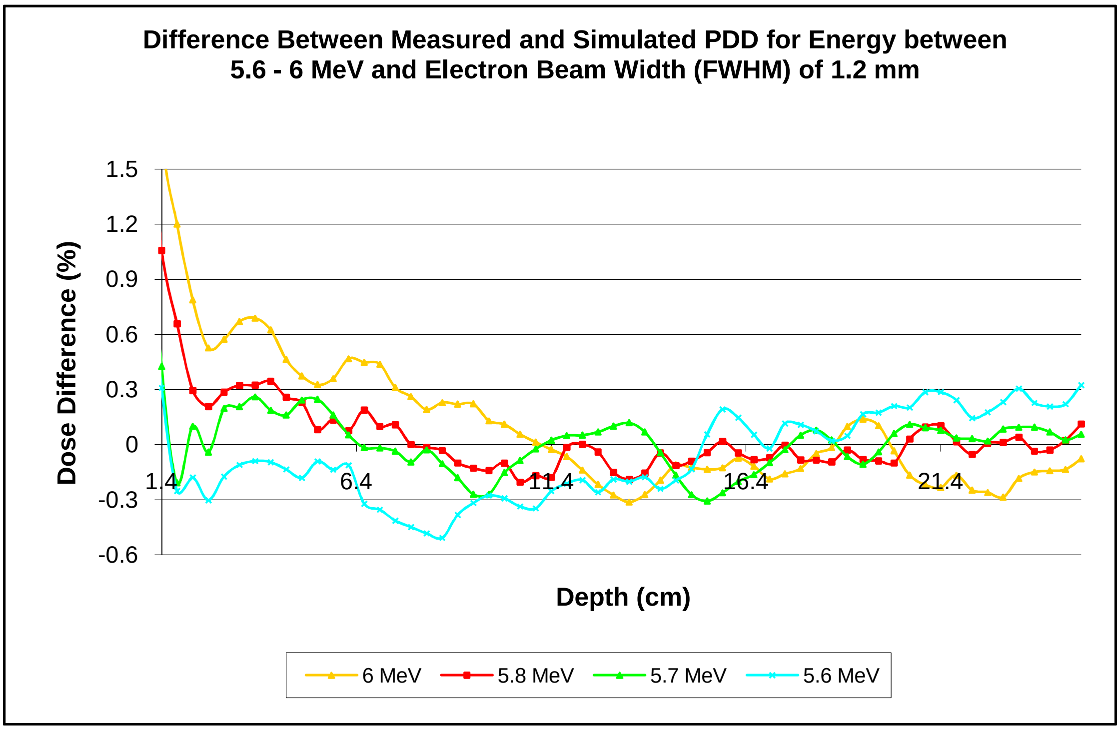

Figure 5.2.3: Comparison of the PDDs for energies from 5.6-6 MeV using the percentage dose difference plot. The build-up region was omitted so that clearer detail in the fall-off region can be seen.

The X-ray beam profiles produced by the linac head model with energy of 5.7 MeV and a range of electron beam width (FWHM) values from 0.9 to 1.5 mm were analysed for the selection of the best electron beam width (FWHM). Figure 5.2.4 indicates that the X-ray beam profiles are very sensitive to the electron beam width. The relationship between them is not clear. The results in the literature showed that there was a polynomial relationship between the in-air off-axis ratio at 15 cm from the central axis and the electron beam width (Sheikh-Bagheri and Rogers 2002). The dips and humps are present in the simulated profile for all values of the electron beam width (FWHM) in figure 5.2.4. As discussed in section 4.4 they were caused by a systematic error in the model of the linac head, possibly the flattening filter. The exact cause of these irregularities has not been identified in the current work but it was observed that the fluctuations were larger for some FWHM than others. By taking the magnitude of these errors and the overall agreements between the measured and simulated X-ray beam profiles into account, the analysis from figure 5.2.4 shows that 1.3 mm is the best value for the electron beam width (FWHM).

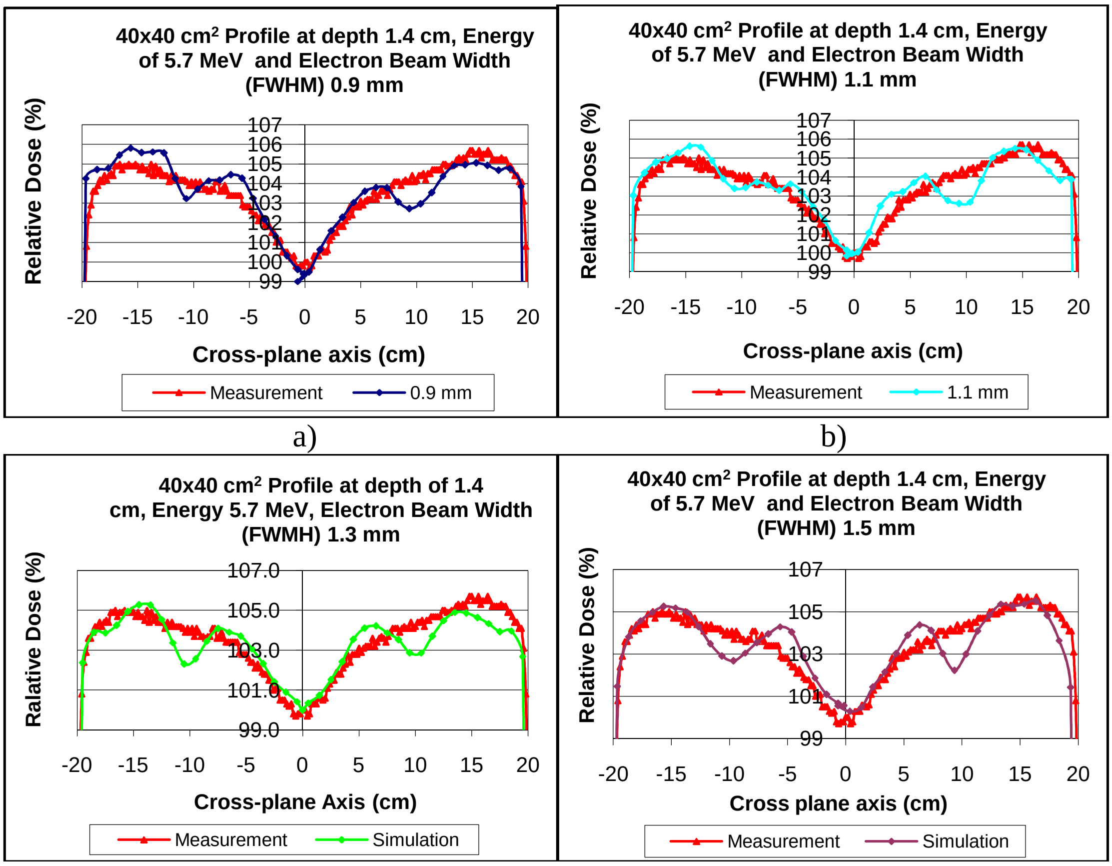

a) b)

c) d)

Figure 5.2.4: Comparison between the simulated and measured profiles for electron beam energy of 5.7 MeV and electron beam spread (FWHM) from 0.9-1.5 mm.

Further analysis of the cross-plane profile corresponding to the electron beam width (FWHM) of 1.3 mm shows that all data points agree within 1% (figure 5.2.5). The uncertainty in the simulation and the error in the measurement are ±0.7% and ±0.5% respectively. A small displacement between the measured and simulated profiles on the right hand side penumbra is not of concern. The reason is because the resolution of the measured data is finer than that of the simulation data. This displacement is about 2 mm, which is still less than the simulated and measured uncertainty in the cross-plane. It should be noticed that the measure profiles exhibit asymmetry relative the central axis. This is due to the imperfect tuning of the electron beam before incident the X-ray target in the real linac head. This imperfect tuning cannot be modelled by the BEAMnrc code and thus exact matching of the measured and simulated profiles is not observed

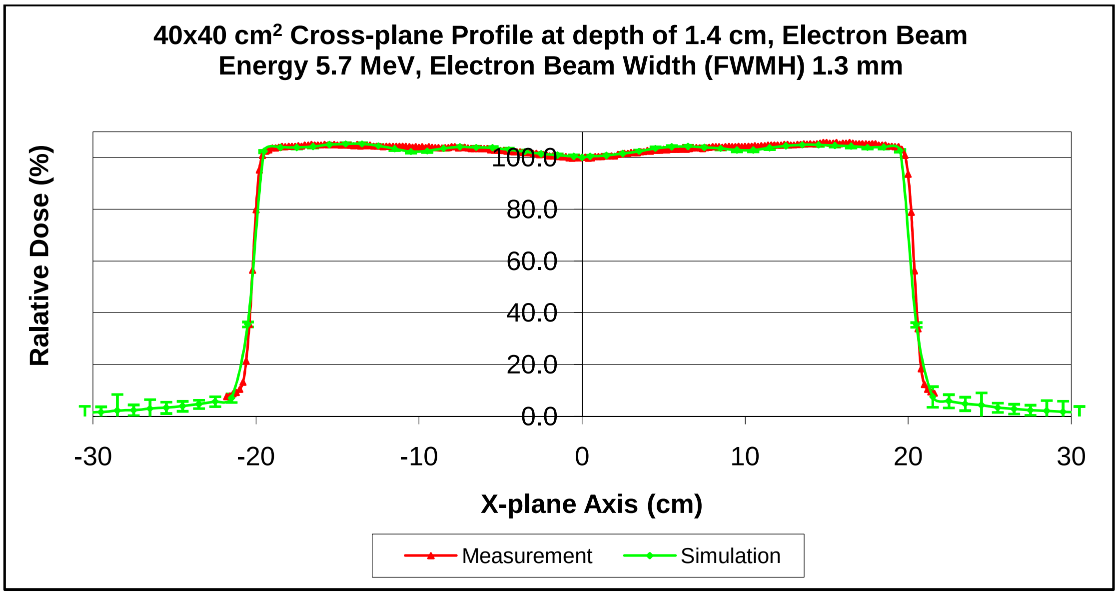

Figure 5.2.5: Measured and simulated cross-plane profiles for electron beam energy of 5.7 MeV and electron beam width (FWHM) of 1.3 mm. Agreement within 1% is achieved for this electron beam width (FWHM) value.

The in-plane profile shows similar behaviour as the cross plane (figure 5.2.6). The dips and humps are still present along the plato region of the profile (insert of figure 5.2.6). This suggests that the cause of the error is radially symmetric about the central axis, which supports the assumption that the error came from the modelling of the flattening filter. In addition, the dose agreement is very similar to that of the cross plane. Very good match is obtained in the central axis and in the penumbra regions.

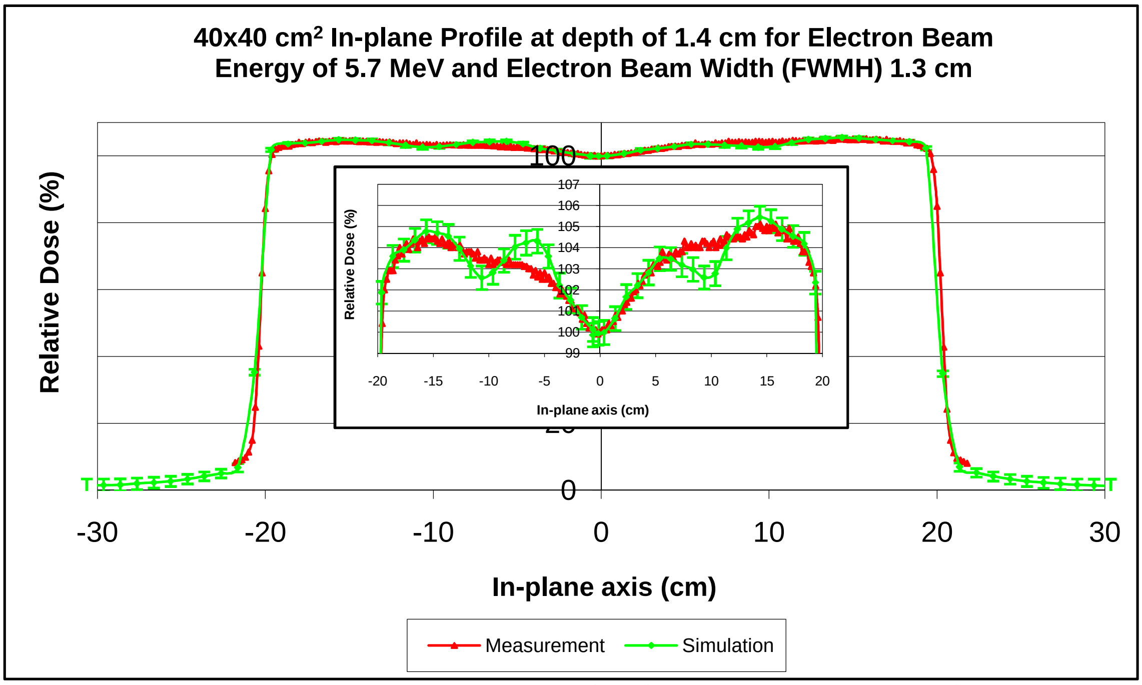

Figure 5.2.6: Measured and simulated in-plane profiles for electron beam energy of 5.7 MeV and FWHM of 1.3 mm. Agreement of less than or equal 1% is achieve for this FWHM.

The best electron beam energy and beam width (FWHM) at this stage of the analysis are 5.7 MeV and 1.3 mm respectively. It should be noticed that the best electron beam energy and beam width (FWHM) were selected based on the analysis of the X-ray percentage depth dose and beam profiles independently. It is not guaranteed that when the combination of this energy and FWHM values is used in a linac head model, the same level of agreement between the measured and simulated PDD and beam profiles is still achieved. In the next step the 10x10 cm^2 PDD for a range of energies from 5.6 to 5.8 MeV was analysed, but this time the FWHM of 1.3 mm was used. The result of this analysis is shown in figure 5.2.7.

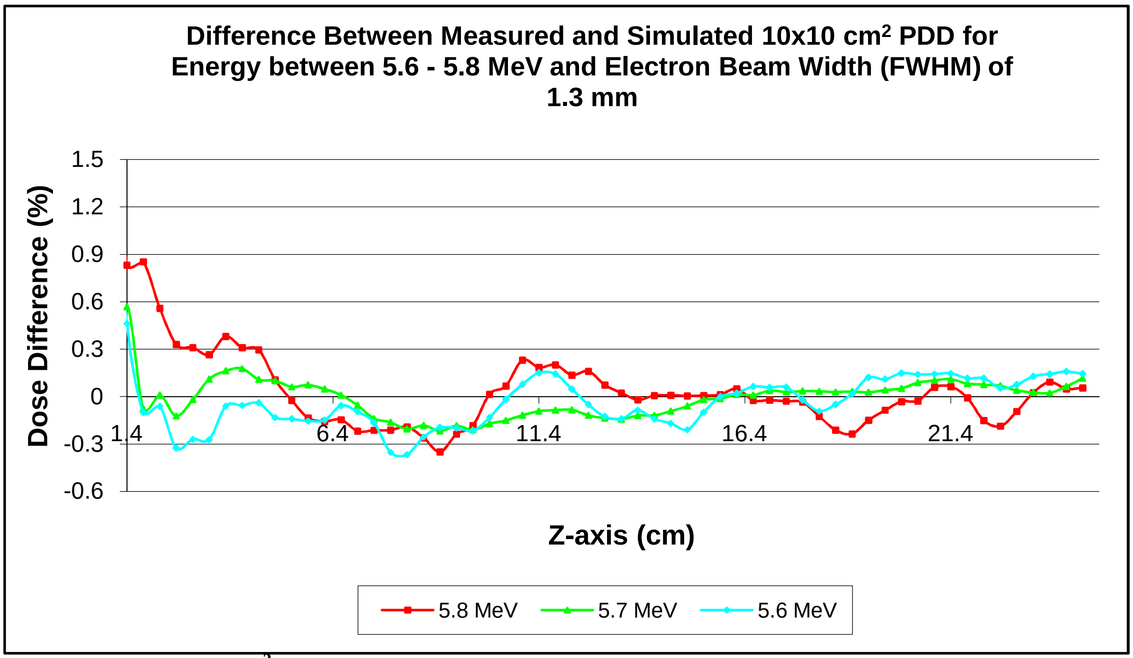

Figure 5.2.7: 10x10 cm^2 percentage dose difference for electron beam energy from 5.6 to 5.8 MeV and electron beam width (FWHM) of 1.3 mm.

There is a small change in the PDD difference pattern compared to figure 5.2.3 where the electron beam width value of 1.2 mm was used. However, the energy of 5.7 MeV still provides the PDD that agrees the best with the measured data. Furthermore, the electron beam width of 1.3 mm gives even better agreement than that of 1.2 mm (figure 5.2.8). This result also agrees with the finding of Sheikh-Bagheri and Rogers who reported that the change in the FWHM did not significantly change the percentage depth dose. One thing to note in figure 5.2.8 is that the differences between the two curves are within the uncertainty of the simulation. This means that the observed differences also come from the statistical simulation errors and not from the “real” difference between the simulated and measured electron beam width values. At this point, however, there is sufficient evidence to conclude that the combination of electron beam energy and FWHM of 5.7 MeV and 1.3 mm respectively are the best values for the model of the linac head developed in the current work.

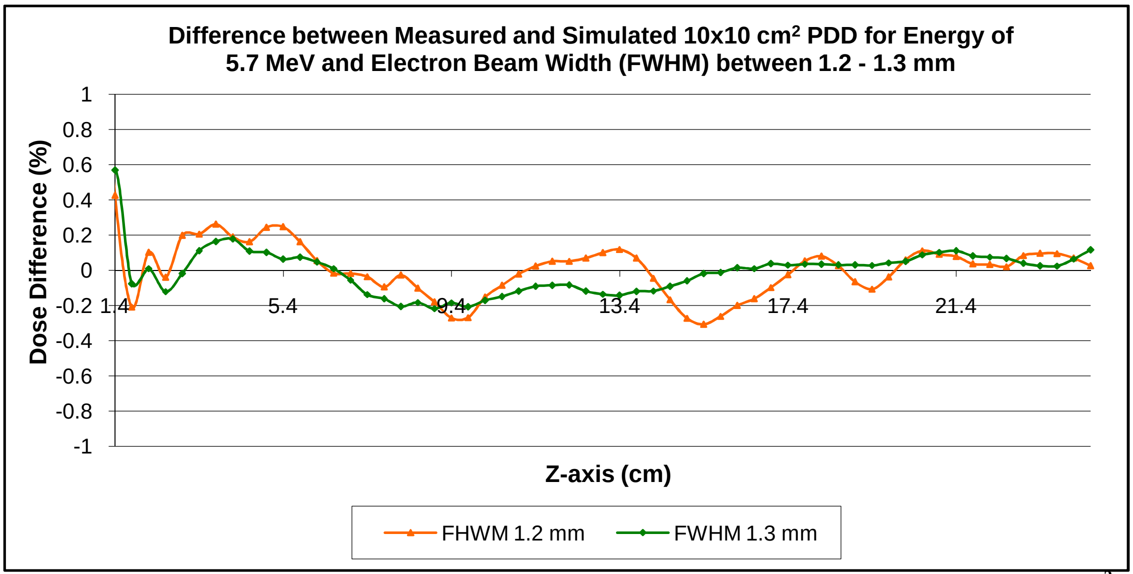

Figure 5.2.8: Percentage depth dose difference between the measured and simulated 10x10 cm^2 PDD for electron beam energy of 5.7 MeV and electron beam width of 1.2 and 1.3 mm.

Selection of random seed in the simulation should not affect the outcome of the simulation (Nitschike and Sim 1993). In order to verify this, the simulation of the 10x10 cm^2 X-ray PDD and 40x40 cm^2 cross-plane beam profile at source to surface distance of 100 cm were carried out using the same setup and modelling parameters except for the random seed value.

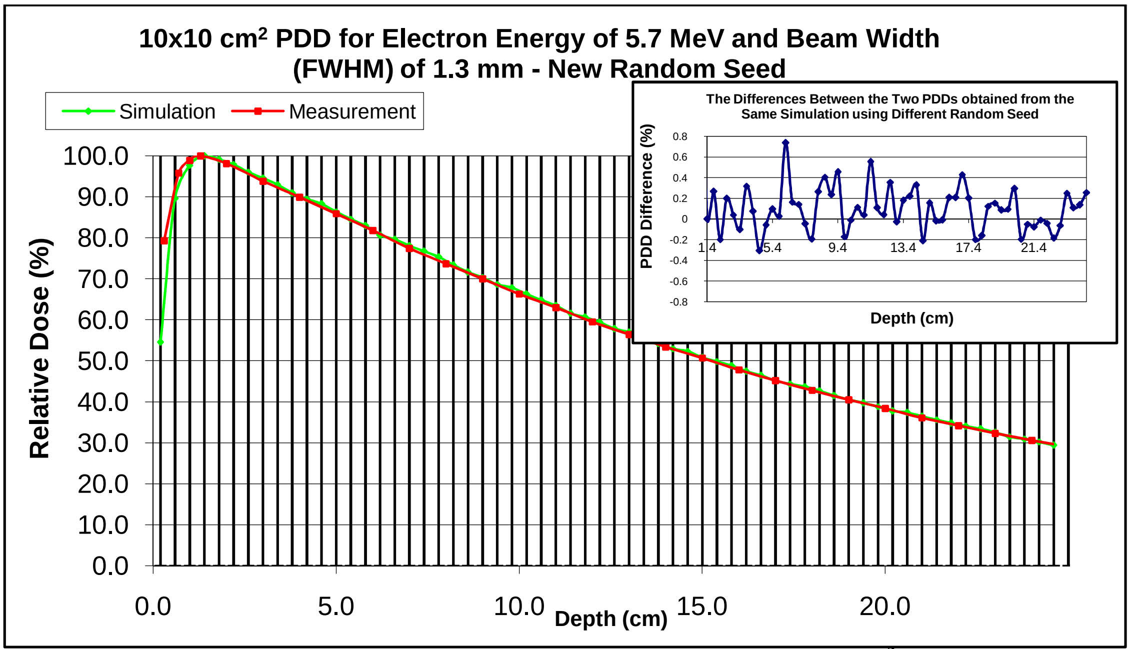

Figure 5.2.9: Comparison between the measured and simulated 10x10 cm^2 PDD curves. The simulated PDD curve was acquired using new random seed value. The insert in this figure shows the percentage difference between the two simulated PDD curves that differ only by the random seed value selected in the simulation.

Figure 5.2.9 shows the overlap of the simulated and measured 10x10 cm^2 X-ray PDD curves. The electron beam energy and beam width of 5.7 MeV and 1.3 mm respectively were used for the linac head model in this investigation. The simulated PDD curve was acquired using the same setup and modelling parameters except for the random seed value. There is no obvious change in the general shape of the simulated PDD curve. The measured and simulated PDD curves matched very well. The curve describing the percentage difference between two simulated PDDs which were acquired using different random seed value is shown in the insert of figure 5.2.9. Beyond the depth of maximum dose, the maximum difference is 0.74% and most data points show the differences of less 0.5%. This is less than the combined uncertainty from two simulations used in the comparison.

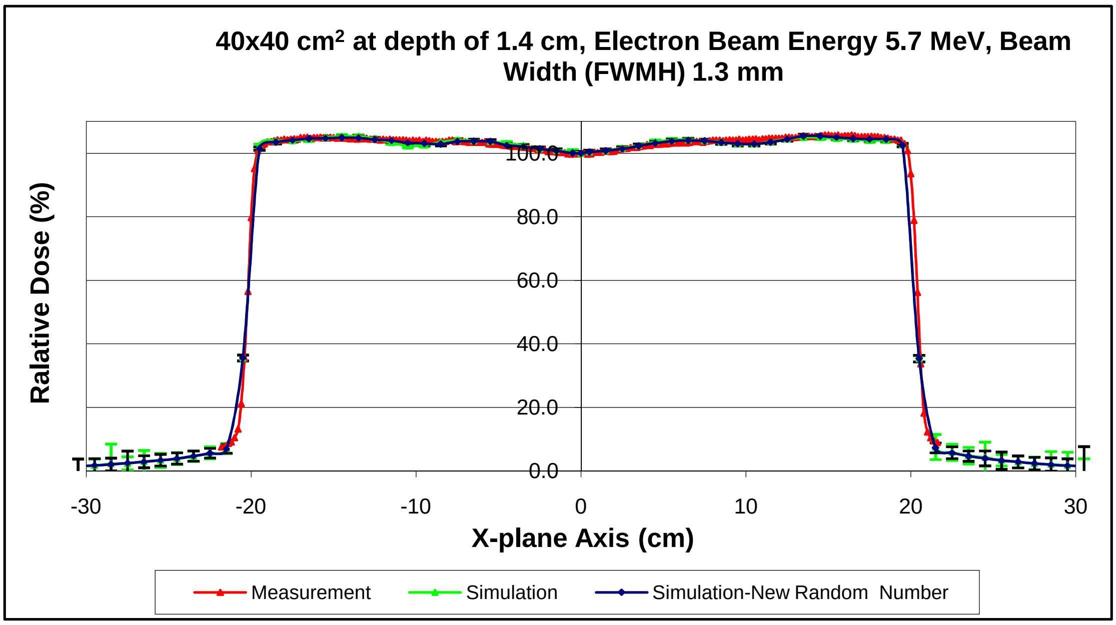

Figure 5.2.10: Measured and two simulated X-ray beam profiles in the cross-plane. The only difference in the simulated beam profiles is the random seed value selected in the simulation.

The 40x40 cm^2 X-ray beam profile was also analysed. Figure 5.2.10 shows the overlap of the measured and two simulated X-ray beam profiles in the cross-plane. The electron beam energy and beam width of 5.7 MeV and 1.3 mm were used in the linac head model. The difference between the two simulated X-ray beam profiles is the random seed value. There is no significant difference between the two simulated beam profiles. They are both in good agreement with the measured beam profile. Based on this investigation, it can be concluded that different random seed value does not have an impact on the results of the Monte Carlo simulation.

The combination of energy and FWHM of 5.7 MeV and 1.3 mm also gives good agreement with the measured profiles at different depths and for different field sizes as shown in figure 5.9 a), b), c) and d). The shape of the simulated profiles conforms very well to the measured profiles. There were small differences in the fall off region of the 10x10 cm^2 profiles for depths of 1.4, 10 and 20 cm. The reason for these differences is unknown, however they were well within the tolerance set in the current work. In addition, the agreement in the plato region is within 1% and the penumbra regions matched very closely. The results from figure 5.9 provide further confirmation for the selected values of energy and FWHM of 5.7 MeV and 1.3 mm respectively. They have also shown that EGS Monte Carlo system can model radiation scatter accurately.

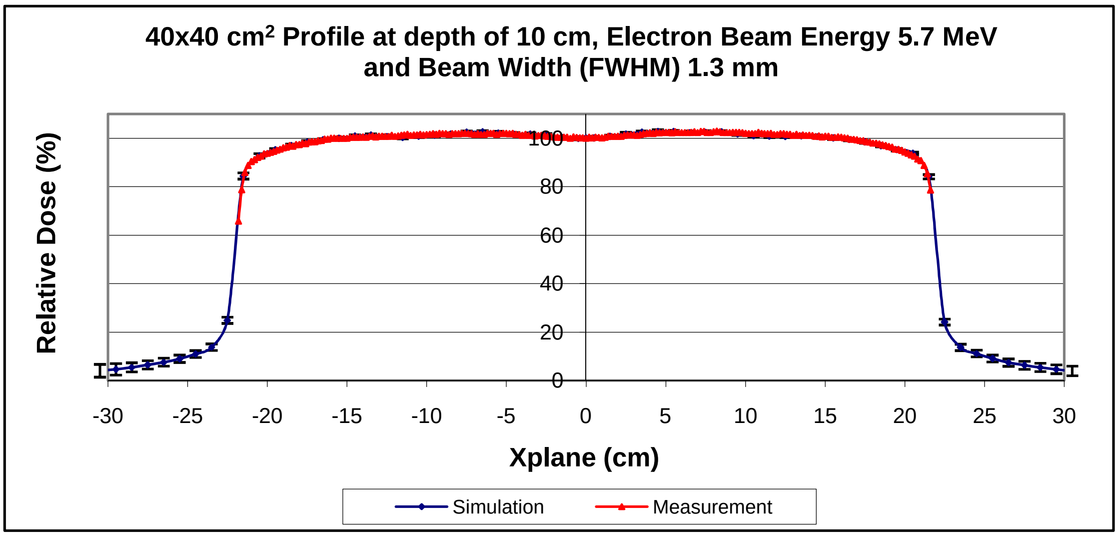

Figure 5.2.11: a) Cross-plane profile at depth 10 cm for electron beam energy of 5.7 MeV, electron beam width of 1.3 mm and field size of 40x40 cm^2.

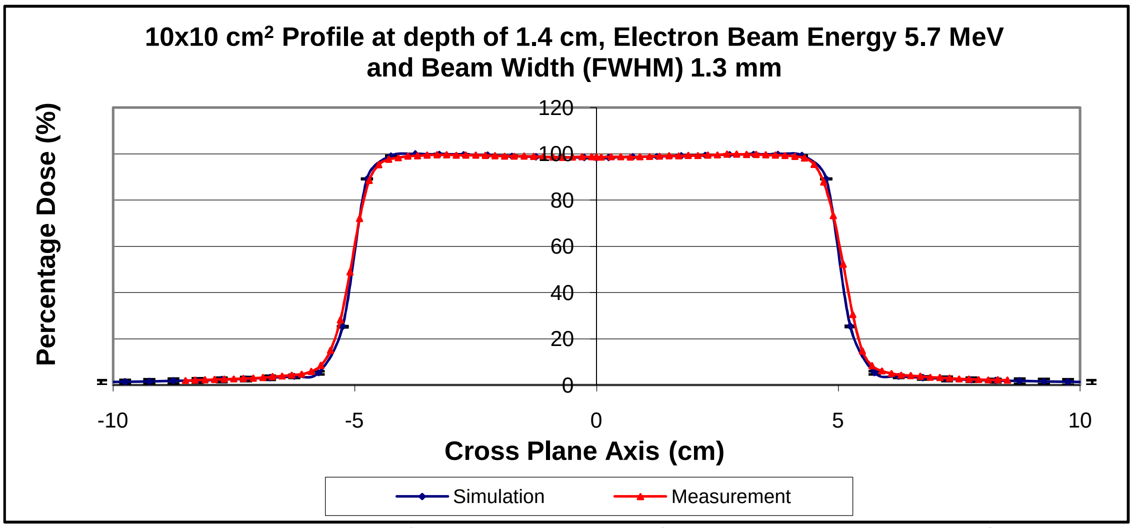

Figure 5.2.12: b) Cross-plane profile at depth 1.4 cm for electron beam energy of 5.7 MeV, electron beam width of 1.3 mm and field size of 10x10 cm^2.

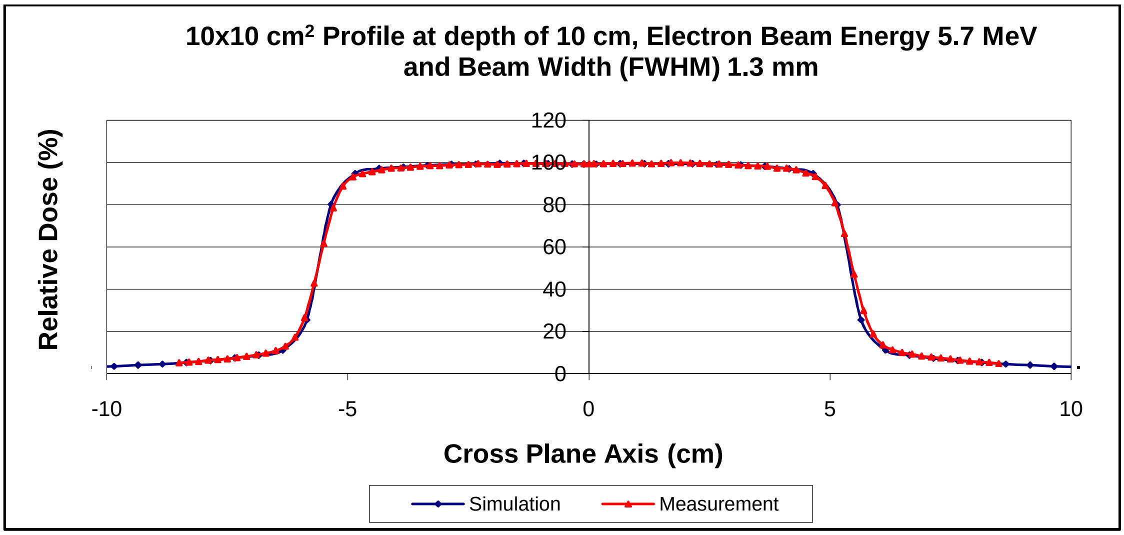

Figure 5.2.13: c) Cross-plane profile at depth 10 cm for electron beam energy of 5.7 MeV, electron beam width of 1.3 mm and field size of 10x10 cm^2.

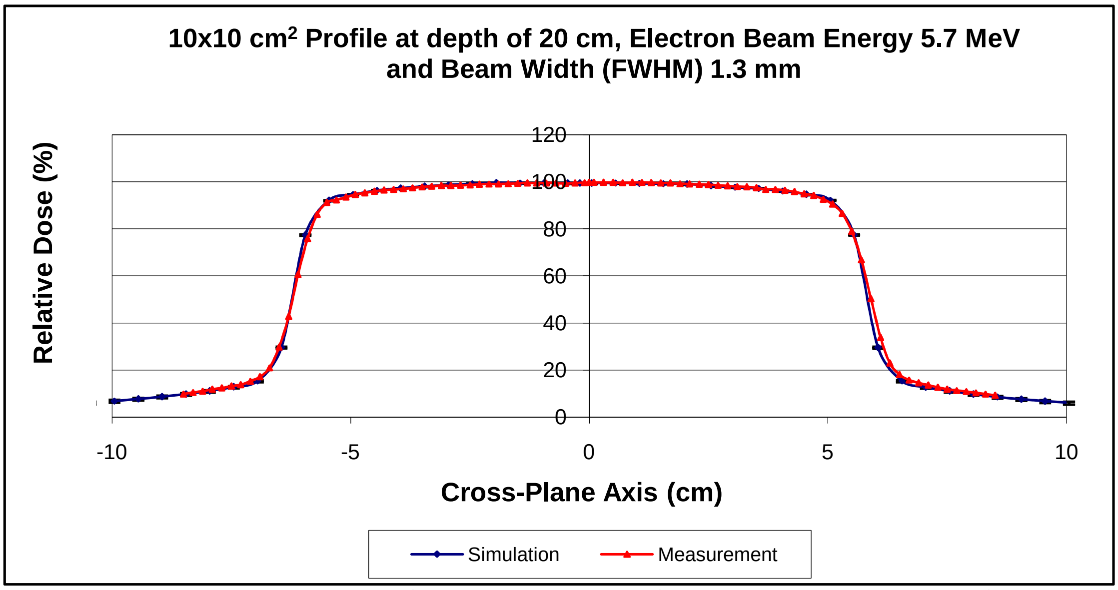

Figure 5.2.14: d) Cross-plane profile at depth 20 cm for electron beam energy of 5.7 MeV, electron beam width (FWHM) of 1.3 mm and field size of 10x10 cm^2.

5.3 Summary

The selection of the energy and FWHM of the electron beam was performed in detail in this work. It was observed that the PDD varied slowly with the electron beam energy. The PDD difference analysis was required to detect differences in the PPD for energy differences of 0.1 MeV. The variation of the profiles due to different FWHM values did not follow any obvious pattern. It was observed that some values of the FWHM caused more fluctuations than others. Substantial data was analysed to show that best values of the electron beam energy and FWHM of the electron beam width in the model of the 600C/D Varian linac head are 5.7 MeV and 1.3 mm respectively.

By using the selected electron beam energy and FWHM of the electron beam width value in the Varian 600C/D linac head model, it was shown that agreements of less than 1% between the measured and simulated X-ray PDD and beam profiles can be achieved.

CHAPTER 6

MONTE CARLO MODELLING OF THE VARIAN MK2 PORTAL VISION EPID

6.1 Modelling of the EPID using DOSXYZnrc

The Varian SLIC EPID (MK2 Portal Vision system, Varian Inc., Palo Alto, CA, USA) was modelled using DOSXYZnrc. The structure and density of the EPID was obtained from the literature (Spezi and Lewis 2002). Modelling was restricted to the region containing the ionisation chamber matrix (refer to figure 2.2.1.1) with the surface area of 32.5x32.5 cm^2. The ionisation chamber matrix was made of 256x256 voxels uniformly separated by a distance of 0.127 cm in both the X and Y directions in the DOSXYZnrc coordinate system. The thickness of all EPID layers in the Z direction was 2.1 cm as shown in figure 6.1. The Printed Circuit Board (PCB) was modelled by two separate layers made of glass and PMMA materials. The layer of glass had a thickness of 0.04 cm and was positioned on top of the PMMA layer of the same thickness. All other PCB layers were modelled in the same way. There was a total of 11 layers combined to make the internal structure of the SLIC EPID matrix. The composition of each layer was created by a program in the EGSnrc system called PEGS4.

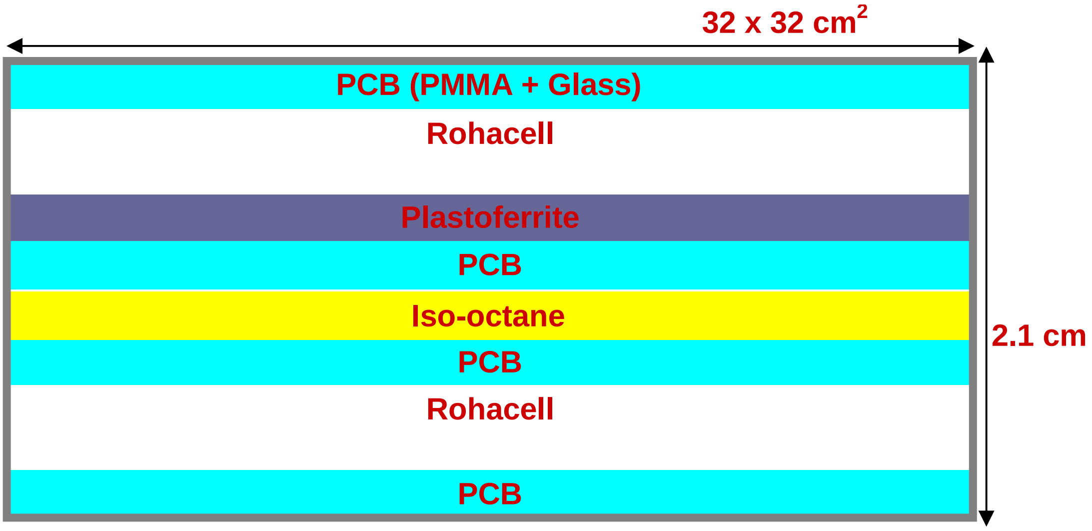

Figure 6.1: Side view of the layers in the active area of the EPID (Spezi and Lewis 2002). The drawing is not to scale.

6.2 Simulation and Experimental Setups

The model of the EPID described above was verified by comparing the Monte Carlo, Pinnacle TPS and transmitted dose maps measured in the EPID sensitive's layer for three different phantom setups. The first setup used an open field with only air between the radiation source and the EPID, called an **Openfield** setup. This is shown in figure 6.2.1. A 6 MV beam from Varian 600CD linac and radiation field size of 15x15 cm^2 were used in all EPID simulations. The radiation source was at a distance of 140 cm from the iso-octane sensitive layer. Taking into account the inherent build-up material and the RW3 solid water (PTW Freiburg, Germany) layers positioned on top of the EPID in the current work, the Source to RW3 build-up Surface Distance (SSD) was 138.5 cm. The RW3 layer acted as an extra build-up necessary to achieve electronic equilibrium at the EPID's sensitive layer. When the condition of electronic equilibrium is achieved, maximum EPID response is detected. An extra build-up layer is required because the water equivalent thickness from the EPID surface to the sensitive layer of the EPID is only about 1.0 cm. Generally, for an X-ray beam energy of 6 MV, the build-up region in water is about 1.3 to 1.5 cm from the surface. A thickness of 1.0 cm of water is therefore not sufficient to generate electronic equilibrium at the EPID sensitive layer. Mohammadi and Bezak 2006 have shown in their investigation that an extra build-up of 0.5 cm RW3 was necessary in order to achieve electronic equilibrium (Mohammadi and Bezak 2006). Since the calibration factor for measured transmitted dose in the EPID was obtained from this work, this extra build-up was thus included in the current simulation work as well.

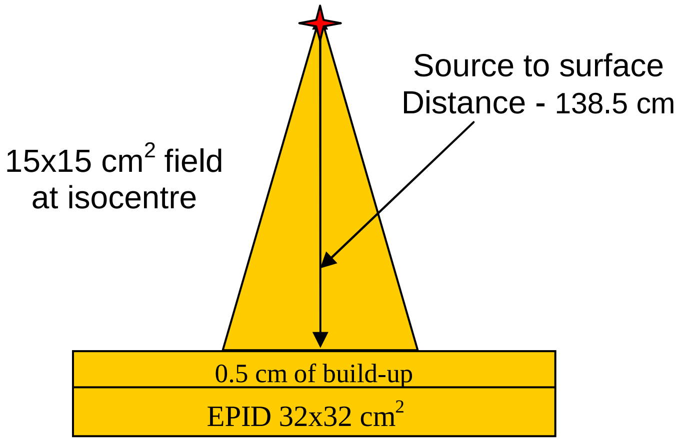

Figure 6.2.1: Simulation set-up of the transmitted dose in the EPID with no phantom in the radiation field. The sensitive layer is 1.0 cm from the EPID surface and 140 cm from the source.

The second setup, called **15cmphant,** consisted of 15 cm of solid water phantom between the radiation source and the EPID. The centre of the 15 cm water phantom was positioned at the iso-centre of the linac. This setup had an air gap of 31.0 between the bottom of the phantom and the EPID and the source to phantom surface distance was 92.5 cm as shown in figure 6.2.2.

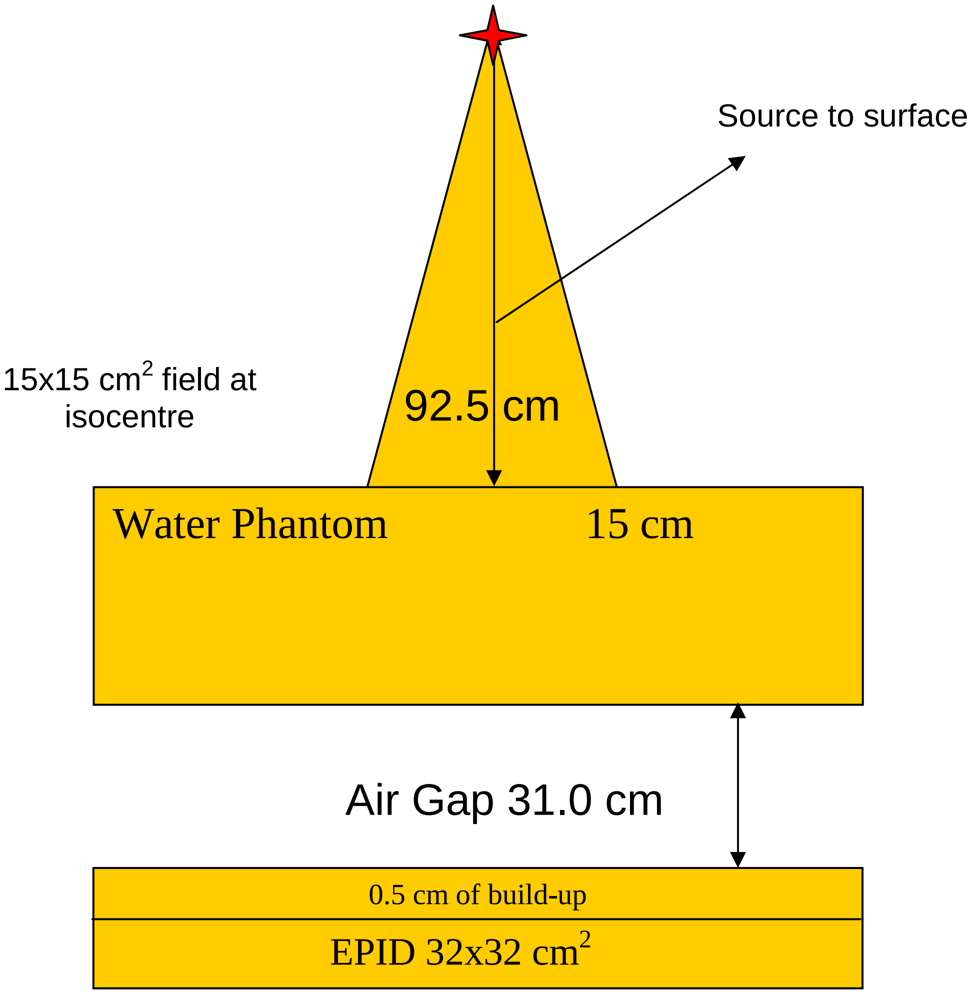

Figure 6.2.2: Set-up for the simulation of the transmitted dose in the EPID with 15 cm thick water phantom positioned in the radiation field. The sensitive layer of the EPID is 140 cm from the source.

The third setup called **RANDO** setup is shown in figure 6.2.3. In this setup, the humanoid phantom, RANDO, was positioned between the radiation source and the EPID. RANDO has a thickness of 22.5 cm measured from the centre of the chest wall in the anterior and posterior (A/P) direction. The metal wire was used to mark a point in the centre of the chest wall and on both sides at midline of RANDO during the Computed Tomography (CT) scan. These points were used as landmarks for RANDO positioning on the treatment couch and also in the Monte Carlo simulation. Taking the RANDO thickness and the position of the landmarks into account, the source to

RANDO surface distance and the air gap between the RANDO and the EPID were 89.4 cm and 26.6 cm respectively. This scenario was quite complex, as the radiation field was positioned in an area that contained large curvatures (breast) and inhomogeneities (lung).

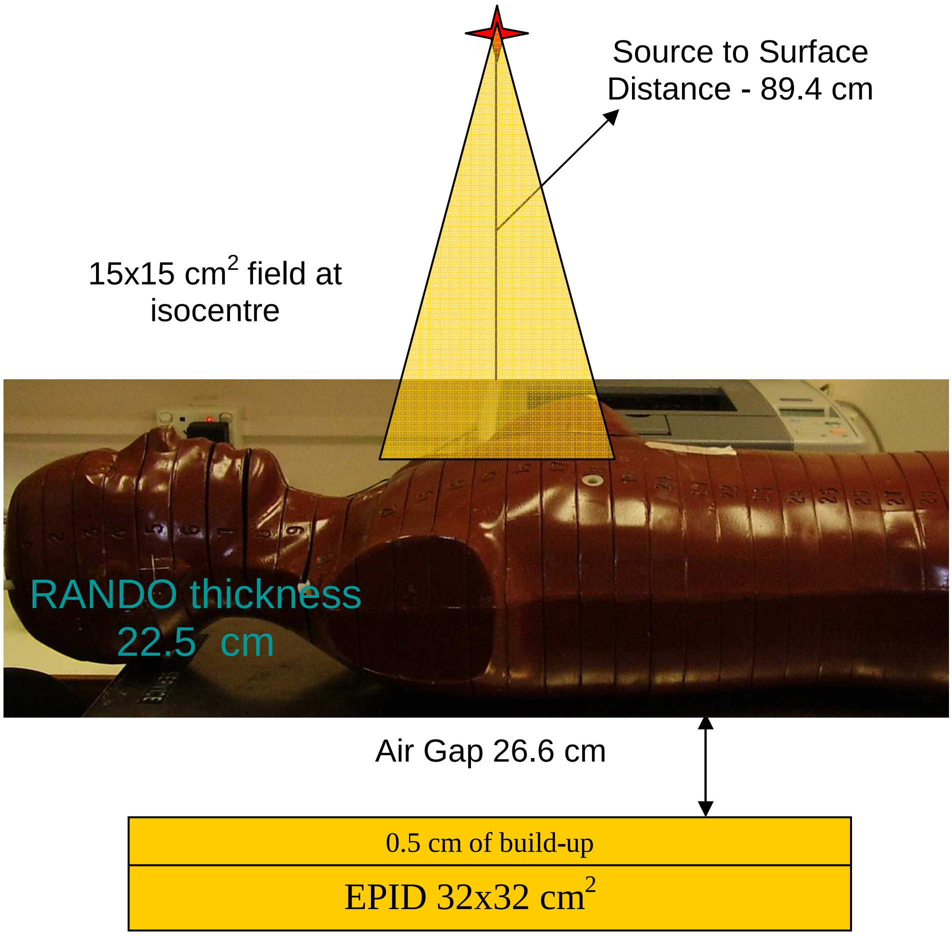

Figure 6.2.3: Set-up for the simulation of the transmitted dose in the EPID with RANDO in the field. The sensitive layer is 1.0 cm from the EPID surface and exactly 140.0 cm from the source.

In the first two setups shown above, the air gap and the water phantom were modelled as single phantoms together with the EPID in DOSXYZnrc. The problem occurred when a CT scan of the RANDO phantom was used to replace the water phantom in the third setup (figure 6.2.3). DOSXYZnrc only allows using either the imported RANDO CT scan or a manually generated phantom input file for the simulation (this contains the modelled EPID). The setup in figure 6.4 shows that combination of these two objects (ie CT scan of RANDO and an input file containing modelled EPID) was required for the simulation.

The in-house MATLAB code created by Reich, Royal Adelaide Hospital, 2006 was used to overcome the difficulty encountered in the third setup (figure 6.2.3). This code has the following functionalities:

a) It allows the dimensions of the RANDO CT images to be extended (from 512x512 pixels to 1024x1024 pixels) by adding extra pixels of air density around the original CT images in DICOM format.
b) Create the model of the EPID and concatenate this model to the extended air region.

The density of each layer of the EPID was assigned using gray scale value in Mr Reich's code. The relationship between density and gray scale value was determined in this work using the DICOM CT data set of RANDO as a reference. Since both Pinnacle and MATLAB can read and output density and gray scale value respectively from a DICOM image format.

The output of Mr Reich's code is a DICOM image format of RANDO with an extended air region and the EPID underneath. This DICOM image format can be read by both Pinnacle and DOSXYZnrc codes for dose calculation in the same way as a normal DICOM image format of a patient. The detail of how DOSXYZnrc read in DICOM image format can be found in DOSXYZnrc user manual (Rogers, Walters et al. 2004).

6.3 Analysis of the Transmitted Dose

The transmitted dose in the EPID from Monte Carlo simulations, Pinnacle TPS calculations and measurements were compared to verify the developed Monte Carlo EPID model and to assess the agreement between these modalities. In the comparison between the Pinnacle TPS and Monte Carlo calculated transmitted doses, the EPID model shown in figure 6.1 was used in both the Pinnacle and Monte Carlo simulations to obtain the dose data. Calculations in Pinnacle were performed using the collapsed cone convolution superposition algorithm (v6.2b, Phillips Medical Systems). When comparing the measured and Monte Carlo transmitted doses, the EPID was modelled using the 32x32x2 cm^2 slab of water in the Monte Carlo simulation. This was consistent with the measured data where the EPID transmitted dose was calibrated against the dose in water. The transmitted dose grids resolution for Monte Carlo, Pinnacle and measurement are shown in table 6.3.1. The simulation times were also included for the Monte Carlo dose calculations.

Open Field Setup	Real EPID Model			Water Equivalent EPID Model		
	Voxel Size (mm)	Time (hr)	# Particles	Voxel Size (mm)	Time (hr)	# Particles
Monte Carlo	1.27x1.27	22.0	4x10^{8}	1.27x1.27	72.2	1.6x10^{9}
Pinnacle	2.5x2.5	-	-	2.5x2.5	-	-
Measurement	1.27x1.27	-	-	1.27x1.27	-	-

a)

15 cm Water Phantom Setup	Real EPID Model			Water Equivalent EPID Model		
	Voxel Size (mm)	Time (hr)	# Particles	Voxel Size (mm)	Time (hr)	# Particles
Monte Carlo	1.27x1.27	202.1	4x10^{8}	1.27x1.27	121.6	4x10^{8}
Pinnacle	2.5x2.5	-	-	2.5x2.5	-	-
Measurement	1.27x1.27	-	-	1.27x1.27	-	-

b)

RANDO Setup	Water Equivalent EPID Model		
	Voxel Size (mm)	Time (hr)	# Particles
Monte Carlo	2.5x2.5	66.3	2x10^{8}
Pinnacle	2.5x2.5	-	-
Measurement	1.27x1.27	-	-

c)

Table 6.3.1: The voxel sizes of the Monte Carlo, Pinnacle and measured transmitted dose map for a) open field , b) 15 cm water phantom and c) RANDO setup. Variations of the number of particles and the calculation time for three different setups for Monte Carlo calculation are also shown. The voxel sizes and the number of particles or the calculation time determine the magnitude of the uncertainty of the calculation.

The transmitted dose map from the DOSXYZnrc simulation program was extracted by an in-house MATLAB code created in this work (Appendix B). Another in-house MATLAB code written by Mohammadi, Royal Adelaide Hospital was used to derive the measured transmitted dose map from the EPID signal. The transmitted dose map from the Pinnacle treatment planning system was extracted using the in-house MATLAB code written by Reich, Royal Adelaide Hospital 2006. The dose map analysis program called Omnipro I'mRT was used to evaluate the agreement between the MC, Pinnacle and measured 2D dose distributions and beam profiles in the EPID's sensitive layer (Scanditronix Wellhofer, OmniPro I'mRT v1.4b, 2005).

6.4 Comparison of the Transmitted Dose for an Open (in Air) Field Phantom

MONTE CARLO VERSUS MEASUREMENT – OPEN FIELD SET UP

Measured and Monte Carlo calculated 15x15 cm^2 (nominal radiation field size at the isocentre) transmitted **cross-plane** dose profiles in the EPID sensitive layer for the Open Field setup are shown in figure 6.4.1a. The EPID model for this setup was simply made of water (as the EPID used in the measurements was calibrated in terms of dose to water) with 1.5 cm thickness to the sensitive layer. The Monte Carlo and measured profiles are displayed as red and green lines respectively. Both of the profiles were normalised to the central axis of the radiation beam. The estimated maximum dose error of measured profiles for the open field setup and all subsequent setups was 2.3% (Sheikh-Bagheri and Rogers 2002; Mohammadi and Bezak 2006). However, the dose errors in the measured dose profiles shown in figure 6.4 are below 1%. The uncertainty in the Monte Carlo dose calculation for this open field setup is in average about 0.6%. The vertical scale in figure 6.4.1 shows that the agreement between the measured and Monte Carlo calculated profiles is better than 2%. Both the horns and the dip in the Monte Carlo profiles were calculated accurately. Similar agreement was found in the comparison of the Monte Carlo simulated and measured **in-plane** profiles for the open field setup. The result is shown in figure 6.4.1b

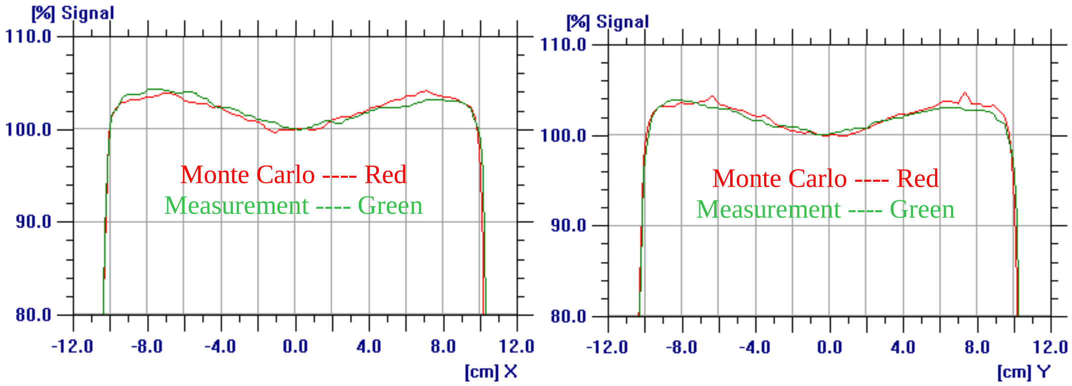

a) Cross-plane Profile b) In-plane Profile

Figure 6.4.1: Transmitted dose profiles from a 6 MV radiation beam of 15x15 cm^2 field size acquired in the EPID by Monte Carlo calculation and measurement a) in the cross-plane and b) in the in-plane for an Open Field setup of figure 6.2.1.

Figures 6.4.2a and 6.4.2b show the 2D dose maps calculated by the Monte Carlo program and obtained from measurement respectively. The dose map comparison shows a good agreement almost everywhere in the EPID plane. The reason for this is because the scattering of the X-ray beam in air is small and there is no heterogeneity in the EPID model.

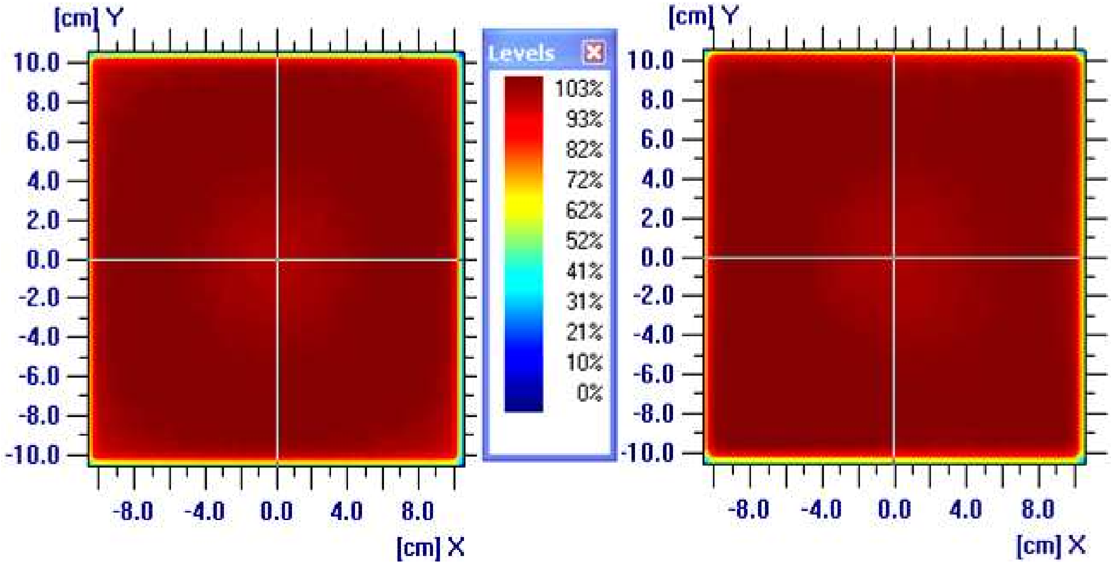

a) Monte Carlo Calculated Dose Map b) Measured Dose Map

Figure 6.4.2: Transmitted dose maps from a 6 MV radiation beam of 15x15 cm^2 field size acquired in the EPID: a) Monte Carlo calculation and b) measurement for an Open Field setup of figure 6.2.1. The dose grid resolutions for both dose maps are 1.27 mmx1.27 mm.

The quantitative assessment of the agreement between the dose maps can be performed using the gamma analysis tool in OmniPro Im'RT software. The gamma result for the MC calculated and measured dose maps for an open field is shown in figure 6.4.3. The total gamma score for this comparison is 99.5%. The gamma criteria for this comparison are 3% and 3 mm for dose difference and distance-to-agreement respectively. The gamma value for agreeing dose pixels is less than or equal to one - this falls into the blue-to-white region of the colour scale. The dose pixels not agreeing within the gamma criteria are displayed in red. There are small disagreeing regions in the left bottom corner of the gamma map. The exact reason for this is not known. Perhaps it was caused by statistical error in the Monte Carlo calculation because it is not seen in other corners of the dose map. Although the average uncertainty in the whole dose map is only 0.6%.

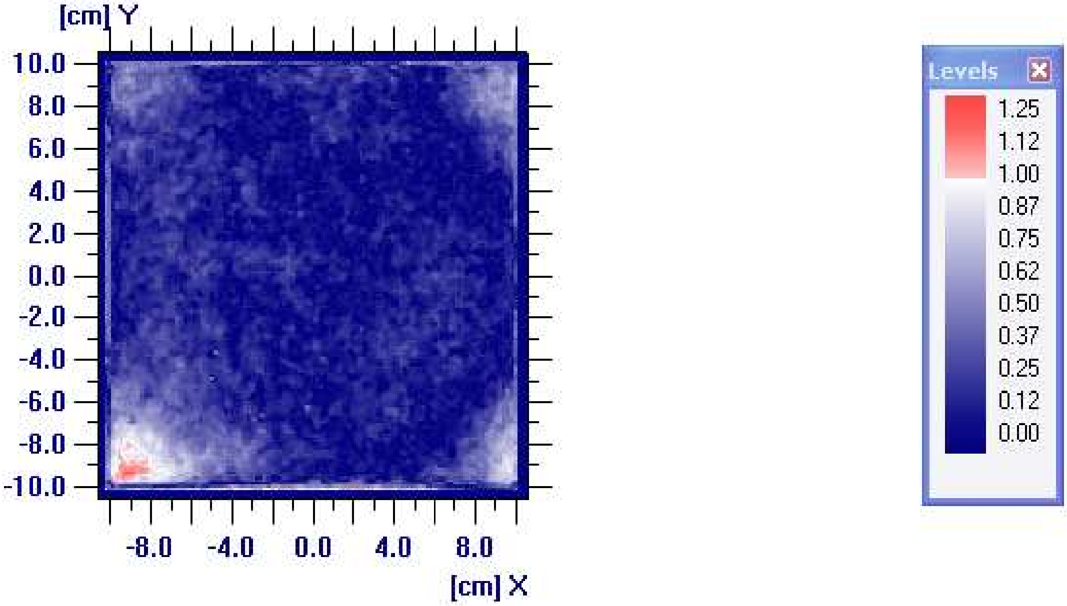

Figure 6.4.3: Gamma map result for the analysis of the Monte Carlo calculated and measured dose maps acquired for an Open Field setup in figure 6.2.1. The Gamma criteria are 3% and 3 mm for dose difference and DTA respectively.

Monte Carlo Versus Pinnacle – open field set up

The comparison between the Monte Carlo and Pinnacle calculated dose profiles was also performed for the open field setup. The EPIDs in the Monte Carlo and Pinnacle calculations in this case were modelled using the real EPID’s composition as opposed to water equivalent EPID for the Monte Carlo and measured transmitted dose comparison. The scatter conditions become more complicated due to the introduction of heterogeneous layers of materials in the EPID (refer to figure 6.1 for individual layers of the EPID model). The more complicated scatter of X-ray photons decreases the accuracy of the Monte Carlo calculation which is evident from the Monte Carlo cross-plane and in-plane profiles (red line) in figure 6.4.4 a) and b) respectively. The average uncertainty in the Monte Carlo calculation increases from 0.6 % to 1%. The vertical scale of the profiles was zoomed in to highlight the percentage dose differences between the Monte Carlo and Pinnacle profiles. It can be observed that the maximum dose difference between them is within 2% for both the in-plane and the cross-plane profiles. A noticeable feature in this comparison is that the dose difference increases towards the horns of the profiles. Because the increase is linear with the off-axis distance, it is presumed that this is a systematic error in the actual modelling of the EPID. The cause of the error is most likely caused by the EPID model in Pinnacle. The actual EPID is made of layers with variable thicknesses from 0.8 mm to 8 mm. However, Pinnacle TPS model uses a uniform thickness of 1 mm for the 0.8 mm thin layers.

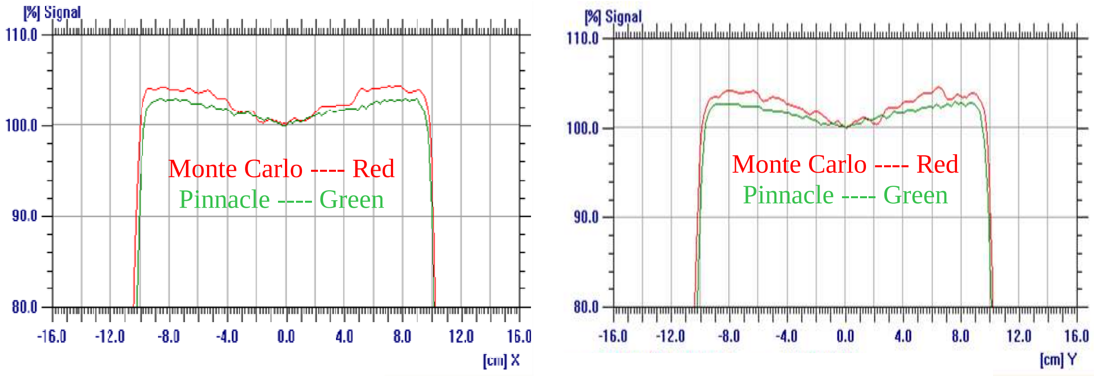

a) Cross-Plane Profile

b) In-plane Profile

Figure 6.4.4: Transmitted dose profiles from a 6 MV radiation beam of 15x15 cm^2 field size acquired in the EPID by Monte Carlo and Pinnacle calculation a) in the cross-plane and b) in the in-plane for an Open Field setup of figure 6.2.1.

The Monte Carlo and Pinnacle calculated dose maps for the real EPID model in the open field setup are shown in figure 6.4.5 a) and b) respectively. The dose difference of a few percents is difficult to pick up when comparing these two dose maps because the colour scale shows an interval of 10% between each colour.

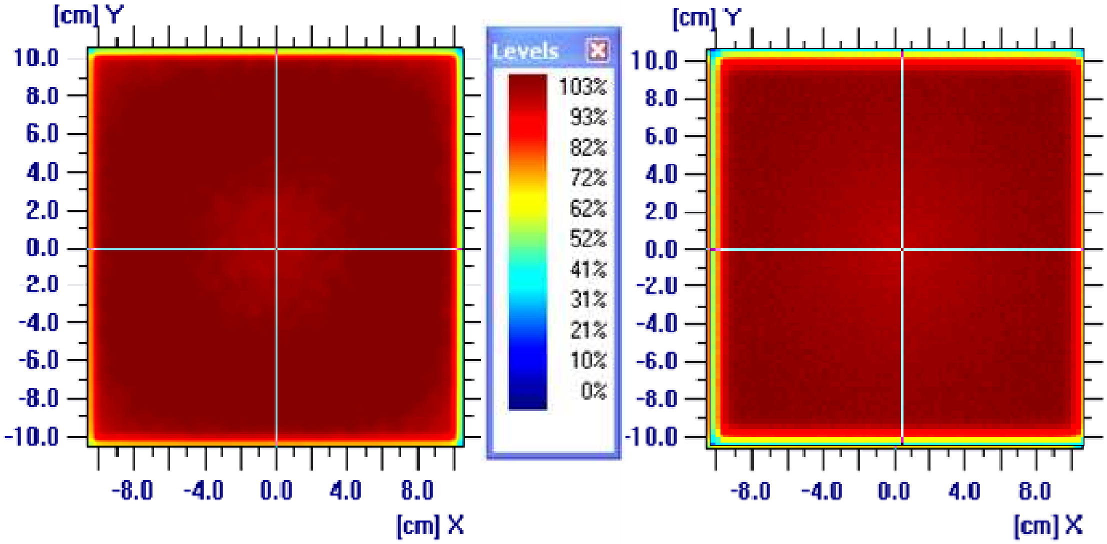

a) Monte Carlo Calculated Dose Map

b) Pinnacle Dose Map

Figure 6.4.5: Transmitted dose maps from a 6 MV radiation beam of 15x15 cm^2 field size acquired in the EPID: a) Monte Carlo calculation and b) Pinnacle for an Open Field setup of figure 6.2.1. The resolution for both dose maps is 1.27 mm.

The gamma map in figure 6.4.6 gives more useful information for this scenario. Because the gamma criteria were set to 3% and 3 mm for dose difference and DTA respectively, the systematic differences observed in the profile comparison will still result in a “PASS” in the gamma test. The total gamma score in this case is 98.1%. The blue colour region in the gamma map shows that the agreement is excellent in the central region of the dose map. The red colour region shows that there are some disagreements in the edges of the dose map. This is because the size of the Pinnacle dose map is slightly smaller than the Monte Carlo dose map. This is not shown in the comparison between the Monte Carlo and measured dose maps therefore it can be deduced that limitations of Pinnacle dose calculation model at an extended source to detector distance (140 cm) might be the cause. Overall, an agreement of 2% was observed between the Monte Carlo and Pinnacle dose maps for this Open Field setup.

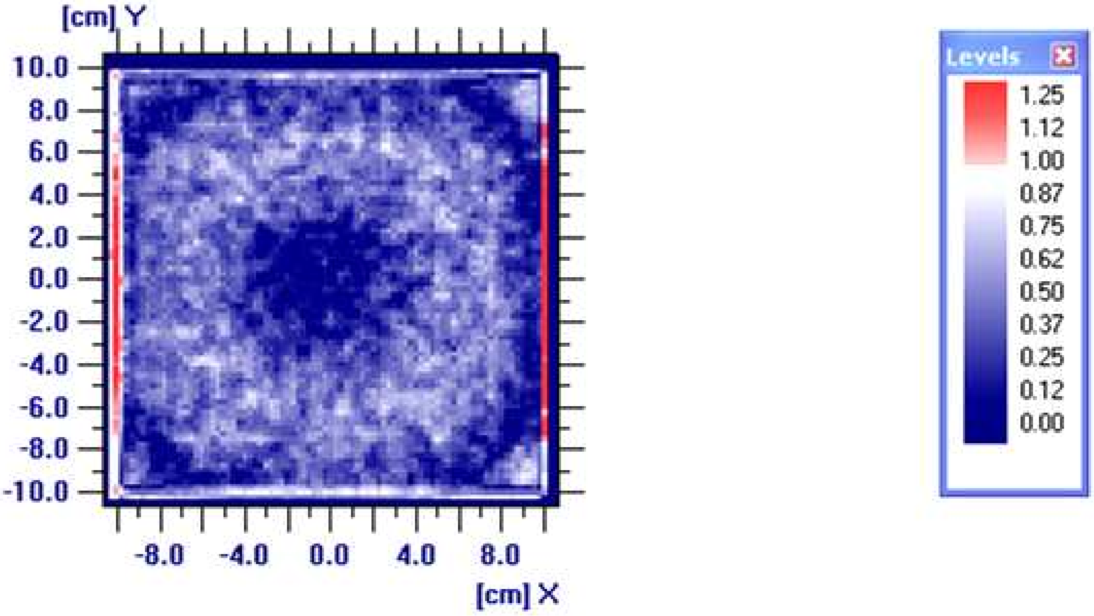

Figure 6.4.6: Gamma map result for the analysis of the Monte Carlo calculated and Pinnacle dose maps acquired from an Open Field setup in figure 6.2.1. The Gamma criteria are 3% and 3 mm for dose difference and DTA respectively.

6.5 Comparison of the Transmitted Dose in a Homogenous Water Phantom

Monte Carlo Versus Measurement – 15 cm homogeneous phantom

The accuracy of the EPID model was further examined by introducing a slab of 15 cm of water between the radiation field and the EPID. The slab of water causes the attenuation of the primary beam and an increase in the average energy of the X-ray beam (beam hardening) passing through the slab. It also produces more scattering radiation (compared to the open field set up) that will reach the EPID sensitive plane. For these reasons, the accuracy of the Monte Carlo profiles was reduced and the data fluctuation increased as shown by the red line in figure 6.5.1 a) and b). The uncertainty in the Monte Carlo calculated data was about 1.2% for this setup. The maximum difference is less than 2.3 %. Figure 6.5.1 shows that both the calculated and the measured profiles are now more flat. The dip and horns features are difficult to distinguish in the profiles. This is the effect of primary beam attenuation and beam hardening and is expected for the dose profile behaviour at larger depths in a water phantom.

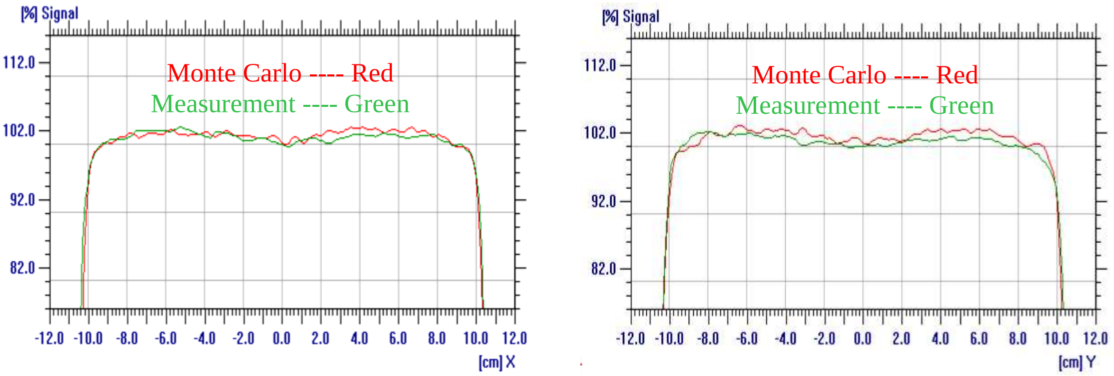

a) Cross-Plane Profile

b) In-plane Profile

6.5.1: Transmitted dose profiles from a 6 MV radiation beam of 15x15 cm^2 field size acquired in the EPID by Monte Carlo calculation and measurement a) in the cross-plane and b) in the in-plane for the 15 cm thick water phantom setup of figure 6.2.1.

In the comparison of the Monte Carlo and measured profiles, the EPID model in the Monte Carlo simulation is simply made of equivalent thickness of water material (unit density) as in the Open Field set up. Observation of figure 6.5.1 shows that the agreement between the Monte Carlo and measured dose profiles in the cross-plane (6.5.1a) and in-plane (6.5.1b) is well below 2%. Observation of the Monte Carlo (6.5.2a) and measured (6.5.2b) dose maps for this setup also indicate good agreement for all data points.

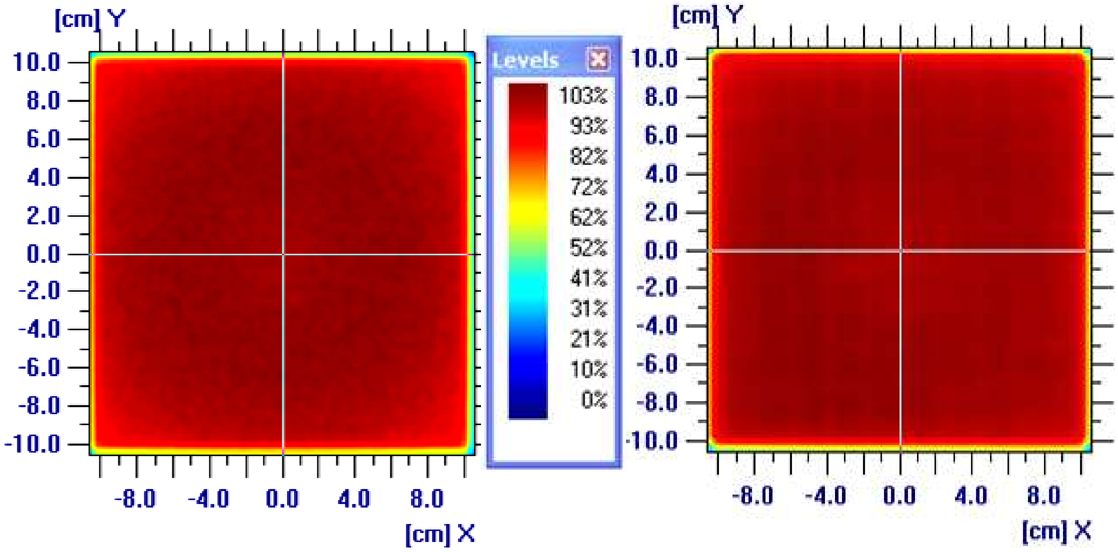

a) Monte Carlo Dose Map

b) Measurement Dose Map

6.5.2: Transmitted dose maps from a 6 MV radiation beam of 15x15 cm^2 field size acquired in the EPID by: a) Monte Carlo calculation and b) measurement for the 15 cm thick water phantom setup of figure 6.2.2. The resolution for both dose maps is 1.27 mm.

Further information about the dose map agreement can be acquired from the gamma map analysis. The result is shown in figure 6.5.3. The total gamma score for this comparison is 99.87%. The majority of the dose points pass the gamma test, indicating that a simple water equivalent EPID model in Monte Carlo code (DOSXYZnrc) is good for predicting the transmitted dose for homogeneous media of unit density. The cloudy white colour on four corners of the gamma map indicates that the gamma test was just passed in these regions. The gamma criteria for this setup were set to 3% and 3 mm for dose difference and DTA respectively. Thus the dose differences between the measured and Monte Carlo calculated data points in these regions are about 3% within the 3 mm DTA. The Monte Carlo dose map in figure 6.5.2 a) shows that the distribution of doses seem to arrive from a rounded radiation field. This causes a faster decrease of doses in the corners of the dose map.

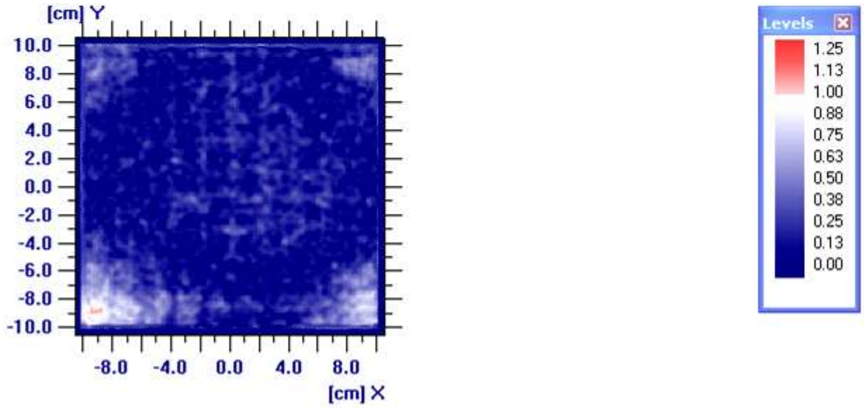

6.5.3: Gamma map result for the analysis of the Monte Carlo calculated and measured dose maps acquired from the 15 cm thick water phantom setup in figure 6.2.2. The Gamma criteria are 3% and 3 mm for dose difference and DTA respectively.

MONTE CARLO VERSUS PINNACLE – 15 CM HOMOGENEOUS PHANTOM

In the comparison between the Monte Carlo and the Pinnacle data, the EPID was modelled using the actual EPID materials in the Monte Carlo code and as well as in Pinnacle TPS. The heterogeneous composition of the actual EPID caused more complex scattering conditions at the EPID's sensitive plane. The additional 15 cm thickness of water further complicated the absorption and scattering of the x-ray beam as discussed in the comparison between the Monte Carlo and measured data for this setup. The combination of these factors increases the uncertainty in the transmitted dose calculation in both the Monte Carlo code and the Pinnacle TPS. The average uncertainty in the Monte Carlo calculation was about 2%. Comparison of the profiles in figure 6.5.1 shows that Monte Carlo and measured data agree well in horn region. This implies that Pinnacle overestimated the transmitted dose near the horn region as shown in figure 6.5.4 below. The dose difference in this region is up to 3.5%.

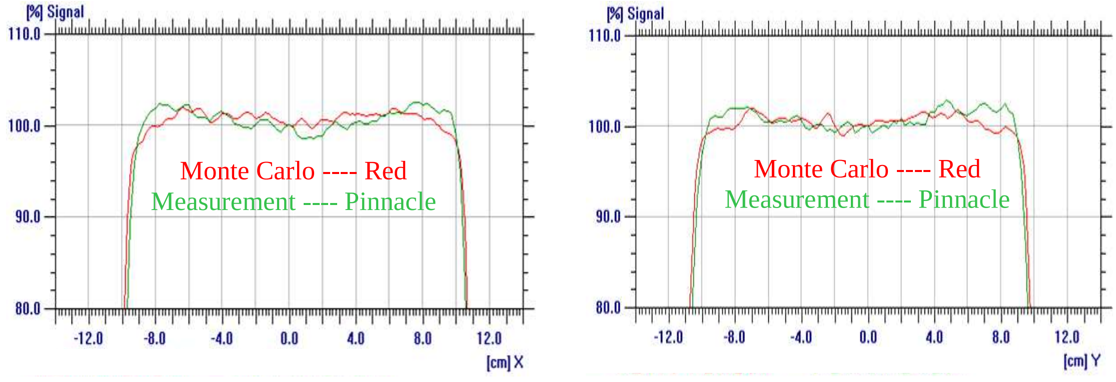

a) Cross-Plane Profile

b) In-plane Profile

6.5.4: Transmitted dose profiles from a 6 MV radiation beam of 15x15 cm^2 field size acquired in the EPID by Monte Carlo calculation and Pinnacle a) in the cross-plane and b) in the in-plane for the 15 cm water phantom setup of figure 6.2.2.

The colour transmitted dose maps in figure 6.5.5 were unable to clearly show the dose difference observed in the above profile comparisons. The gamma map analysis (figure 6.5.6) was very useful, in this case, to further quantify the difference between the Monte Carlo and Pinnacle dose maps. The criteria for the gamma analysis are again 3% and 3 mm for dose difference and DTA respectively. The disagreeing regions, that failed the gamma test, indicate that Pinnacle and Monte Carlo dose differences in all corners are more than 3% within DTA of 3 mm.

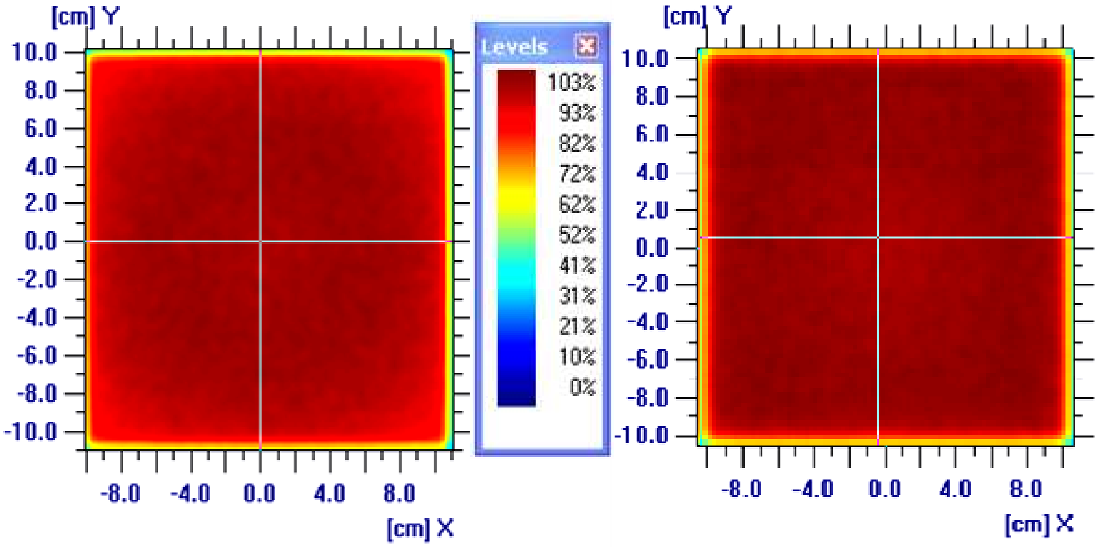

a) Monte Carlo Dose Map b) Pinnacle Dose Map

6.5.5: Transmitted dose maps from a 6 MV radiation beam of 15x15 cm^2 field size acquired in the EPID by: a) Monte Carlo and b) Pinnacle calculation for the 15 cm thick water phantom setup of figure 6.2.3. The resolution for both dose maps is 2.5 mm.

The central region, however, shows that the transmitted dose maps agree within the dose and the distance-to-agreement of 3% and 3 mm respectively. The result of this gamma map is roughly similar to that observed in the Monte Carlo and measured gamma map (refer to figure 6.5.3), however, there are more failed points in this gamma map. The total gamma score for this comparison is 81.97%. As discussed in the comparison between the Monte Carlo and measured dose profiles section, the increase in scattered radiation reaching the EPID's plane as well as the reduction in the EPID signal due to beam absorption in the water phantom are possible causes. Since Pinnacle model of scatter radiation was based on the pre-calculated scatter kernel in homogeneous water phantom (Mackie, Scrimger et al. 1985), some inaccuracies could have occurred in calculating the scatter dose in the EPID's sensitive plane. Monte Carlo method on the other hand, was based on the first principles and thus, dose distribution due to scatter radiation can be calculated more accurately. Furthermore, dose distribution in Pinnacle was modelled for clinical uses at a source to surface distance from 90 to 110 cm, inaccuracies in the Pinnacle transmitted dose calculation at a source to detector distance of 140 cm may occur.

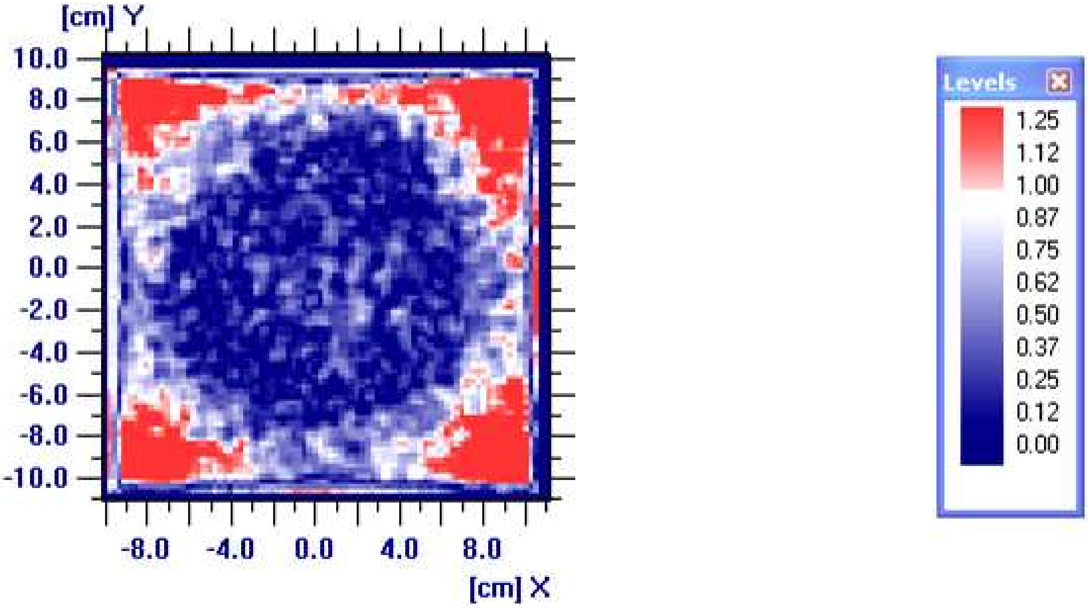

6.5.6: Gamma map result for the analysis of the Monte Carlo and Pinnacle calculated and dose maps acquired from the 15 cm water thick phantom setup in figure 6.2.2. The Gamma criteria are 3% and 3 mm for dose difference and DTA respectively.

6.6 Comparison of the Transmitted Dose in an Anthropomorphic Phantom

MONTE CARLO VERSUS MEASUREMENT – RANDO PHANTOM

The Monte Carlo model of the EPID was further examined by introducing RANDO into the radiation field (refer to setup in figure 6.2.3). For this setup, the EPID was modelled by materials that made up the real EPID. The exposed region of RANDO consisted of a single breast, lung and bone structures that represented the human anatomical structures. These heterogeneity structures caused complicated absorption and scattering of X-rays in the interaction region. The dose profiles in the cross-plane (6.6.1a) and the in-plane (6.6.1b) were compared with the measured data to investigate how well Monte Carlo modelled absorption and scattering of X-rays in heterogeneous phantom. Discrepancies of about 10% were found for both cross-plane and in-plane profiles near the edges of the radiation field. One of the reasons for these discrepancies could be setup uncertainties. In addition, the RANDO phantom used is aged and its body is not as rigid as a new RANDO which made positioning more difficult. The individual slices of RANDO could not be tightly bolted together and thus created air gaps in between slices. The artefact due to the air gaps is shown in the measured (green) and Monte Carlo calculated (red) in-plane profiles of figure 6.6.1b as a decrease in dose (dips). The dose grid for measured data was 1.27x1.27 mm^2 compared to 2.5x2.5 mm^2 for Monte Carlo calculation, and thus displaying the artefact more clear.

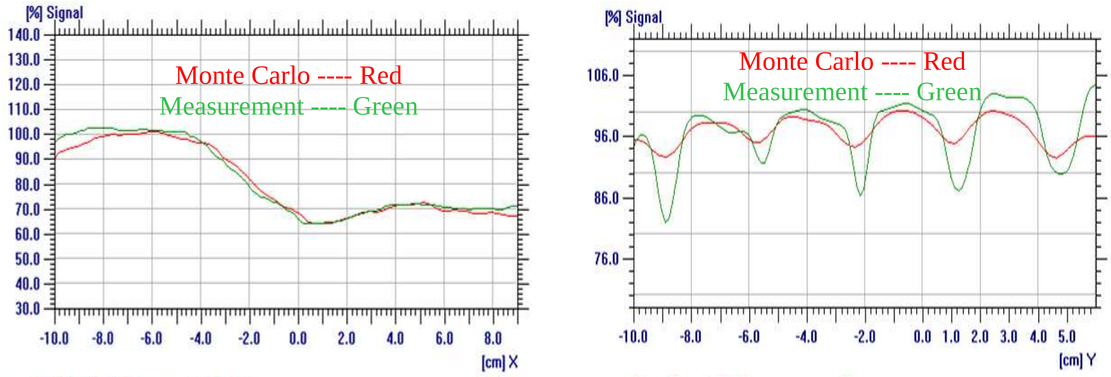

a) Cross-Plane Profile

b) In-plane Profile

Figure 6.6.1: Transmitted dose profiles from a 6 MV radiation beam of 15x15 cm^2 field size acquired in the EPID by Monte Carlo calculation and measurement a) in the cross-plane and b) in the in-plane for the RANDO of figure 6.2.3. The dips present in the in-plane were caused by the air gaps between RANDO slices.

Figure 6.6.2 shows the Monte Carlo and measured transmitted dose maps for this setup. Only relevant region of interests in the Monte Carlo and measured dose map are displayed. Higher dose regions are shown in darker red as labelled by the colour scale used. The artefact due to air gaps in between RANDO slices can also be seen in these dose maps presented as discontinuations in the colour scale along the Y direction (inferior and superior direction of RANDO). The Monte Carlo dose map is more blurred than the measured dose map due to lower resolution dose grid (large voxel size). Increasing the dose grid resolution to be the same as the measured data was impractical due to long calculation time. A total of about 240 hours would be required.

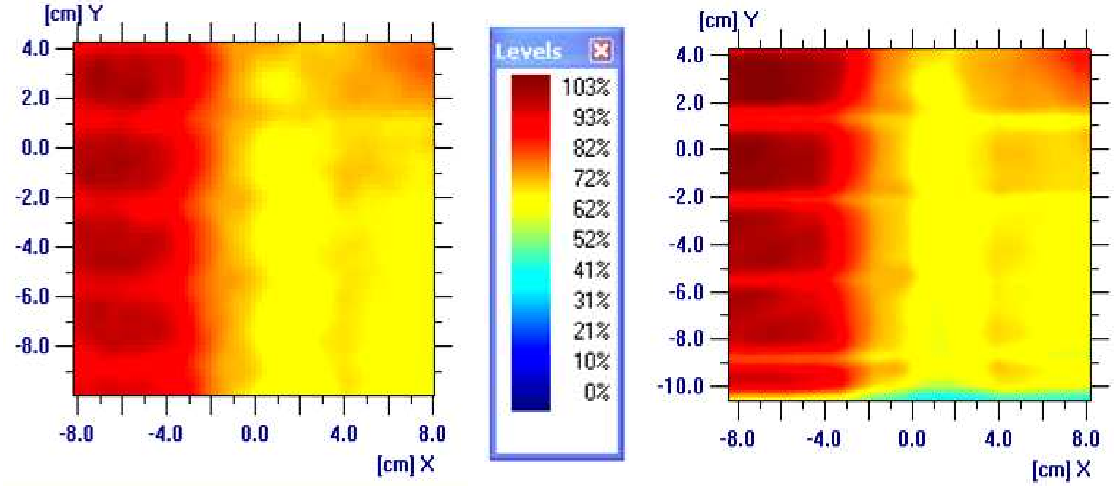

a) Monte Carlo Dose Map b) Measured Dose Map

Figure 6.6.2: The transmitted dose maps in the SLIC EPID acquired by a) Monte Carlo calculation and b) measurement for the RANDO phantom setup in figure 6.2.3. The measured and Monte Carlo calculated dose grids resolution at the EPID plane are 1.27 mm x 1.27 mm and 2.5 mm x 2.5 mm respectively. The artefacts shown in these dose maps were cause by air gaps in between RANDO slices.

The gamma analysis in this case was performed with the gamma criteria of 5% and 5 mm (compared to 3% and 3 mm in the previous setups) in dose difference and DTA respectively. It is clear from the two dose transmitted maps shown in figure 6.6.2 that there are significant differences between the Monte Carlo calculated and measured transmitted doses and that these difference are higher then 3% 3 mm assessment criteria used normally. As a result, in order to assess and quantify the degree of agreement between the two dose maps, the gamma criteria were increased to 5% and 5 mm in dose difference and DTA respectively. Even with this relaxed criteria, there are failed regions in the gamma map (figure 6.6.3) caused by the air gaps between the RANDO slices (shown as pink strips). The gamma criteria of 5% and 5 mm imply that the effect of air gaps causes a dose difference of more than 5% within the DTA of 5 mm between measured and Monte Carlo calculation. A region near the bottom of the gamma map also failed the gamma test. The possible reasons are as follows: the uncertainty in converting the CT number to physical density in the Monte Carlo program, the use of larger voxel size in Monte Carlo calculation to reduce the simulation time and the presence of heterogeneous and curved structures in RANDO which created quite complex absorption and scattering conditions. Overall, the gamma map in figure 6.6.3 shows that there is large number of data points that passed the gamma test, which implies that the dose agreement between the measured and Monte Carlo transmitted dose is within 5% for this setup.

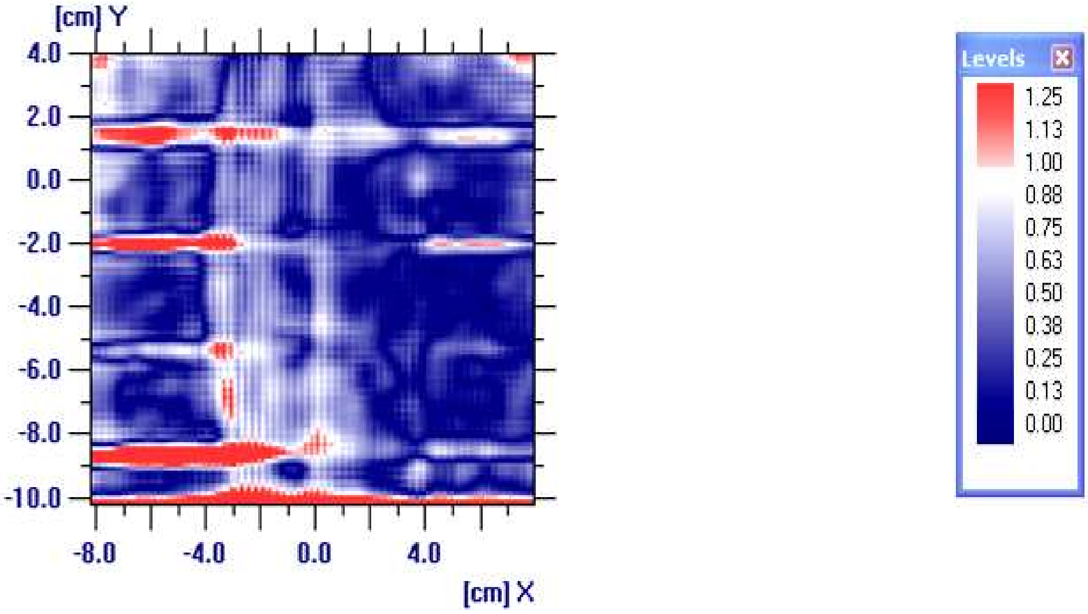

Figure 6.6. 3: Gamma map result for the analysis of the Monte Carlo calculated and measured dose maps acquired from the RANDO setup in figure 6.2.3. The Gamma criteria are 5% and 5 mm for dose difference and DTA respectively.

PINNACLE VERSUS MEASUREMENT – RANDO PHANTOM

The transmitted dose in the real EPID model for RANDO phantom setup was also calculated in Pinnacle. Analysis of the transmitted dose was performed to study the accuracy of Pinnacle TPS calculation of interactions in heterogeneous anatomy. The comparison between the Pinnacle calculated and measured cross-plane profiles (figure 6.6.4a) shows that most data points agree better than 4%. The agreement is worse near the edges of the radiation field, mainly due to setup errors. The dips in dose caused by the presence of air gaps in between RANDO slices were also observed in Pinnacle in-plane profile (figure 6.6.4b). They are shallower than the measured data because of low dose grid resolution (2.5 mm) used in Pinnacle calculation. Figure 6.6.4b also shows an artefact in Pinnacle calculated data. This artefact causes a maximum dose difference of 20% in comparison with the measured in-plane profile.

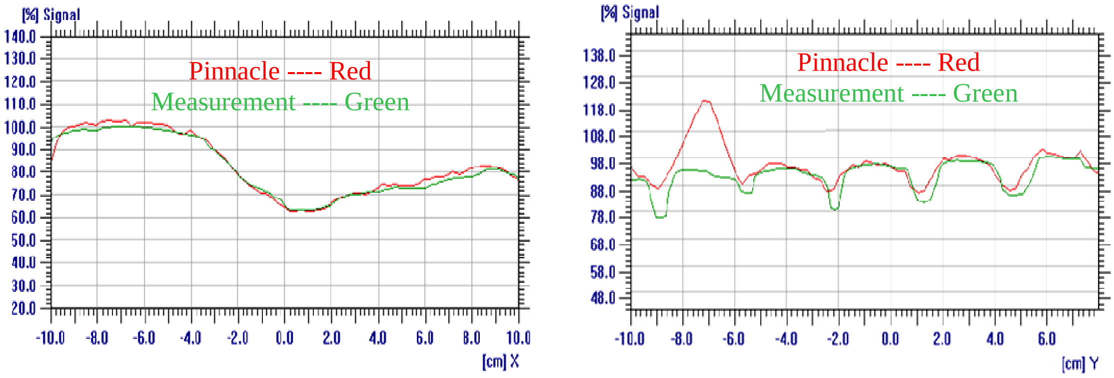

a) Cross-Plane Profile

b) In-plane Profile

Figure 6.6.4: The 15x15 cm^2 transmitted dose profiles in an EPID acquired by Pinnacle calculation and measurement a) in the cross-plane and b) in the in-plane for the RANDO of figure 6.2.3. A big hump in the Pinnacle in-plane profile was the result of an unknown artefact in Pinnacle calculation.

The Pinnacle dose map in figure 6.6.5a indicates that the artefact is actually extends to an area of about 6x2 cm^2 in the lower part of RANDO. The exact cause is unknown however, it looks like an artefact that was commonly caused by low density object within the radiation field.

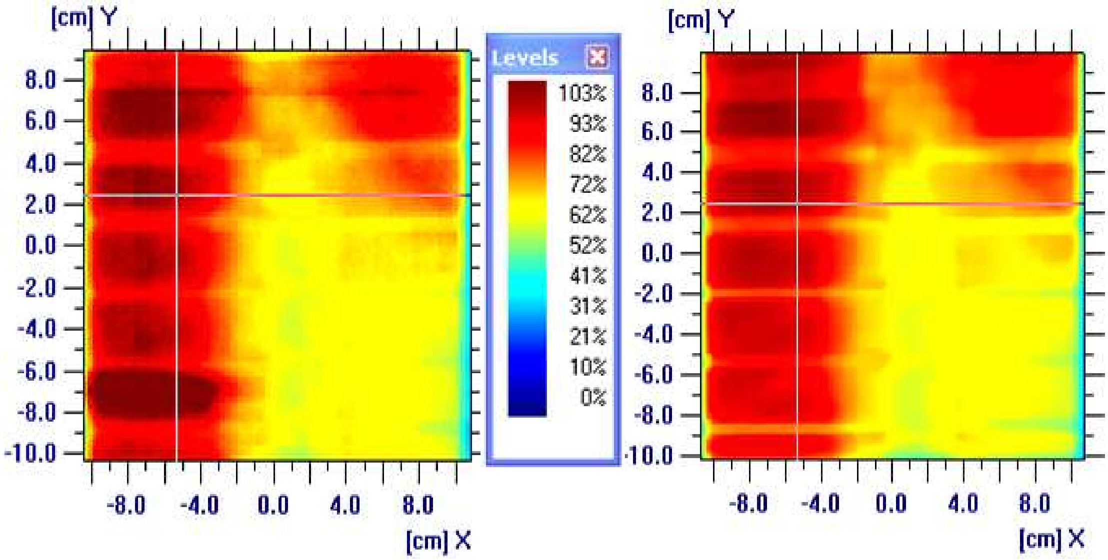

a) Pinnacle Dose Map

b) Measured Dose Map

Figure 6.6. 5: The transmitted dose maps in an EPID acquired by a) Pinnacle calculation and b) measurement for the RANDO setup in figure 6.2.3. The resolution of the measured and Pinnacle calculated dose maps are 1.27 mm and 0.25 mm respectively.

The disagreement in the edges of the radiation field is still present and is indicated by the pink regions on the left and right edges of the gamma map as shown in figure 6.6.6. Observation of the gamma map in figure 6.6.6 shows that the rest of the data points on the Pinnacle dose map agreement well under 5% with the measurement. Compare to figure 6.6.3 it can be seen that Pinnacle transmitted dose map agrees better with measurement than Monte Carlo transmitted dose map. Part of the reason is that Pinnacle system equipped with better graphical tools for planning the calculation. These tools assist in reducing the error in aligning RANDO's landmark in the calculation. These results show that overall, Pinnacle can model X-ray interaction in complex heterogeneous region with an uncertainty of proximately 5%.

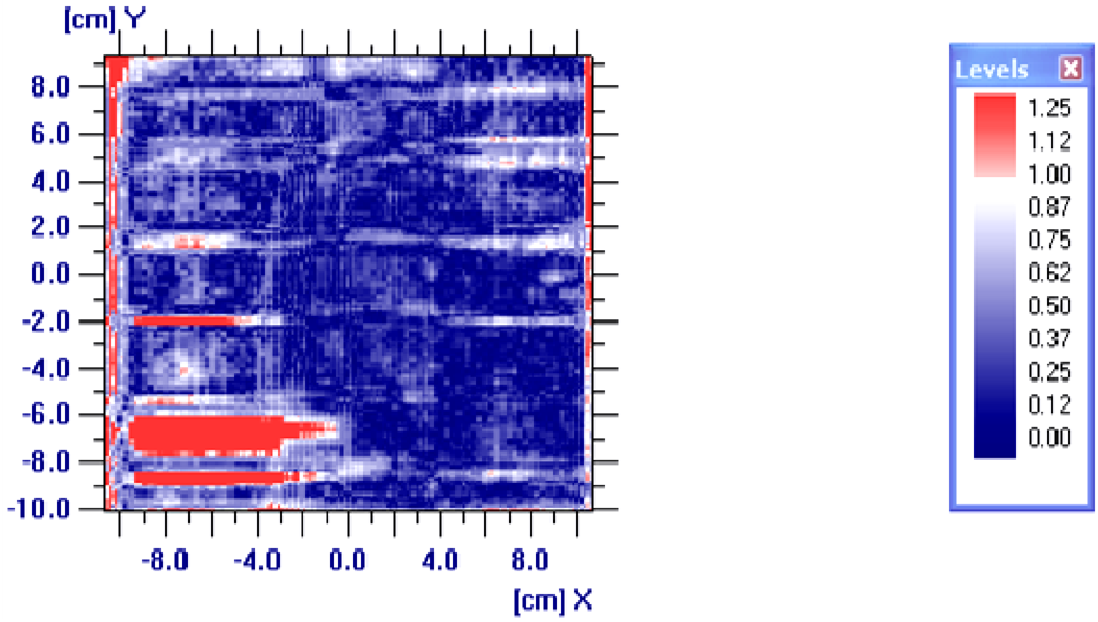

Figure 6.6.6: Gamma map result for the analysis of the Pinnacle calculated and measured dose maps acquired from the RANDO setup in figure 6.2.3. The Gamma criteria are 5% and 5 mm for dose difference and DTA respectively.

6.6 Summary

The verifications of the Monte Carlo and Pinnacle modelled EPIDs were performed in this chapter. Three different phantom setups were designed to study the accuracy of the modelled EPID in calculating the transmitted dose in simple and complicated scattering conditions. Setup number one was an open field where only air was presented in between the radiation source and the EPID. Setup number two was the same as number one except there was 15 cm of water phantom in between the radiation source and the EPID. In setup number three, the 15 cm of water phantom in setup number two was replaced by the RANDO phantom. It was found that the Monte Carlo modelled EPID can provide transmitted dose data that agree well within 3% of the measured and Pinnacle data in a simple scattering condition generated by the open field and 15 cm of water phantom setups. Although higher disagreements were observed in the edges of the radiation field, this can be explained by the existence of high dose gradient. The introduction of RANDO in the radiation field caused complicated scattering conditions due to heterogeneous structure of RANDO phantom. Also, matching the setup in the measurement, Pinnacle and Monte Carlo calculations became more difficult, especially for Monte Carlo calculation due to the lack of graphical setup tools. The combination of these factors made it difficult to calculate the transmitted dose accurately. A general agreement of 5% within the DTA of 5 mm between the Monte Carlo and the measured transmitted dose was observed in a selected region of interest. Similar agreement between Pinnacle calculated and measured transmitted dose was found, however there were more data points that agreed at this level than that compared to Monte Carlo calculated data. However, due to the lack of high resolution dose grid and graphical setup tools, it was uncertain to claim that Monte Carlo method can calculated transmitted dose in heterogeneous phantom more accurate than Pinnacle TPS dose calculation method.

CHAPTER 7

CONCLUSIONS

7.1 Summary

The primary objective of this project was investigation and development of a Monte Carlo method to calculate transmitted dose in a Scanning Liquid Ionisation Chamber EPID and to evaluate the accuracy of the developed Monte Carlo method in comparison with measurement and Pinnacle treatment planning system. Before this objective could be achieved, a Monte Carlo model of a linac head needed to be generated and verified with the measured data so that a good accuracy of the model could be assumed. The corresponding modelling and verification processes were described in chapters 3, 4 and 5.

Chapter 3 presented the principle and the application of the Monte Carlo programs BEAMnrc and DOSXYZnrc to model the Varian 600C/D linac head and to calculate the dose respectively. The modelling and verification process of the linac head were described in details in chapter 4. The results for the verification of the X-ray beam field size and the radial and transverse symmetry properties were also presented in this chapter. It was found that the projected field size at the depth of maximum dose was accurate and good radial and transverse symmetry of the radiation beam was observed. In addition, the modelling of the flattening filter for an X-ray beam were checked by observing the shape of the dip and horns of the beam profile at the depth of maximum dose. An agreement with the measured beam profiles of less 1.5% was found. Furthermore, the statistics for the use of various time reduction (Variance Reduction) parameters were also presented in chapter 4. It was found that Bremsstrahlung Splitting techniques in Monte Carlo program are essential for reducing the calculation uncertainty with minimal increase in calculation time, in other word Bremsstrahlung Splitting techniques improve the efficiency of the calculation. An increase in the efficiency of a factor of 100 was found in this work which was consistent with the reported values (Kawrakow, Rogers et al. 2004).

The major part of this project was the selection of the electron beam energy and the FWHM of the electron beam width that were used in the model of the linac head. It was discussed in the literature that every linac can have slightly different value for electron beam energy and electron beam width and these parameters are difficult to measure (Sheikh-Bagheri and Rogers 2002). Chapter 5 presented a method and results for the selection of the electron beam energy and beam width. These parameters were selected in the current work by comparing the Monte Carlo calculated and measured PDD (using a 10x10 cm^2 field size) and beam profiles (using 40x40 cm^2 field size) at the depth of maximum dose. The PDDs were thoroughly analysed to select the best match for the electron beam energy. The results for the PDD analysis for energies between 5.5 and 6 MeV were shown in chapter 5. The best energy was found to be 5.7 MeV. Attempts were made to select the electron beam energy accurate to ±0.1 MeV, however the results showed that accuracy of ±0.2 MeV is more reasonable because the uncertainty of the calculation is larger than the variation of the PDD for an energy change of 0.1 MeV. The FWHM of the electron beam width was selected by comparing the Monte Carlo simulated and measured X-ray beam profiles for a range of FWHM values of the electron beam widths from 0.9 to 1.5 mm. The best FWHM of the electron beam width was found to be 1.3 mm. The analysis also showed that the beam profiles were influenced by both the electron beam energy and the FWHM of the electron beam width. The beam profiles were more sensitive to the FWHM of the electron beam width than the electron beam energy. This result also confirmed similar finding in the literature (Sheikh-Bagheri and Rogers 2002). An agreement of less than 1% between Monte Carlo and the measured data was found when the selected electron beam energy and beam width of 5.7 MeV and 1.3 mm respectively were used in the linac head model. This satisfies the requirement of 1% and 3 mm dose difference and distance to agreement criteria set for the linac head model in this work.

The modelling of the EPID and the verification of the transmitted dose was described in chapter 6. The geometry of the modelled EPID was obtained from the paper by Spezi and Lewis in 2002 (Spezi and Lewis 2002). The EPID was modelled by 11 layers of various materials and densities by the Monte Carlo code DOSXYZnrc. The transmitted dose in the EPID was also calculated by DOSXYZnrc code. The phasespace file of the modelled linac head was used as a radiation source for the calculation of the transmitted dose. The following phantom setups were designed in this work to assess the accuracy of the Monte Carlo EPID model in different scattering conditions: air, uniform water phantom and humanoid phantom. The first scenario used an open field setup where only air medium was present between the radiation source and the EPID. The 15 cm thick water phantom was inserted between the radiation field and the EPID in the second setup. In the third setup, the water phantom was replaced by the humanoid phantom RANDO. The dose agreements of about 2% within 3 mm distance to agreement were observed between the Monte Carlo, Pinnacle and measured transmitted dose for both, the open field and 15 cm thick water phantom setups. The results led to a conclusion that Monte Carlo model of the EPID can be used with good accuracy for calculating transmitted doses in air and for homogeneous water phantoms. It also confirmed that Pinnacle treatment planning system can be used to model the EPID for transmitted doses calculation for these conditions. In the analysis of the transmitted dose for the RANDO setup, it was found that the dose agreement between the Monte Carlo, Pinnacle and measurement were generally about 5% within the distance to agreement of 5 mm. Pinnacle treatment planning system was found to predict slightly better result than Monte Carlo method. Some difficulty was encountered in aligning RANDO for measurement because the individual RANDO slices could not be tightly joined together. It was found that the artefact in the RANDO transmitted dose map was caused by air gaps in between the RANDO slices. The lack of higher dose resolution in Monte Carlo dose map and good graphical setup tools in the Monte Carlo program also imposed a limitation on the accuracy of the dose calculation. Therefore, for the dose calculation conditions in the current project it remains unclear whether Monte Carlo method can calculate the transmitted dose in heterogeneous phantoms more accurately than Pinnacle treatment planning system. However, a general dose agreement of 5% between Monte Carlo and measurement and Pinnacle and measurement can be concluded from our results.

7.2 Possible Future Development

It was shown in this work that the Monte Carlo method and specifically the Monte Carlo codes BEAMnrc and DOSXYZnrc can be used to model the X-ray linac head with an accuracy of less than 1.5%. The phase space file containing the distribution of the simulated X-rays can be used in the simulation of the transmitted dose in an EPID through air, water phantom or in the human like phantom such as RANDO. In an investigation to assess the Monte Carlo EPID model in the clinically like scenarios, the transmitted dose map in the breast region of RANDO was analysed in this work. The overall agreements of 5% and 5 mm in dose and distance to agreement were found. Further work may be extended to study the transmitted dose in the pelvis region of RANDO. The distribution of material density is more uniform in the pelvis region. Therefore it is expected to see better dose agreement. To assess the Monte Carlo model of the EPID more accurately, comparison of the transmitted dose using the patient data would be of great beneficial. This should be done using the patient setup EPI images to avoid any extra dose to the patient. The difficulties of using heterogeneous phantom such as RANDO in this work were discussed in section 7.1. For dose verification purpose, a simpler heterogeneity phantom such as a uniform rectangular water phantom with air or bone density inserts may be performed prior to the use of RANDO phantom or real patient. This methodology was adopted by Fogliata et al 2007 in their investigation to compare in the dose distribution difference in heterogeneous media for seven different dose calculation algorithms including Pinnacle and Monte Carlo algorithms (Fogliata, Vanetti et al. 2007).

The technical limitation of the Monte Carlo method is the calculation time. It was found in this work that the calculation time of about 200 hours was required to calculate the transmitted dose with an uncertainty of around 1%. This is clinically impractical. Therefore, improvement in the Monte Carlo algorithm to speed up the calculation is mandatory before Monte Carlo can be used in clinical practice.

APPENDIX A

A.1 BEAMnrc's Input File

A typical BEAMnrc input file created in this project. The left column is the parameters used in BEAMnrc. The right column is the description of those parameters interpreted from the BEAMnrc's Users Manual (Rogers, B. et al. 2007).

6mvbeam: Model of 40x40 cm^2, 6MV Varian 600C/D

AIR700ICRU

MEDIUM	Medium of region at front or back of component module (CM) is air.

0, 0, 0, 0, 1, 2, 0,

IWATCH	Normal output. This all we are concerned about, output for every discrete interaction is not needed. Sometime might need option 4 to get graphical output.
ISTORE	Stores random seeds for first history of a batch
IRESTART	First run for this data set. Don't usually repeat simulation with same random number.
IO_OPT	Phase-space output at every scoring plane. Only 1 scoring plane used in this simulation. Data analysis not required
IDAT	Don't store data for re-use, saves time. Only store data if running simulation that takes 100 of hours.
LATCH_OPTION	Creates variables that keep track of which region a particle is in and whether they are secondary particle or created by brems photon.
IZLAST	Do not score z-position of the last site of interaction for photons and electrons created by photons. Use 2 if want to score xyz-postion to be used for EGS_WINDOW. Don't know why scoring is useful.

200000000, 22, 23, 500.0, 2, 5000, 2, 5,

NCASE	The number of particles in the simulation
IXXIN	Random number seed 1. Can be any number and blank is ok.
JXXIN	Random number seed 2. try not to use the same as seed 1.
TIMMAX	Max CPU time allowed for this run in hours
IBRSPL	Perform Directional Bremsstrahlung Splitting (DBS). Most efficient type
NBRSPL	Number of splitting and annihilation per interaction. 5000 for highest efficiency.
IRRLTT	Play Russian Roulette on split photon that are outside the region of interest (fat photon).
ICM_SPLIT	Allow the splitting of photons and electrons (unrelated to Brems Splitting) happen above CM number 5. This option is designed to improve the statistic in the depth-dose calculation by increasing # photons before they incident the phantom. High efficiency can be obtained if the

chosen CM is near the bottom therefore 5 is used.

The next Record is required only if IBRSPL = 2 (DBS is on)

40, 100,

FS	Radius in cm of Brems Splitting region. 40 is chosen to encompass the treatment field size (40x40 cm^2 in this case).
SSD	SSD in cm at which FS is defined.
NMIN	Background splitting. Only use for Selective Brems Splitting (IBRSPL=29).
ICM_DBS	No electron splitting is require since only interested in photon statistic. Otherwise, CM # in which electron splitting is enabled. Only allow to happen in FLATFILT CM which is CM # 2 in this simulation.
ZPLANE_DBS	Layer # within ICM_DBS at which electron splitting occur. Only use if electron splitting is enabled (ICM_DBS > 0) Recommend to set to the back surface of the flattening filter (i.e. total # layers + 1).
IRAD_DBS	1 for distributing NBRSPL split electrons radially symmetric about the beam axis. Beam must be radially symmetric above splitting plane. 0 (default) for random distribution.
ZRR_DBS	Define the Z position of a plane above the splitting plane where Russian Roulette will not apply to non-fat photon about to interact. This option increases the number of electrons below this plane and only use if electron splitting is enabled (ICM_DBS > 0).

The next Record is required only if ICM_SPLIT > 0

5000, 5000,

NSPLIT_PHOT	Photon splitting number. Unrelated to Brems Splitting. Only design to improve efficiency in the phantom depth-dose calculation.
NSPLIT_ELEC	Electron splitting number.

-1, 19, -0.12, 0.0, 0.0, 1.0, 0, 0, 0, 0

IQIN	Charge of the incident particle. 0 for photon, -1 electron.
ISOURCE	Source number. 19 defines a source with Gaussian distribution in the X and Y plane incident from the front.
RBEAM	-FWHM in cm of 2-D Gaussian distribution. Positive value defines Sigma of the 2-D Gaussian distribution.
UINC, VINC, WINC	Define direction cosine relative to the X, Y and Z plane.

For unknown reason the last 4 zeros need to be there

0,

MONOEN	0 for monoenergetic beam and 1 for energy spectrum.

If MONOEN = 0

5.6,

EIN = 5.6	Energy of the monoenergetic beam in MeV.

If MONOEN = 1

Filename of the energy spectrum

`0, 0, 0.7, 0.01, 0, 1, 2.0, 0,`

ESTEPIN = 0	Dummy variable. No need
SMAX = 0	Dummy variable.
ECUT = 0.7	GLOBAL ECUT i.e Cut-off energy in Mev for all region. Electron with energy < this value will be discarded from the simulation and its remaining energy will be deposited to the current region. This value is recommended for peak efficiency.
PCUT = 0.01	GLOBAL PCUT for photon.
IDORAY = 0	Dummy variable
IREJCT_GLOBAL = 1	Do electron range rejection. Electron will be discarded if it cannot pass the current region and has energy less than ESAVE_GLOBAL. 1 for optimal efficiency in this simulation
ESAVE_GLOBAL = 2	Energy in MeV below which electron will be discard in range rejection. Recommended value.
IFLUOR = 0	Dummy variable.

`0, 0, 0, 0, 0,`

IFORCE = 1	0 for Normal photon transport (default). 1 for force photon interaction in the geometry.
NFMIN = 1	# of photon to start forcing. This will always be 1 regardless of what input.
NFMAX = 5	# photon interaction before stop forcing
NFCMIN = 3	CM number at which photon forcing start. CM 3 model the chamber with many thin layers.
NFCMAX = 4	CM number beyond which to stop photon forcing. CM 4 is a thin mirror made of low density material.

`1, 6,`

NSC_PLANES = 1	Number of scoring plane. If > 1 scoring plane required then the subsequence inputs are corresponding to the CM # at which phase-space data are written.
IPLANE_to_CM = 6	CM # correspond to the scoring plane. 6 is the last CM in this simulation.

Repeat the next record for the number of NSC_PLANES

`0, 1,`

NSC_ZONES = 0	For maximum # scoring zone in the chosen scoring plane.
MZONE_TYPE = 1	For square ring zone because radiation field shape is square. 0 for annular zones.

The next record is for NSC_ZONES > 0

RSCORE_ZONE =	Outer radius of each scoring zone in order increasing radius for MZONE_TYPE = 0. It is the half_width from the origin for MZONE_TYPE = 1.

`0,`

ITDOSE_ON = 0	Only total dose is calculated. 1 for total dose and dose components to be calculated. We don’t care about dose component in this simulation.

`0.0,`

Z_min_CM = 0	Z-coordinate of the origin

******* START OF CM SLABS WITH IDENTIFIER TARGET *******

3.809,

RMAX_CM	Lateral dimension from central axis

CM DESCRIPTION: X-RAY TARGET MADE OF TUNGSTEN AND COPPER

3,

N_$SLABS - # layers in this CM

0.0,

ZMIN_$SLABS	Distance from front surface to the origin. defined such that the electron beam enter the fron surface at the origin

0.063, 0, 0, 0, 1, 0,

ZTHICK_$SLABS	Thickness of first layer in cm.
ECUT = 0	Default to ECUTIN.
PCUT = 0	Default to PCUTIN.
DOSE_ZONE = 0	Region to score dose. Not interest in dose in this layer so define 0 for no scoring.
IREGION_TO_BIT=1	Interactions in this layer will be recorded by Latch bit 1
ESAVEIN = 0	Default to ESAVE_GLOBAL

W700ICRU

MED_IN	Medium of first layer

0.265, 0, 0, 0, 1, 0,

ZTHICK_$SLABS	Thickness of second layer in cm.
ECUT = 0	These parameters carry the same meaning as above but apply in second layer.
PCUT = 0	
DOSE_ZONE = 0	
IREGION_TO_BIT=1	
ESAVEIN = 0	

CU700ICRU

MED_IN	Medium of second layer

1.772, 0, 0, 0, 1, 0,

ZTHICK_$SLABS	Thickness of third layer in cm.
ECUT = 0	These parameters carry the same meaning as above but apply in third layer.
PCUT = 0	
DOSE_ZONE = 0	
IREGION_TO_BIT=1	
ESAVEIN = 0	

VACUUM	**MED_IN –** Medium of third layer

****START OF CM FLATFILT WITH IDENTIFIER FLAT_FILTER ****

12.31,	RADIUS OF OUTER BOUNDARY OF CM (RMAX_CM)

CM DESCRIPTION: PRIMARY COLLIMATOR AND FLATTENING FILTER MADE OF TUNGSTEN AND LEAD

2.1,	distance from front of flat_filter to reference plane
13,	# layer in flat_filter
1, 7.849,	# cones in layer 1 and thickness
0.524,	top radius of cones 1 in layer 1
2.481,	bottom radius of cones 1 in layer 1
2, 0.036,	# cones in layer 2 and thickness

```
0, 2.481,               top radius of cone 1 & 2 in layer 2
0.126, 2.490,           bottom radius of cones 1 & 2 in layer 2
2, 0.065,               # cones in layer 3 and thickness
0.126, 2.490,           top radius of cones 1 & 2 in layer 3
0.252, 2.506,           bottom radius of cones 1 & 2 in layer 3
2, 0.164,               # cones in layer 4 and thickness
0.252, 2.506,           top radius of cones 1 & 2 in layer 4
0.504, 2.547,           bottom radius of cones 1 & 2 in layer 4
2, 0.166,               # cones in layer 5 and thickness
0.504, 2.547,           top radius of cones 1 & 2 in layer 5
0.756, 2.588,           bottom radius of cones 1 & 2 in layer 5
2, 0.154,               # cones in layer 6 and thickness
0.756, 2.588,           top radius of cones 1 & 2 in layer 6
1.080, 2.626,           bottom radius of cones 1 & 2 in layer 6
2, 0.151,               # cones in layer 7 and thickness
1.080, 2.626,           top radius of cones 1 & 2 in layer 7
1.260, 2.664,           bottom radius of cones 1 & 2 in layer 7
2, 0.141,               # cones in layer 8 and thickness
1.260, 2.664,           top radius of cones 1 & 2 in layer 8
1.512, 2.699,           bottom radius of cones 1 & 2 in layer 8
2, 0.119,               # cones in layer 9 and thickness
1.512, 2.699,           top radius of cones 1 & 2 in layer 9
1.764, 2.729,           bottom radius of cones 1 & 2 in layer 9
2, 0.103,               # cones in layer 10 and thickness
1.764, 2.729,           top radius of cones 1 & 2 in layer 10
2.016, 2.755,           bottom radius of cones 1 & 2 in layer 10
2, 0.118,               # cones in layer 11 and thickness
2.016, 2.755,           top radius of cones 1 & 2 in layer 11
2.268, 2.784,           bottom radius of cones 1 & 2 in layer 11
2, 0.021,               # cones in layer 12 and thickness
2.268, 2.784,           top radius of cones 1 & 2 in layer 12
2.419, 2.789,           bottom radius of cones 1 & 2 in layer 12
2, 0.113,               # cones in layer 13 and thickness
2.419, 2.789,           top radius of cones 1 & 2 in layer 13
2.816, 2.817,           bottom radius of cones 1 & 2 in layer 13
0.7, 0.01, 2, 3,        ecut, pcut, dose_zone, ire_to_bit on cone 1
in layer 1
AIR700ICRU
0.7, 0.01, 2, 3,        region between the outermost cone and rmax_cm
W700ICRU
0.7, 0.01, 3, 4,        ecut, pcut, dose_zone, ire_to_bit on cone 1
in layer 2
PB700ICRU
0.7, 0.01, 2, 3,        ecut, pcut, dose_zone, ire_to_bit on cone 2
in layer 2
AIR700ICRU
0.7, 0.01, 2, 3,        region between the outermost cone and rmax_cm
W700ICRU
0.7, 0.01, 3, 4,        ecut, pcut, dose_zone, ire_to_bit on cone 1
in layer 3
PB700ICRU
0.7, 0.01, 2, 3,        ecut, pcut, dose_zone, ire_to_bit on cone 2
in layer 3
AIR700ICRU
0.7, 0.01, 2, 3,        region between the outermost cone and rmax_cm
W700ICRU
0.7, 0.01, 3, 4,        ecut, pcut, dose_zone, ire_to_bit on cone 1
in layer 4
PB700ICRU
0.7, 0.01, 2, 3,        ecut, pcut, dose_zone, ire_to_bit on cone 2
in layer 4
AIR700ICRU
0.7, 0.01, 2, 3,        REGION BETWEEN THE OUTERMOST CONE AND RMAX_CM
```

```
W700ICRU
0.7, 0.01, 3, 4,        ECUT, PCUT, DOSE_ZONE, IRE_TO_BIT ON CONE 1
IN LAYER 5
PB700ICRU
0.7, 0.01, 2, 3,        ECUT, PCUT, DOSE_ZONE, IRE_TO_BIT ON CONE 2
IN LAYER 5
AIR700ICRU
0.7, 0.01, 2, 3,        REGION BETWEEN THE OUTERMOST CONE AND RMAX_CM
W700ICRU
0.7, 0.01, 3, 4,        ECUT, PCUT, DOSE_ZONE, IRE_TO_BIT ON CONE 1
IN LAYER 6
PB700ICRU
0.7, 0.01, 2, 3,        ECUT, PCUT, DOSE_ZONE, IRE_TO_BIT ON CONE 2
IN LAYER 6
AIR700ICRU
0.7, 0.01, 2, 3,        REGION BETWEEN THE OUTERMOST CONE AND RMAX_CM
W700ICRU
0.7, 0.01, 3, 4,        ECUT, PCUT, DOSE_ZONE, IRE_TO_BIT ON CONE 1
IN LAYER 7
PB700ICRU
0.7, 0.01, 2, 3,        ECUT, PCUT, DOSE_ZONE, IRE_TO_BIT ON CONE 2
IN LAYER 7
AIR700ICRU
0.7, 0.01, 2, 3,        REGION BETWEEN THE OUTERMOST CONE AND RMAX_CM
W700ICRU
0.7, 0.01, 3, 4,        ECUT, PCUT, DOSE_ZONE, IRE_TO_BIT ON CONE 1
IN LAYER 8
PB700ICRU
0.7, 0.01, 2, 3,        ECUT, PCUT, DOSE_ZONE, IRE_TO_BIT ON CONE 2
IN LAYER 8
AIR700ICRU
0.7, 0.01, 2, 3,        REGION BETWEEN THE OUTERMOST CONE AND RMAX_CM
W700ICRU
0.7, 0.01, 3, 4,        ECUT, PCUT, DOSE_ZONE, IRE_TO_BIT ON CONE 1
IN LAYER 9
PB700ICRU
0.7, 0.01, 2, 3,        ECUT, PCUT, DOSE_ZONE, IRE_TO_BIT ON CONE 2
IN LAYER 9
AIR700ICRU
0.7, 0.01, 2, 3,        REGION BETWEEN THE OUTERMOST CONE AND RMAX_CM
W700ICRU
0.7, 0.01, 3, 4,        ECUT, PCUT, DOSE_ZONE, IRE_TO_BIT ON CONE 1
IN LAYER 10
PB700ICRU
0.7, 0.01, 2, 3,        ECUT, PCUT, DOSE_ZONE, IRE_TO_BIT ON CONE 2
IN LAYER 10
AIR700ICRU
0.7, 0.01, 2, 3,        REGION BETWEEN THE OUTERMOST CONE AND RMAX_CM
W700ICRU
0.7, 0.01, 3, 4,        ECUT, PCUT, DOSE_ZONE, IRE_TO_BIT ON CONE 1
IN LAYER 11
PB700ICRU
0.7, 0.01, 2, 3,        ECUT, PCUT, DOSE_ZONE, IRE_TO_BIT ON CONE 2
IN LAYER 11
AIR700ICRU
0.7, 0.01, 2, 3,        REGION BETWEEN THE OUTERMOST CONE AND RMAX_CM
W700ICRU
0.7, 0.01, 3, 4,        ECUT, PCUT, DOSE_ZONE, IRE_TO_BIT ON CONE 1
IN LAYER 12
PB700ICRU
0.7, 0.01, 2, 3,        ECUT, PCUT, DOSE_ZONE, IRE_TO_BIT ON CONE 2
IN LAYER 12
AIR700ICRU
```

```
0.7, 0.01, 2, 3,        REGION BETWEEN THE OUTERMOST CONE AND RMAX_CM
W700ICRU
0.7, 0.01, 3, 4,        ECUT, PCUT, DOSE_ZONE, IRE_TO_BIT ON CONE 1 IN LAYER 13
PB700ICRU
0.7, 0.01, 2, 3,        ECUT, PCUT, DOSE_ZONE, IRE_TO_BIT ON CONE 2 IN LAYER 13
AIR700ICRU
0.7, 0.01, 2, 3,        REGION BETWEEN THE OUTERMOST CONE AND RMAX_CM
W700ICRU
```

***** START OF CM CHAMBER WITH IDENTIFIER ICHAMBER ******

```
6.0,                    LATERAL DIMENSION
Use CHAMBER CM to model the ion chamber
11.31,                  DISTANCE FROM 1ST CONE TO REF PLANE
0, 17, 0,               # LAYER IN TOP, CHAMBER AND BOTTOM PARTS
5.9, 5.95, 5.98,        INNER, OUTER RAD OF CHAMBER, INNER RAD CONTAINER WALL
0.043, 1,               THICKNESS OF GROUP 1, # LAYER IN GROUP
0.7, 0.01, 4, 5,        ECUT, PCUT, DOSE_ZONE, IREGION_TO_BIT FOR GROUP 1
STEEL700ICRU
0.314, 1,               THICKNESS OF GROUP 2, # LAYER IN GROUP
0.7, 0.01, 4, 5,        ECUT, PCUT, DOSE_ZONE, IREGION_TO_BIT FOR GROUP 2
AIR700ICRU
0.027, 1,               THICKNESS OF GROUP 3, # LAYER IN GROUP
0.7, 0.01, 4, 5,        ECUT, PCUT, DOSE_ZONE, IREGION_TO_BIT FOR GROUP 3
MICA700
0.314, 1,               THICKNESS OF GROUP 4, # LAYER IN GROUP
0.7, 0.01, 4, 5,        ECUT, PCUT, DOSE_ZONE, IREGION_TO_BIT FOR GROUP 4
AIR700ICRU
0.027, 1,               THICKNESS OF GROUP 5, # LAYER IN GROUP
0.7, 0.01, 4, 5,        ECUT, PCUT, DOSE_ZONE, IREGION_TO_BIT FOR GROUP 5
MICA700
0.314, 1,               THICKNESS OF GROUP 6, # LAYER IN GROUP
0.7, 0.01, 4, 5,        ECUT, PCUT, DOSE_ZONE, IREGION_TO_BIT FOR GROUP 6
AIR700ICRU
0.027, 1,               THICKNESS OF GROUP 7, # LAYER IN GROUP
0.7, 0.01, 4, 5,        ECUT, PCUT, DOSE_ZONE, IREGION_TO_BIT FOR GROUP 7
MICA700
0.314, 1,               THICKNESS OF GROUP 8, # LAYER IN GROUP
0.7, 0.01, 4, 5,        ECUT, PCUT, DOSE_ZONE, IREGION_TO_BIT FOR GROUP 8
AIR700ICRU
0.038, 1,               THICKNESS OF GROUP 9, # LAYER IN GROUP
0.7, 0.01, 4, 5,        ECUT, PCUT, DOSE_ZONE, IREGION_TO_BIT FOR GROUP 9
STEEL700ICRU
0.314, 1,               THICKNESS OF GROUP 10, # LAYER IN GROUP
0.7, 0.01, 4, 5,        ECUT, PCUT, DOSE_ZONE, IREGION_TO_BIT FOR GROUP 10
AIR700ICRU
0.027, 1,               THICKNESS OF GROUP 11, # LAYER IN GROUP
```

```
0.7, 0.01, 4, 5,        ECUT, PCUT, DOSE_ZONE, IREGION_TO_BIT FOR
GROUP 11
MICA700
0.314, 1,               THICKNESS OF GROUP 12, # LAYER IN GROUP
0.7, 0.01, 4, 5,        ECUT, PCUT, DOSE_ZONE, IREGION_TO_BIT FOR
GROUP 12
AIR700ICRU
0.027, 1,               THICKNESS OF GROUP 13, # LAYER IN GROUP
0.7, 0.01, 4, 5,        ECUT, PCUT, DOSE_ZONE, IREGION_TO_BIT FOR
GROUP 13
MICA700
0.314, 1,               THICKNESS OF GROUP 14, # LAYER IN GROUP
0.7, 0.01, 4, 5,        ECUT, PCUT, DOSE_ZONE, IREGION_TO_BIT FOR
GROUP 14
AIR700ICRU
0.027, 1,               THICKNESS OF GROUP 15, # LAYER IN GROUP
0.7, 0.01, 4, 5,        ECUT, PCUT, DOSE_ZONE, IREGION_TO_BIT FOR
GROUP 15
MICA700
0.314, 1,               THICKNESS OF GROUP 16, # LAYER IN GROUP
0.7, 0.01, 4, 5,        ECUT, PCUT, DOSE_ZONE, IREGION_TO_BIT FOR
GROUP 16
AIR700ICRU
0.043, 1,               THICKNESS OF GROUP 17, # LAYER IN GROUP
0.7, 0.01, 4, 5,        ECUT, PCUT, DOSE_ZONE, IREGION_TO_BIT FOR
GROUP 17
STEEL700ICRU
0.7, 0.01, 4, 5,        ECUT, PCUT, DOSE_ZONE, IREGION_TO_BIT FOR
CHAMBER WALL
STEEL700ICRU
0.7, 0.01, 4, 5,        ECUT, PCUT, DOSE_ZONE, IREGION_TO_BIT OF GAP
AIR700ICRU
0.7, 0.01, 4, 5,        ECUT, PCUT, DOSE_ZONE, IREGION_TO_BIT
CONTAINER WALL
AIR700ICRU
0,                      RANGE REJECTION WORK ON REGION BY REGION
BASIS
```

******* START OF CM MIRROR WITH IDENTIFIER MIRROR *******

6.38,

RMAX_CM(ICM_$MIRROR) Half-width of CM boundary from the central axis*

CM DESCRIPTION Mirror made of MYLAR at 35 degree about the X-axis.

18.95, 6.17,

ZMIN_$MIRROR Perpendicular distance from front to origin.*

ZTHICK_$MIRROR High of mirror in the Z direction.*

3.79, -5.02,

XFMIN_$MIRROR X-coordinate at which front face of mirror intersect plane at ZMIN_$MIRROR

XBMIN_$MIRROR X-coordinate at which front face of mirror intersect plane at ZMIN_$MIRROR + ZTHICK_$MIRROR. XFMIN AND XBMIN are chosen such that the mirror is 35 degree wrt the central axis

1,

N_$MIRROR # layers in mirror.*

0.005,

DTHICK_$MIRROR Thickness of layer 1.*

0, 0, 0, 4,	
ECUT	These parameters have the same value as in other CM above except particle interactions are tracked using Latch bit 4 and they applied to the **mirror region**.
PCUT	
DOSE_ZONE	
IREGION_TO_BIT	
MYLAR700ICRU	
MED_IN	Medium of layer 1.*

Repeat the previous 2 records for more than 1 layer

0, 0, 0, 4,	
ECUT	These parameters have the same value as in other CM above except particle interactions are tracked using Latch bit 4 and they applied to **region behind the mirror**.
PCUT	
DOSE_ZONE	
IREGION_TO_BIT	
AIR700ICRU	
MED_IN	Medium of region behind mirror is air.
0, 0, 0, 4,	
ECUT	These parameters have the same value as in other CM above except particle interactions are tracked using Latch bit 4 and they applied to **region in front of mirror**.
PCUT	
DOSE_ZONE	
IREGION_TO_BIT	
AIR700ICRU	
MED_IN	Medium of region in front of mirror is air.

******** START OF CM JAWS WITH IDENTIFIER SEC_COL *******

10,	
RMAX_CM(SLABS)	Half width of the JAWS. 10 cm is chosen so that the boundary of the JAWS is big enough to cover the radiation field. It was worked out using similar triangle.
CM DESCRIPTION	Secondary collimator modelled using the CM JAWS
2,	
ISCM_MAX_$JAWS	# paired jaws. There are 2 in this simulation (X and Y)
X,	
XY_CHOICE = X	The top JAW’s separation and movement in the X-axis
28, 35.8, 5.6, 7.16,	-5.6, -7.16,
ZMIN_JAWS(1)	Perpendicular distance (cm) from top surface of X jaws to the origin*.
ZMAX_JAWS(1)	Perpendicular distance (cm) from bottom surface of X jaws to the origin*.
XFP_JAWS(1)	Positive X-coordinate of top corner or perpendicular distance (cm) from top corner of X jaws to central axis. *5.6 cm, 2.8 cm and 1.4 cm give field size of 40x40, 20x20 and 10x10 cm^2 respectively at 100 SSD.*
XBP_JAWS(1)	Positive X-coordinate of bottom corner or perpendicular distance (cm) from bottom corner of X jaws to central axis. *7.16 cm, 3.58 cm, and*

1.79 cm give field size of 40x40, 20x20 and 10x10 cm^2 respectively at 100 SSD.

XFN_JAWS(1) Negative X-coordinate of top corner of X jaws to central axis.

XBN_JAWS(1) Negative X-coordinate of bottom corner of X jaws to central axis.

Y,

XY_CHOICE = Y Bottom JAW’s separation and movement in the Y-axis

36.7, 44.5, 7.34, 8.9, -7.34, -8.9,

ZMIN_JAWS(2) All of these parameters carry the same meaning as X jaws

ZMAX_JAWS(2)

XFP_JAWS(2) *7.34 cm, 3.67 cm and 1.835 cm give field size of 40x40, 20x20 and 10x10 cm^2 respectively at 100 SSD.*

XBP_JAWS(2) *8.9 cm, 4.45 cm and 2.225 cm give field size of 40x40, 20x20 and 10x10 cm^2 respectively at 100 SSD.*

XFN_JAWS(2)

XBN_JAWS(2)

0, 0, 0, 5,

ECUT These parameters have the same meaning as in other CM above but they **apply to interior region (air) of the jaws**. Particle interactions are tracked using Latch bit 5.

PCUT

DOSE_ZONE

IREGION_TO_BIT

0, 0, 0, 5,

ECUT These parameters have the same value as in other CM above except particle interactions are tracked using Latch bit 5.

PCUT

DOSE_ZONE

IREGION_TO_BIT

W700ICRU

MED_IN Medium of X JAWS*

0, 0, 0, 5,

ECUT These parameters have the same value as in other CM above except particle interactions are tracked using Latch bit 5.

PCUT

DOSE_ZONE

IREGION_TO_BIT

W700ICRU

MED_IN Medium of Y JAWS*

******* START OF CM SLABS WITH IDENTIFIER AIR GAP *******

50,

RMAX_CM(SLABS) Lateral dimension from central axis. Exact value is not important, as long as it is large enough to cover the radiation field

CM DESCRIPTION Air filled region. Created so that the phase-space file is at 100 cm from the origin.

1,

N_$SLABS # layers in this CM

44.5,

ZMIN_$SLABS Distance (cm) from front surface to the origin. This CM is directly below the JAWS

```
50.5, 0, 0, 0, 6, 0,
```

ZTHICK_$SLABS=50.5	Slabs thickness in cm. This value is chosen so that the phase-space is 100 cm from the origin.
ECUT = 0	Default to GLOBAL ECUT.
PCUT = 0	Default to GLOBAL PCUT.
DOSE_ZONE = 0	Region to score dose. Not interest in dose in this layer so define 0 for no scoring.
IREGION_TO_BIT=6	Interactions in this layer will be recorded by Latch bit 6
ESAVEIN = 0	Default to ESAVE_GLOBAL

```
*********************end of all CMs*****************************
 #########################
 :Start MC Transport Parameter:

 Global ECUT= 0.7
 Global PCUT= 0.01
 Global SMAX= 1e10
 ESTEPE= 0.25
 XIMAX= 0.5
 Boundary crossing algorithm= PRESTA-I
 Skin depth for BCA= 0
 Electron-step algorithm= PRESTA-II
 Spin effects= On
 Brems angular sampling= Simple
 Brems cross sections= BH
 Bound Compton scattering= On
 Pair angular sampling= Simple
 Photoelectron angular sampling= Off
 Rayleigh scattering= Off
 Atomic relaxations= On

 :Stop MC Transport Parameter:
 #########################
```

Reference:

*Varian specification data for 600C/D 6MV linear accelerator head.

A.2 DOSXYZnrc’s Input File

A typical DOSXYZnrc input file created in this project. The left column are the parameters used in DOSXYZnrc. The right column is the description of those parameters interpreted from the DOSXYZnrc’s Users Manual (Rogers, Walters et al. 2004).

R1) Title: Exposure of a 100x100x40 cm^3 homogeneous water phantom by a 40x40 cm^2 field, 6 MV Varian 600C/D photon beam.

R2) 2	
NMED	Number of media in the simulation.
R3) *H2O700ICRU*	Specific name of the first medium as defined in PEG4 data file.
AIR700ICRU	Name of the second medium and so on for NMED
R4) 0.70, 0.01, 0, 0	
ECUTIN	Electron global cut-off energy in MeV. If ECUTIN> ECUT defined in EGSnrc then ECUTIN is used.
PCUTIN	Similarly to ECUTIN for photon.
ESTEPM	Dummy input. Here for consistency.
SMAX	Dummy input.
R5) -1, -1, -1, 1	
IMAX	# voxels in the X direction. Negative implies equally space uniform voxels in the X direction. Use –ve value here for a simple uniform water phantom.
JMAX	Similar to IMAX for Y direction.
KMAX	Z direction.
IPHANT	Only insert 1 for outputting .egsphant file for displaying non-CT contour using dosxyz_show program otherwise leave blank.

If IMAX, JMAX and KMAX are –ve, the next 6 records are divided equally for X, Y and Z directions.

R6) -50	Coordinate of the boundary of the phantom in the X direction.
1, 100	Size of the voxels in cm and # voxel.
-50	Similar to the parameter above but apply in the Y direction.
1, 100	
0	Coordinate of the boundary in the Z direction.
0.4, 40	Size of the voxels in cm and # voxel.

The combination of these parameters in this record defines the dimension of the phantom. In this case our phantom span from -50 to 50 cm in the X and Y direction and 0 to 16 cm in the Z direction. The phantom is a 100x100x16 cm^3 box.

If IMAX, JMAX and KMAX are +ve, the first parameter in R6 would be the boundary in the X direction and the successive parameters (one each line upto the number defined by I, J, K MAX) will be the size of the voxel.

e.g. -1, -1, 2
0
1, 16
0
1, 16
0
5
10

These parameters define a 16x16x10 cm^3 phantom with 2 layer of 5 cm in the Z direction.

R7) 0, 0, 0, 0, 0, 0, 0, 0

IL	Lower X boundary for assigning the density to a region. Define by voxel number, not by distance.
IU	Upper X boundary.
JL	Lower Y boundary.
JU	Upper Y boundary.
KL	Lower Z boundary.
KJ	Upper Z boundary.
MEDIUM	Medium number. e.g. 1 for water and 2 for air in this simulation. All regions default to medium number 1 if set to 0.
DENSITY	The density of the medium as defined in PEGS4 data file. Set to 0 for default density of the medium specified, faster this way.

Setting all zeros for this record imply that the whole phantom made up of medium 1 and has density of that medium. Otherwise successive line will be tracked and stop when zeros line is found

R8) 0, 0, 0, 0, 0, 0, 0, 0

IL	All of these parameters are the same as in record 7 except this is for setting ECUT and PCUT in region by region basis.
IU	
JL	
JU	
KL	
KJ	
ECUTL	ECUT for local region.
PCUTL	PCUT for local region.

These parameters are not necessary in this simulation therefore no value is assigned.

R9) 51, 51, 51, 51, 1, 40, 1, 0

IL	All of these parameters are the same as in record 7 except these are the region where the dose will be print in the .egslst file.
IU	
JL	
JU	
KL	
KJ	
IZSCAN	Setting the format of the calculated dose output in the .egslst file. > 0 for z-can per page otherwise x-scan per page. Not important. Data analysis should be performed using STATDOSE program.
MAX20	Set to 1 for printing the 20 highest doses.

R9) 2, 2, 0, 0, 0, 180, 0, 0, 180

IQIN	2 for photons, electrons and positrons. -1 for electron and 0 for photon. 2 was chosen to reflect what happen in the treatment.
ISOURCE	Source type. 2 for phase-space file source. Other sources should refer to DOSXYZnrc Users Manual.
X|Y|Z|ISO	X,Y,Z coordinate of the iso-centre for this source type. The origin was chosen to be the iso-centre and the coordinate of the phantom are defined relative to this origin.
THETA	Angle between the Z direction to the line joining the origin of the phase-space plane to the iso-centre. 180^{o} for source to be directed from the top.
PHI	Angle between the X direction to the line joining the origin of the phase-space plane to the iso-centre in the XY plane. 0 was chosen because want source to be perpendicular to X direction.
DSOURCE	Absolute distance from the iso-centre to the origin of the phase-space plane. 0 was chosen so that the phase-space is positioned at the surface of the phantom which is in the plane of Z=0.
PHICOL	Angle by which the collimator is rotated in the collimator plane perpendicular to beam direction. 180^{o} to retain same XY coordinate system for BEAMnrc and DOSXYZnrc.

R10) 2, 0, 2, 0, 0

ENFLAG	0 for monoenergetic beams. 1 for beam with an energy spectrum. 2 for beam with phase-space file. 3 for beam with phase-space + dose components calculation 4 for beam with phase-space file modelled by multiple source model.
MODE	0 for default file format which is suitable for ENFLAG = 2 (7 variable/record). 2 for special file format for phase-space file with Z-last setting (8 variable/record).

MEDSUR	Medium number for region surrounding the phantom. We choose medium number 2 for air surrounding to be consistent with the experiment. 0 for vacuum surrounding.

For ENFLAG > 1

DSURROUND1	If DFLAG = 0, this will be the thickness (cm) of the medium surrounding the phantom in all directions. Chosen 0 to give a default value of 50 cm. If DFLAG = 1, this will be the thickness of the medium surrounding the phantom in the X-direction.
DFLAG	0 to apply DSURROUND to all directions. 1 to apply DSURROUND to the X-direction only.

If DFLAG = 1

DSURROUND2	Thickness of the medium surrounding the phantom in the Y-direction.
DSURROUND3	Thickness of the medium surrounding the phantom in the Z-direction.
DSURROUND4	Thickness of the medium surrounding the phantom in the -Z-direction.

R11) /home/tpham….

FILNAM	Name of the file containing the characteristics of the beam, it is the phase-space file in this simulation. If ENFLAG = 0, this is where we specify the energy of the beam.

R12) 10000, 0, 500, 97, 33, 40, 1, 0, 1, 1, 2, -1, 0, 0, 0

NCASE	# of particles to be simulated initially
IWATCH	0 for no tracking output. 1 for listing every interaction 2 for listing every electron step 4 for creating the files which can be used by EGS_Windows to display the phantom.
TIMMAX	Maximum allowed simulation time.
INSEED 1	Random seed number 1
INSEED 2	Random seed number 2
BEAM_SIZE	Beam size for a square field for dose calculation. Particles will not be tracked if going beyond this field. Only used for source 2, 3 and 4. Used 40 for 40x40 cm^2 field. Default value is 100 which larger than necessary and might waste computing time.
ISMOOTH	1 for redistribute the phase-space whenever a particle is reused (recycle a particle). This is good for simulating random process. 0 for not redistributing.
IRESTART	0 for running the simulation the first time. Other options are not of interest.
IDAT	0 for output intermediate files for restarts.

	1 implies do not do output files at all. This option is used to save time since usually does not need to restart the simulation. 2 for output data file for restart at end only
IREJECT	0 implies no range rejection applied and 1 for apply range rejection. 1 is used to save time.
ESAVE_GLOBAL	Energy below which charged particle will be considered for range rejection. Note that the particle will only be discarded if 2 conditions are met: 1) has energy < ESAVE_GLOBAL and cannot reach the nearest boundary.
NRCYCL	Number of time to recycle each particle in the phase-space. The particle will be recycled NRCYCL+1 times. If < 0, the recycling period will be calculated automatically. The later option is more convenient thus was used here.
IPARALLEL	This option is not necessary in the new version of EGS .
PARNUM	Not required.
N_SPLIT	> 1 for splitting photons N_SPLIT times. More efficient than photon forcing. The rule of thumb for the value of N_SPLIT for good efficiency is N_SPLIT $\geq$ No/(1-$e^{-\lambda}$) where No $\geq$ 5, and λ is the number of photons in the geometry of interest i.e. # photons in the phase-space before entering the phantom.

APPENDIX B

MatLab's Codes

EXTRACTING 2D DOSE MAP FROM MONTE CARLO DOSE OUTPUT FILES FOR OPEN FIELD AND 15CMPHANT SETUP

```
%%% WRITTEN BY THUC PHAM 6/7/2007
display('THIS PROGRAM EXTRACTS THE ENTIRE SIMULATION DOSE MATRIX FROM
3DDOSE FILE AND WRITE TO AN EXCEL FILE')
display('IT PUTS VALUES OF THE X-COORDINATE ALONG THE ROWS e.g.
x2=mc(2,1)')

        %INPUT REQUIREMENT
%# VOXELS IN THE X OR Y DIRECTION

clear all;

FilePath_a = ('*.3ddose');
[dFILENAME_a, dPATHNAME_a] = uigetfile(FilePath_a, 'File Open');
filename1 = [dPATHNAME_a dFILENAME_a];
% filename1=input('Please Enter 3ddose file name: ','s');
fid=fopen(filename1); %NEED TO OPEN BEFORE fscanf CAN READ
x_voxel=input('Please enter the number voxel in the x direction: ');
x_element=1+x_voxel;
y_voxel=input('Please enter the number voxel in the y direction: ');
y_element=1+y_voxel;
z_voxel=input('Please enter the number voxel in the z direction: ');
z_layer=input('Please enter the sensitive plane number to read from:
');
z_layer=z_layer-1;
z_element=1+z_voxel;
element_read= x_voxel*y_voxel*z_layer + 3 + x_element + y_element +
z_element;
read1=fscanf(fid,'%g %g %g',[element_read 1]);
clear read1;
MC=fscanf(fid,'%g %g %g',[x_voxel y_voxel]);
MC=MC*10e+19;

% Normalisation (at the 3x3 centre voxels)
a=x_voxel/2
b=y_voxel/2
norm_factor = mean(mean(MC(a-1:a+1,b-1:b+1)))
MC=100*MC/norm_factor;
filename2=input('Please state the Excel filename to be written:
','s');
xlswrite(filename2,MC)
```

EXTRACTING 2D DOSE MAP FROM MONTE CARLO DOSE OUTPUT FILES FOR RANDO SETUP

```
%%% WRITTEN BY THUC PHAM 6/7/2007
clear all;
display('THIS PROGRAM EXTRACTS THE ENTIRE SIMULATION DOSE MATRIX FROM
3DDOSE FILE AND WRITE TO AN EXCEL FILE')
display('IT PUTS VALUES OF THE X-COORDINATE ALONG THE ROWS e.g.
x2=mc(2,1)')
```

```
        %INPUT REQUIREMENT
%# VOXELS IN THE X OR Y DIRECTION

FilePath_a = ('*.3ddose');
[dFILENAME_a, dPATHNAME_a] = uigetfile(FilePath_a, 'File Open');
filename1 = [dPATHNAME_a dFILENAME_a];
% filename1=input('Please Enter 3ddose file name: ','s');
fid=fopen(filename1); %NEED TO OPEN BEFORE fscanf CAN READ
x_voxel=input('Please enter the number voxel in the x direction: ');
x_element=1+x_voxel;
y_voxel=input('Please enter the number voxel in the y direction: ');
y_element=1+y_voxel;
z_voxel=input('Please enter the number voxel in the z direction: ');
plane_no=input('Please enter the sensitive plane number in the EPID:
');
z_element=1+z_voxel;
header_line = x_element + y_element + z_element + 3;
start_element= x_voxel*(plane_no-1) + header_line;
MC = zeros(z_voxel,x_voxel); % create the zero matrix to be filled
with 3ddose data

for i=1:z_voxel;
    i
read1=fscanf(fid,'%g %g %g',[start_element 1]);
%clear read1;
mc = fscanf(fid,'%g %g %g',[1 x_voxel]);
MC(i,1:x_voxel) = mc;

% start_element1 = x_voxel*(y_voxel-1);
% read2=fscanf(fid,'%g %g %g',[start_element1 1]);
% mc1 = fscanf(fid,'%g %g %g',[1 x_voxel]);
% MC(2,1:x_voxel) = mc1;
start_element = x_voxel*(y_voxel-1);
end

% Normalisation (at the 3x3 centre voxels)
a=z_voxel/2
b=x_voxel/2
norm_factor = mean(mean(MC(a-1:a+1,b-1:b+1)))
MC=100*MC/norm_factor;

filename2=input('Please enter the Excel file name to be written:
','s');
xlswrite(filename2,MC)
```

REFERENCES

Alber, M. (2000). "Hyperion—an integrated IMRT planning tool The Use of Computers in Radiation Therapy." ed W Schlegel and T Bortfeld (Heidelberg: Springer): 46-8.

Andreo, P. (1988). "Stopping-power ratios for dosimetry Monte Carlo Transport of Electrons and Photons." ed T M Jenkins, W R Nelson and A Rindi (New York: Plenum): 485-501.

Andreo, P. and A. Brahme (1986). "Stopping power data for high-energy photon beams." Phys Med Biol **31**: 839-58.

Andreo, P., D. T. Burns, et al. (2004). "Absorbed Dose Determination in External Beam Radiotherapy: An International Code of Practice for Dosimetry based on Standards of Absorbed Dose to Water." IAEA on behalf of EAEA, WHO, PAHO and ESTRO **V.11b**(TRS-398).

Andreo, P. and A. E. Nahum (1985). "Stopping power ratio for a photon spectrum as a weighted sum of the values for
monoenergetic photon beams." Phys Med Biol **30**: 1055-65.

Antonuk, L. E., J. Boudry, et al. (1992). "Demonstration of megavoltage and diagnostic x-ray imaging with hydrogenated amorphous silicon arrays." Med Phys **19**(6): 1455-66.

Baily, N. A., R. A. Horn, et al. (1980). "Fluoroscopic visualization of megavoltage therapeutic x ray beams." Int. J. Radiat. Oncol., Biol., Phys **6**: 935-939.

Bakai, A., M. Alber, et al. (2003). "A revision of the gamma-evaluation concept for the comparison of dose distributions." Phys Med Biol **48**(21): 3543-53.

Boellaard, R., M. van Herk, et al. (1996). "The dose response relationship of a liquid-filled electronic portal imaging device." Med Phys **23**(9): 1601-11.

Boyer, A. L., L. Antonuk, et al. (1992). "A review of electronic portal imaging devices (EPIDs)." Med Phys **19**(1): 1-16.

Broggi, S., C. Fiorino, et al. (2002). "In vivo estimation of midline dose maps by transit dosimetry in head and neck radiotherapy." Br J Radiol **75**(900): 974-81.

Chaney, E. L., T. J. Cullip, et al. (1994). "AMonte Carlo study of accelerator head scatter." Med Phys **21**: 1383-90.

Chin, P. W., E. Spezi, et al. (2003). "Monte Carlo simulation of portal dosimetry on a rectilinear voxel geometry: a variable gantry angle solution." Phys Med Biol **48**(16): N231-8.

Depuydt, T., A. Van Esch, et al. (2002). "A quantitative evaluation of IMRT dose distributions: refinement and clinical assessment of the gamma evaluation." Radiother Oncol **62**(3): 309-19.

Essers, M., B. R. Hoogervorst, et al. (1995). "Dosimetric characteristics of a liquid-filled electronic portal imaging device." Int J Radiat Oncol Biol Phys **33**(5): 1265-72.

Faddegon, B. A., C. K. Ross, et al. (1990). "Forward-directed bremsstrahlung of 10- to 30-MeV electrons
incident a on thick targets of Al and Pb." Med Phys **17**: 773-85.

Faddegon, B. A., C. K. Ross, et al. (1991). "Angular distribution of bremsstrahlung from 15-MeV electrons
incident on thick targets of Be, Al and Pb." Med Phys **18**(727-39).

Fielding, A. L., P. M. Evans, et al. (2002). "The use of electronic portal imaging to verify patient position during intensity-modulated radiotherapy delivered by the dynamic MLC technique." Int J Radiat Oncol Biol Phys **54**(4): 1225-34.

Fielding, A. L., P. M. Evans, et al. (2004). "Verification of patient position and delivery of IMRT by electronic portal imaging." Radiother Oncol **73**(3): 339-47.

Fippel, M., F. Haryanto, et al. (2003). "A virtual photon energy fluence model for Monte Carlo dose calculation." Med Phys **30**(3): 301-11.

Fogliata, A., E. Vanetti, et al. (2007). "On the dosimetric behaviour of photon dose calculation algorithms in the presence of simple geometric heterogeneities: comparison with Monte Carlo calculations." Phys Med Biol **52**(5): 1363-85.

Greer, P. B. and C. C. Popescu (2003). "Dosimetric properties of an amorphous silicon electronic portal imaging device for verification of dynamic intensity modulated radiation therapy." Med Phys **30**(7): 1618-27.

Hansen, V. N., P. M. Evans, et al. (1996). "The application of transit dosimetry to precision radiotherapy." Med Phys **23**(5): 713-21.

Herman, M. G., J. M. Balter, et al. (2001). "Clinical use of electronic portal imaging: report of AAPM Radiation Therapy Committee Task Group 58." Med Phys **28**(5): 712-37.

Huyskens, D., J. Van Dam, et al. (1994). "Midplane dose determination using in vivo dose measurements in combination with portal imaging." Phys Med Biol **39**(7): 1089-101.

Johns, H. E. and J. R. Cunningham (1983). "The Physics of Radiology." (4th edition).

Kawrakow, I., D. W. Rogers, et al. (2004). "Large efficiency improvements in BEAMnrc using directional bremsstrahlung splitting." Med Phys **31**(10): 2883-98.

Kawrakow, I. and D. W. O. Rogers (2006). "Monte Carlo Simulation of Electron and Photon Transport." NRCC Report PIRS-701.

Keall, P. J., J. V. Siebers, et al. (2003). "Determining the incident electron fluence for Monte Carlo-based photon treatment planning using a standard measured data set." Med Phys **30**(4): 574-82.

Khan, F. M. (2003). "The Physics of Radiation Therapy." Lippincott Williams & Wilkins(3 edition).

Kirby, M. C. and P. C. Williams (1993). "Measurement possibilities using an electronic portal imaging device." Radiother Oncol **29**(2): 237-43.

Leong, J. (1986). "Use of digital fluoroscopy as an on-line verification device in radiation therapy." Phys Med Biol **31**(9): 985-92.

Leunens, G., J. Van Dam, et al. (1990). "Quality assurance in radiotherapy by in vivo dosimetry. 1. Entrance dose measurements, a reliable procedure." Radiother Oncol **17**(2): 141-51.

Lovelock, D. M. J., C. Chui, et al. (1995). "A Monte Carlo model of photon beams used in radiation therapy." Med Phys **22**: 1387-94.

Low, D. A., W. B. Harms, et al. (1998). "A technique for the quantitative evaluation of dose distributions." Med Phys **25**(5): 656-61.

Ma, C. M. and D. W. Rogers (2007). "BEAMDP Users Manual." NRCC Report PIRS-0509.

Mackie, T. R. (1990). "Applications of the Monte Carlo Method in Radiotherapy." Dosimetry of Ionization Radiation - Academic Press New York **3**: 541-620.

Mackie, T. R., J. W. Scrimger, et al. (1985). "A convolution method of calculating dose for 15-MV x rays." Med Phys **12**: 188-96.

Mah, E., J. Antolak, et al. (1989). "Experimental evaluation of a 2D and a 3D electron pencil beam algorithm." Med Phys **34**: 1179-1194.

McCall, R. C., R. D. McIntyre, et al. (1978). "Improvement of linear accelerator depth-dose curves." Med Phys **5**: 518-24.

McNutt, T. R., T. R. Mackie, et al. (1996). "Calculation of portal dose using the convolution/superposition method." Med Phys **23**(4): 527-35.

Metcalfe, P. and T. Kron (1997). "Monte Carlo and Convolution Methods."

Metcalfe, P., T. Kron, et al., Eds. (2007). The Physics of Radiotherapy X-rays and Electrons, Medical Physics Publishing.

Mohammadi, M. (2006). "EPID Dosimetry in Intensity Modulated Radiation Therapy Applications." School of Chemistry and Physics University of Adelaide: 21.

Mohammadi, M. and E. Bezak (2006). "Two-dimensional transmitted dose measurements using a scanning liquid ionization chamber EPID." Phys Med Biol **51**(11): 2971-2985. Epub 2006 May 24.

Mohan, R., C. Chui, et al. (1986). "Differential pencil-beam dose computation model for photons." Med Phys **13**: 64-73.

Nahum, A. E. (1978). "Water/air mass stopping power ratios for megavoltage electron and photon beams." Phys Med Biol **23**: 24-38.

Nitschike and Sim (1993). "Testing Random Number Generators For MC Applications." Australas Phys Eng Sci Med **16**: 22-32.

Parsaei, H., E. el-Khatib, et al. (1998). "The use of an electronic portal imaging system to measure portal dose and portal dose profiles." Med Phys **25**(10): 1903-9.

Pasma, K. L., M. Kroonwijk, et al. (1998). "Accurate portal dose measurement with a fluoroscopic electronic portal imaging device (EPID) for open and wedged beams and dynamic multileaf collimation." Phys Med Biol **43**(8): 2047-60.

Pasma, K. L., M. Kroonwijk, et al. (1999). "Transit dosimetry with an electronic portal imaging device (EPID) for 115 prostate cancer patients." Int J Radiat Oncol Biol Phys **45**(5): 1297-303.

Prince, J. L. and J. Links (2006). "Medical Imaging Signals and Systems." Pearson Prentice Hall: New Jersey.

Rizzotti, A., C. Compri, et al. (1985). "Dose evaluation to patients irradiated by 60Co beams, by means of direct measurement on the incident and on the exit surfaces." Radiother Oncol **3**(3): 279-83.

Rogers, D. W., W. B., et al. (2007). "BEAMnrc User's Manual." Report PIRS 0509.

Rogers, D. W., B. A. Faddegon, et al. (1995). "BEAM: a Monte Carlo code to simulate radiotherapy treatment units." Med Phys **22**(5): 503-24.

Rogers, D. W., B. Walters, et al. (2004). "DOSXYZnrc User's Manual." Report PIRS 794.

Rogers, D. W. O. and A. F. Bielajew (1990). "Monte Carlo Technique of Electron and Photon Transport for Radiation Dosimetry." The Dosimetry of Ionizing Radiation - Academic Press **3**: 427-539.

Sheikh-Bagheri, D. and D. W. Rogers (2002). "Monte Carlo calculation of nine megavoltage photon beam spectra using the BEAM code." Med Phys **29**(3): 391-402.

Sheikh-Bagheri, D. and D. W. Rogers (2002). "Sensitivity of megavoltage photon beam Monte Carlo simulations to electron beam and other parameters." Med Phys **29**(3): 379-90.

Sheikh-Bagheri, D., D. W. Rogers, et al. (2000). "Comparison of measured and Monte Carlo calculated dose distributions from the NRC linac." Med Phys **27**(10): 2256-66.

Shortt, K. R., C. K. Ross, et al. (1986). "Electron Beam Dose Distributions Near Standard Inhomogeneities." Phys Med Biol **31**: 235-249.

Spezi, E. and D. G. Lewis (2002). "Full forward Monte Carlo calculation of portal dose from MLC collimated treatment beams." Phys Med Biol **47**(3): 377-90.

Taborsky, S. C. (1981). "Digital imaging for radiation therapy verification." Proc. SPIE **314**: 164-171.

Treurniet, J. R. and D. W. Rogers (1999). "EGS_Windows_4.0 User's Manual " NRCC Report PIRS-0669.

Tzedakis, A., J. E. Damilakis, et al. (2004). "Influence of initial electron beam parameters on Monte Carlo calculated absorbed dose distributions for radiotherapy photon beams." Med Phys **31**(4): 907-13.

van Dyk, J. (1999). "The Modern Technology of Radiation Oncology - A Compendium for Medical Physicists and Radiation Oncologists." Medical Physics Publishing.

Van Esch, A., B. Vanstraelen, et al. (2001). "Pre-treatment dosimetric verification by means of a liquid-filled electronic portal imaging device during dynamic delivery of intensity modulated treatment fields." Radiother Oncol **60**(2): 181-90.

van Herk, M. (1991). "Physical aspects of a liquid-filled ionization chamber with pulsed polarizing voltage." Med Phys **18**(4): 692-702.

van Herk, M. and H. Meertens (1988). "A matrix ionisation chamber imaging device for on-line patient setup verification during radiotherapy." Radiother Oncol **11**(4): 369-78.

van Zijtveld, M., M. L. Dirkx, et al. (2006). "Dosimetric pre-treatment verification of IMRT using an EPID; clinical experience." Radiother Oncol **81**(2): 168-75.

Walters, B., I. Kawrakow, et al. (2007). "DOSXYZnrc Users Manual." NRCC Report PIRS-974revB.

Walters, B., I. Kawrakow, et al. (2007). DOSXYZnrc Users Manual. NRCC Report. Ottawa, NRCC.

Walters, B. R., I. Kawrakow, et al. (2002). "History by history statistical estimators in the BEAM code system." Med Phys **29**(12): 2745-52.

Weisstein, E. (2008). "Normal Distribution." Wolfram MathWorld: http://mathworld.wolfram.com/NormalDistribution.html.

Wendling, M., R. J. Louwe, et al. (2006). "Accurate two-dimensional IMRT verification using a back-projection EPID dosimetry method." Med Phys **33**(2): 259-73.

Zhao, W., I. Blevis, et al. (1997). "Digital radiology using active matrix readout of amorphous selenium: construction and evaluation of a prototype real-time detector." Med Phys **24**(12): 1834-43.